Title
Design and Investigation of Membrane-Electrode Assemblies for the Electrochemical Reduction of CO2

Author
Romiluyi, Oyinkansola Susan

Publication Date
2022

Peer reviewed|Thesis/dissertation

Design and Investigation of Membrane-Electrode Assemblies for the Electrochemical Reduction of CO_2

By

Oyinkansola Susan Romiluyi

A dissertation submitted in partial satisfaction of the

requirements for the degree of

Doctor of Philosophy

in

Chemical Engineering

in the

Graduate Division

of the

University of California, Berkeley

Committee in charge:

Professor Alexis T. Bell, Co-Chair
Dr. Adam Z. Weber, Co-Chair
Professor Bryan McCloskey
Professor Andrew Minor

Summer 2022

Design and Investigation of Membrane-Electrode Assemblies for the Electrochemical Reduction of CO_2

Oyinkansola Susan Romiluyi

Abstract

Design and Investigation of Membrane-Electrode Assemblies for the Electrochemical Reduction of CO_2

by

Oyinkansola Susan Romiluyi

Doctor of Philosophy in Chemical Engineering

University of California, Berkeley

Professor Alexis T. Bell, Co-Chair
Dr. Adam Z. Weber, Co-Chair

The electrochemical conversion of carbon dioxide is of increasing interest because it offers a means of achieving the generation of value-added products, mitigation of greenhouse gas (GHG)-emissions, and storage of intermittent renewable energy. Aqueous gas-diffusion electrode (GDE) systems for electrochemical CO_2 reduction allow for an order-of-magnitude increase in obtainable limiting current densities compared to planar systems due to their inherent increase in CO_2 flux. Despite this improvement, aqueous GDEs exhibit significant ohmic resistances that limit the current densities that can be achieved at applied overpotentials, making them impractical for industrial implementation.

Membrane-electrode assemblies (MEAs), consisting of humidified gaseous feeds at one or both porous electrodes and no aqueous electrolyte (only a solid ion-conducting polymer or ionomer), can overcome the limitations of aqueous GDEs. Commercial-scale generation of carbon-containing products by means of electrochemical CO_2 reduction (CO_2R) requires electrolyzers operating at high current densities and product selectivities. MEAs have been shown to be suitable for this purpose. In this dissertation, various MEA designs are considered: the Full-MEA, the H_2O-MEA, and the Exchange-MEA. Based on recent modeling and experimental findings presented and cited within this dissertation, the Exchange-MEA emerges as the cell design of choice for ultimately developing an efficient and scalable CO_2 reduction device because it enables good ionomer and membrane hydration, as well as high catalyst activity and selectivity. However, despite its outwardly simple design, the MEA is a complicated system that warrants further investigation into its structure and function.

There is significant complexity in the CO_2R MEA, specifically in its ionomer-based catalyst layers. In particular, the cathode catalyst layer and the multiple phenomena occurring in this region contribute extensively to the rate of CO_2R, overall current-voltage performance, and product selectivity profiles in the MEA. Thus, the theme of this dissertation is to elucidate how key components in the cathode catalyst-layer region (ionomer, catalyst, water, *etc.*) interact so that a systematic understanding of how these microscale interactions contribute to underlying, limiting phenomena can be achieved and ultimately used to improve macroscale CO_2R MEA performance.

Chapter 1 of this dissertation introduces the field of CO_2R and discusses current progress towards understanding the complexity of the catalyst layer. Chapter 2 documents the experimental and engineering design work done on MEAs within this dissertation project, presenting a systematic exploration of various system factors, such as relative humidity and temperature, as well as the development of MEA fabrication and operation best practices and guiding principles. In Chapter 3, the influence of the ionomer-to-catalyst ratio (I:Cat), the catalyst loading, and the catalyst-layer thickness – as well as the anode exchange solution concentration, the MEA cell design, and the degree of hydration – on the performance of a cathode catalyst layer containing Ag nanoparticles supported on carbon is investigated, with the goal of establishing how and why these parameters affect the total current density and the partial current densities of H_2 and CO. Chapter 4 delves deeper into more fundamental aspects of the Ag/ionomer interface, its chemistry/pH, and its effect on kinetic behavior, interfacial capacitance, catalyst-layer morphology, CO_2 crossover, CO_2R selectivity, and activity. Lastly, Chapter 5 takes a forward-looking approach and outlines key open questions and emerging challenges in CO_2 electrochemical synthesis towards improved optimization and understanding for scale-up and technological deployment.

To my patient advisors and committee members – Adam, Alex, Nem, Bryan, Andy

To my dear family – Femi, Abisola, Seun – and loved ones

To my indispensable dissertation writing partners – Ibeh, Pelagie, Soliver, Julie

To my treasured mentors – Dr. Peter Agbo, Professor Enrique Iglesia – and collaborators

To my irreplaceable Weber and Bell group members – and CBE, JCAP, and LBNL colleagues

To my cherished BGESS comrades – and Cal friends

– and to all the invaluable people I've met along this journey

……

Without even just one of you, this would not be possible.

Thank you from the bottom of my heart.

Contents

List of Figures

List of Tables

Acknowledgements

I gratefully acknowledge Lawrence Berkeley National Laboratory's Laboratory Directed Research and Development (LDRD) Grant for funding. This material is based in part upon work performed at the Joint Center for Artificial Photosynthesis, a DOE Energy Innovation Hub, supported through the Office of Science of the U.S. Department of Energy under Award Number DE-SC0004993.

1 Introduction

1.1 The Case for Electrochemical CO_2 Reduction

One of, if not the most pressing and existential crisis of our time is the issue of climate change. As each year passes, the threat of an increase in the global average temperature to well above 2ºC (above pre-industrial levels) appears to grow.[1,2] Before the term "climate change" was used to describe the extensive, largely irreversible, and increasingly devastating global weather, climate, and ecosystem effects witnessed today, the term "global warming" was used to link a rise in global temperature to a rise in greenhouse gas (GHG)-emissions (like carbon dioxide, methane, and nitrous oxide) in the earth's atmosphere. These terms were first coined and introduced by Wallace Broecker in his seminal 1975 paper[3] and, in their seminal climate paper in 1999,[4] Michael Mann, Raymond Bradley, and Malcolm Hughes presented the iconic hockey-stick graph depicting the sharp rise in the global mean temperature record over the past millennium. Now, both "climate change" and "global warming" are used interchangeably to refer to the unprecedented, long-term heating of our climate systems by heat-trapping atmospheric gases primarily stemming from anthropogenic activities (especially fossil fuel extraction, production, transformation, and combustion) since the beginning of the late-industrial revolution period in the mid-1800s. The notable imbalance caused by the accumulation of these GHG-emissions is not only responsible for a global temperature rise, but also various, related adverse environmental phenomena such as frequent extreme weather occurrences,[5] prolonged and severe droughts,[6] record-breaking heat waves,[7,8] near-permanent loss of biodiversity,[9–12] ocean acidification,[13] glacier melt,[14] sea-level rise,[15,16] as well as related adverse impacts on human civilization like poor farming yields and negative health effects.[17]

Humanity's collective journey in understanding both the underlying science and sheer gravity of this situation has taken decades and it is now self-evident that the current trends must be mitigated and reversed. Addressing this GHG-emission problem by nipping it at the source (via immediate carbon capture and storage) is one of the more popular solutions currently under consideration.[18,19] Yet, for such an issue of tremendous import, there are in fact numerous ways and strategies to approach a solution, many of which are multi-pronged and multi-disciplinary in nature. Approaches range from long-term, culture-shifting solutions – such as improved generation of and access to renewable energy options (*i.e.,* hydropower, wind, solar, nuclear), increased reforestation and afforestation efforts, reduced meat farming and consumption, increased manufacturing and use of biodegradable and bio-sourced products, and reduced food and energy waste[20] – to more drastic, last-ditch efforts in the realms of geoengineering like artificial cooling, ocean alkalinity enhancement, and ocean fertilization.[21,22] Almost none of these individual solutions constitute a silver bullet or panacea in that they each lack the technological capacity and versatility to be broadly applied across various countries, cultures, and natural resource regions. Although there are several ongoing debates about how to reduce, capture, or bury our emissions, there have been few discussions on how to reframe our thinking around them, particularly the CO_2 molecule itself. A molecule in such abundance in our atmosphere should be able to serve a more useful purpose than to be buried out of sight, never minding the adverse environmental impacts associated with this capture-and-sink strategy.[23] In other words, there should be a way of treating this gas as something other than a waste product and rather as something that has untapped, potential value. The key question is whether CO_2 can be transformed into the building blocks used to produce the chemicals, fuels, and materials we rely on for our current and future technology needs and

livelihoods. Since it is highly unlikely that mankind will completely halt or even temper all forms of economic activity and technological progression in the coming decades, a better strategy would be to transform the very source of this existential crisis into a carbon source that can be used to "fuel" our advancement.

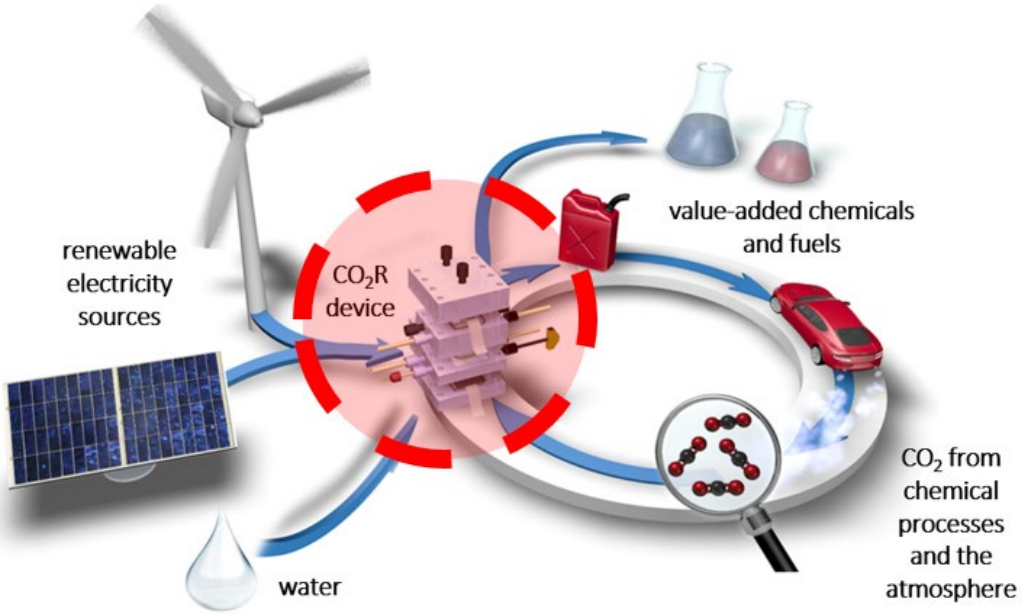

Figure 1.1. Schematic of the carbon-neutral concept of electrochemical CO_2 reduction. The choice and design of the CO_2 reduction device is crucial. *Design schematic modified from Ref.* [24].

The hydrogenation of carbon-containing compounds into a range of hydrocarbons and alcohols is not a new concept and has been practiced in traditional thermal catalysis for decades.[25–27] What is relatively novel is that this reduction process can be done electrochemically, at much less severe pressure and thermal conditions, and, better yet, renewably: this is the case for the electrochemical reduction of CO_2. As shown in **Figure 1.1**, electrochemical CO_2 reduction (CO_2R) offers a versatile option for converting CO_2 to chemical feedstocks, fuels, and materials using electricity from renewable sources such as solar and wind energy. Thus, with electrochemical CO_2 reduction, it is possible to create carbon-neutral products of high market value and/or large market size such as carbon monoxide (syngas), formic acid, methane, ethylene, ethanol, and 1-propanol.[28] The foundational work of Yoshio Hori serves as a proof-of-concept for this process by showing that the choice of electrocatalyst metal strongly determines product selectivity.[29–33] Metals such as tin (Sn) show appreciable selectivity for formic acid, silver (Ag) and gold (Au) are selective for carbon monoxide, and copper (Cu) is selective for various multicarbon hydrocarbons and oxygenated compounds.[34] Moreover, if the CO_2 can be sourced not only from near-pure point sources, such as from industrial fermentation,[35] aluminum smelting, or cement manufacturing,[36] but also extracted directly from the atmosphere via direct air capture (DAC), it would herald the revolutionary, game-changing production of carbon-*negative* products. This is the reason why research into industrial-scale electrochemical CO_2 reduction is ongoing and is of great importance. Performing CO_2R electrochemically and on an industrial scale would simultaneously allow for GHG-emission mitigation, intermittent renewable energy storage,[34] scalable modular implementation with reduced land-use requirements,[37] and onsite CO_2 conversion into energy-dense products that are compatible with our existing energy and transportation infrastructure.[34,38]

1.2 Membrane-Electrode Assemblies as Efficient CO_2 Reduction Test-Beds

Key to achieving industrial-scale electrochemical CO_2 reduction is the development of a CO_2 reduction device that allows for the efficient and selective production of C_{2+} products, such as ethylene and ethanol, which are of special interest due to their ease of conversion to liquid fuels and their commercial value.[34] Thus, electrocatalysts that can selectively produce a range of hydrocarbons and alcohols, such as Cu, are required.[33] However, for most of the work in this dissertation, Ag is the electrocatalyst of choice as it is a well-behaved catalyst known to produce carbon monoxide (CO) exclusively via the multi-electron CO evolution reaction (COER), in addition to hydrogen (H_2) from the parasitic, multi-electron hydrogen evolution reaction (HER)[33] (see **Equations 1.1 thru 1.2**):

$$\text{COER: } CO_2 + H_2O + 2e^- \rightarrow CO + 2OH^- \ (U^\circ = -0.11 \text{ V vs. SHE}) \quad (1.1)$$

$$\text{HER: } 2H_2O + 2e^- \rightarrow H_2 + 2OH^- \ (U^\circ = -0.828 \text{ V vs. SHE}) \quad (1.2)$$

Using Ag allows for the product distribution to be greatly simplified so that the effect of design changes can be more clearly observed. Moreover, its product mixture of H_2 and CO (syngas) can be industrially upcycled to higher-order hydrocarbons via Fischer-Tropsch synthesis.[25,38] The electrocatalyst used for the anode for most of this work is iridium/iridium oxide (Ir/IrO_2) because it is highly active for the oxygen evolution reaction (OER)[39] (see **Equation 1.3**):

$$\text{OER: } 4OH^- \rightarrow O_2 + 2H_2O + 4e^- \ (U^\circ = 0.401 \text{ V vs. SHE}) \quad (1.3)$$

This electrochemical system consisting of **Equations 1.1 thru 1.3** is operated under alkaline conditions because experimental and theoretical studies confirm that lower CO_2R activation energies, and hence enhanced CO_2R selectivity, can be achieved in higher pH environments.[34,40–44] The sum of the above electrochemical half-reactions (discounting the parasitic HER) brings about an overall reaction that is essentially the reverse of complete combustion (see **Equation 1.4**):

$$CO_{2(g)} \rightarrow CO_{(g)} + \frac{1}{2}O_{2(g)} \quad (1.4)$$

In a typical CO_2 reduction electrolytic cell, an overpotential must be supplied above the cell's thermodynamic potential in order to drive the CO_2R/COER, HER, and OER electrode reactions.[45] The performance of a CO_2R device, which in this work refers to the measured total current density and the CO faradaic efficiency (*i.e.,* CO_2R selectivity), depends on numerous interdependent factors, making for a complex system in which the choice of cell design plays a significant role. Over the course of this dissertation project, different electrochemical cell designs were considered and investigated: a planar cell, an aqueous gas-diffusion electrode (GDE) cell, and an MEA (membrane-electrode assembly) cell. **Figure 1.2** summarizes the specific advantages and disadvantages of each design.

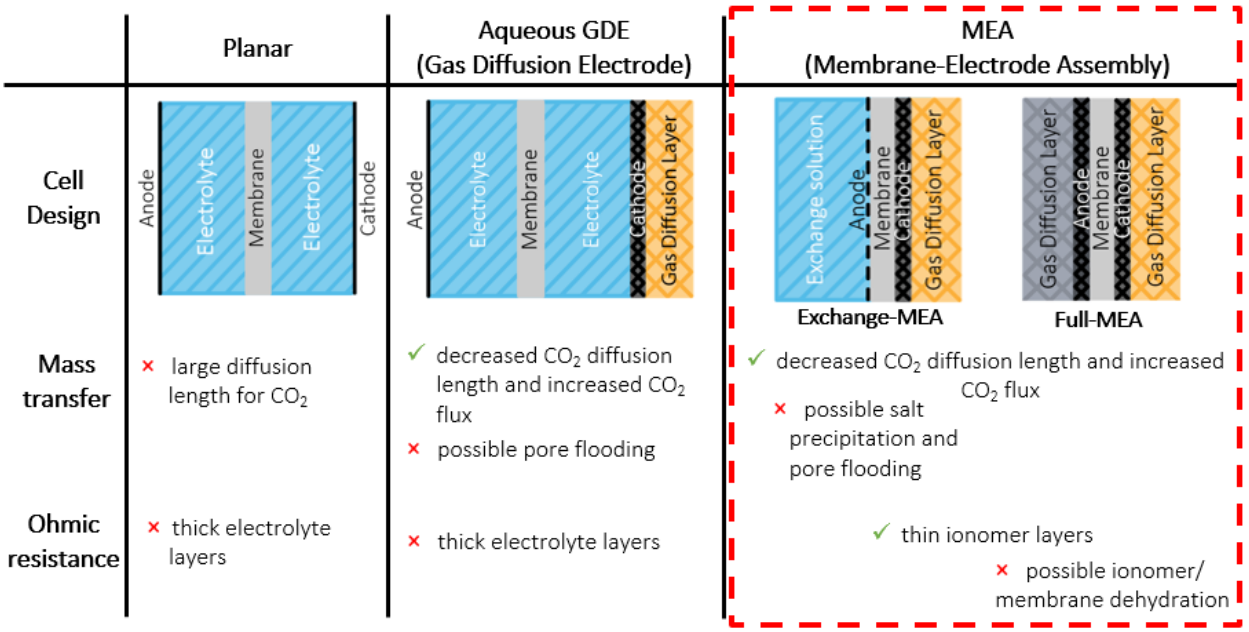

Figure 1.2. Comparison of various electrochemical CO_2 reduction device systems. *Design schematics modified from Ref.* [46].

CO_2 reduction in the planar cell experiences mass-transfer limitations due to a large, ~100 µm-thick hydrodynamic boundary layer near the flat cathode surface.[45,47,48] This large diffusion barrier for CO_2, coupled with the poor solubility of CO_2 in aqueous solutions under ambient conditions (*i.e.,* 33 mM atm^{-1}),[49] limits the achievable current density to ~10 mA cm^{-2} for planar systems. Aqueous GDEs are able to circumvent this mass-transport limitation and obtain more than an order-of-magnitude increase in current densities and achieve higher CO faradaic efficiencies.[33,50–56] However, aqueous GDEs have significant ohmic limitations resulting from the large distance between the anode and cathode, which limits their achievable current densities, rendering them impractical for industrial implementation.[57] A membrane-electrode assembly (MEA) addresses these issues by eliminating the liquid electrolyte and replacing it with a solid polymer electrolyte. The reduction in the anode-to-cathode distance leads to a one to two order-of-magnitude decrease in the ohmic drop of the system, and thus higher current densities can be applied at the same overpotentials.[46] There are two main MEA designs, each shown in **Figure 1.2**: the Exchange-MEA, which has humidified feed entering the cathode and a flowing exchange solution behind the anode, and the Full-MEA, which has humidified feed entering both the cathode and anode. The Full-MEA can achieve high current densities but has a tendency to suffer from low membrane and ionomer hydration.[46] Modifications can be implemented to improve hydration in this system, such as employing elevated temperature operation to increase the partial pressure of water in the humidified feed or by incorporating an aqueous solution behind the anode, as is the case in the Exchange-MEA, which has the advantage of increased water supply and results in better membrane hydration, conductivities, current densities, and CO selectivity.[46,58]

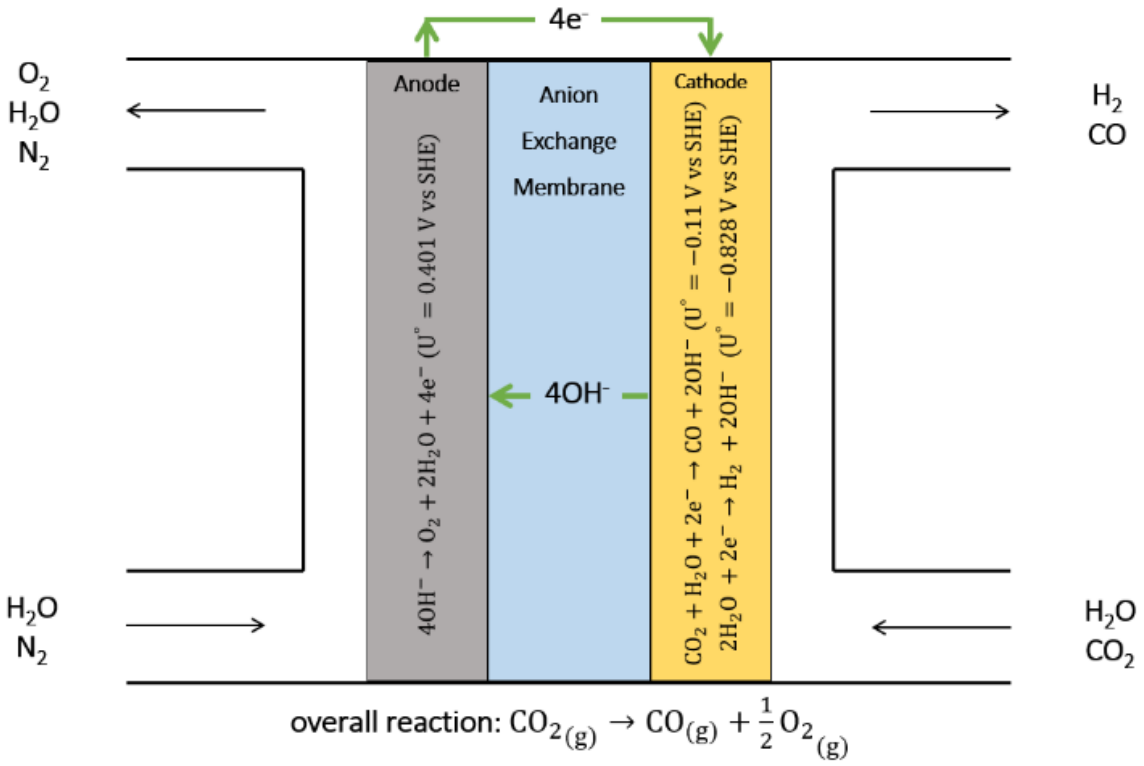

Figure 1.3. CO_2 reduction in the Full-MEA.

A schematic of a Full-MEA is shown in **Figure 1.3**: humidified gases are fed into both the anode and cathode and, with the application of an overpotential, the OER, HER, and COER reactions are facilitated in their respective catalyst layers, leading to the release of product gases. Each electrode consists of an appropriate electrocatalyst, ionomer, and gas-diffusion layer (GDL) or porous transport layer (PTL), with a selective AEM (anion exchange membrane) in between. In this architecture, gaseous CO_2 is fed into a gas-channel flow plate that distributes the reactant CO_2. The CO_2 diffuses through the porous transport layer (typically a fibrous carbon layer) thereby ensuring a uniform delivery of the CO_2 and electrons to the porous catalyst layer, where CO_2R occurs. The ionomer binds the particles and provides a pathway for ion conduction. An ion-exchange membrane is employed between the porous electrodes to facilitate ionic conduction between the electrodes, while simultaneously inhibiting product and electron crossover. At the anode, an aqueous exchange solution (typically either a hydroxide or a bicarbonate solution or simple pure H_2O) is fed through the porous support for the catalyst layer, wherein water oxidation occurs. The use of an aqueous environment at the anode substantially reduces the ohmic resistance of the overall cell by ensuring that the membrane is well hydrated.[46] It is important to note, however, that the high current densities achieved in the MEA can potentially induce high electro-osmotic fluxes that pull water away from the cathode catalyst layer, thus lowering its water activity;[59] such fluxes in constrained water environments, such as those in the ionomer polymer matrix adjacent to the electrocatalyst, could significantly skew the $[CO_2]$:$[H_2O]$ ratio in the catalyst-layer microenvironment.[60–62]

1.2.1 Relevant literature on CO_2R MEA devices

Recent work involving CO_2R MEAs (or MEA-like devices)[63,64] have explored the effects of electrocatalyst design and electrode configurations on MEA performance. There are currently fewer than thirty CO_2R MEA studies that investigate various concepts such as electrocatalyst metal selectivity,[65–71] materials or operating conditions,[71–73] C_{2+} selectivity enhancement strategies,[74–79] bipolar membrane configurations,[80,81] CO_2 purity effects,[82] bicarbonate[83] and CO/tandem[84,85] reduction, as well as relevant reviews,[86] with many using an Exchange-MEA architecture.[63,75,79] In addition, much can be learned from the wider low-temperature water electrolysis literature,[87] with research work on alkaline electrolyzer systems (AEMWEs: anion exchange membrane water electrolyzers) being much more relevant to CO_2R systems, due to their similar high pH requirements, than the more established acidic electrolyzer systems (PEMWEs: proton exchange membrane water electrolyzers).[88–93] However, few to none of the aforementioned CO_2R MEA studies have done an in-depth examination of the effects of perturbing integral aspects of the device system, specifically the elements and interfaces present in its ionomer-based catalyst layers.

1.3 The Catalyst Layer

The structure of MEAs used for COER and OER are depicted in **Figure 1.4**. For electrochemical reactions to occur, the catalysts must have access to unhindered electronic, ionic, and gas transport pathways: these pathways are provided by the conductive microporous and gas-diffusion layers, the hydrated ionomer, and the pore space network, respectively. The microporous layer (MPL) restricts the deposited catalyst to a defined region at the top of the gas-diffusion substrate, where it can have adequate contact with the membrane.

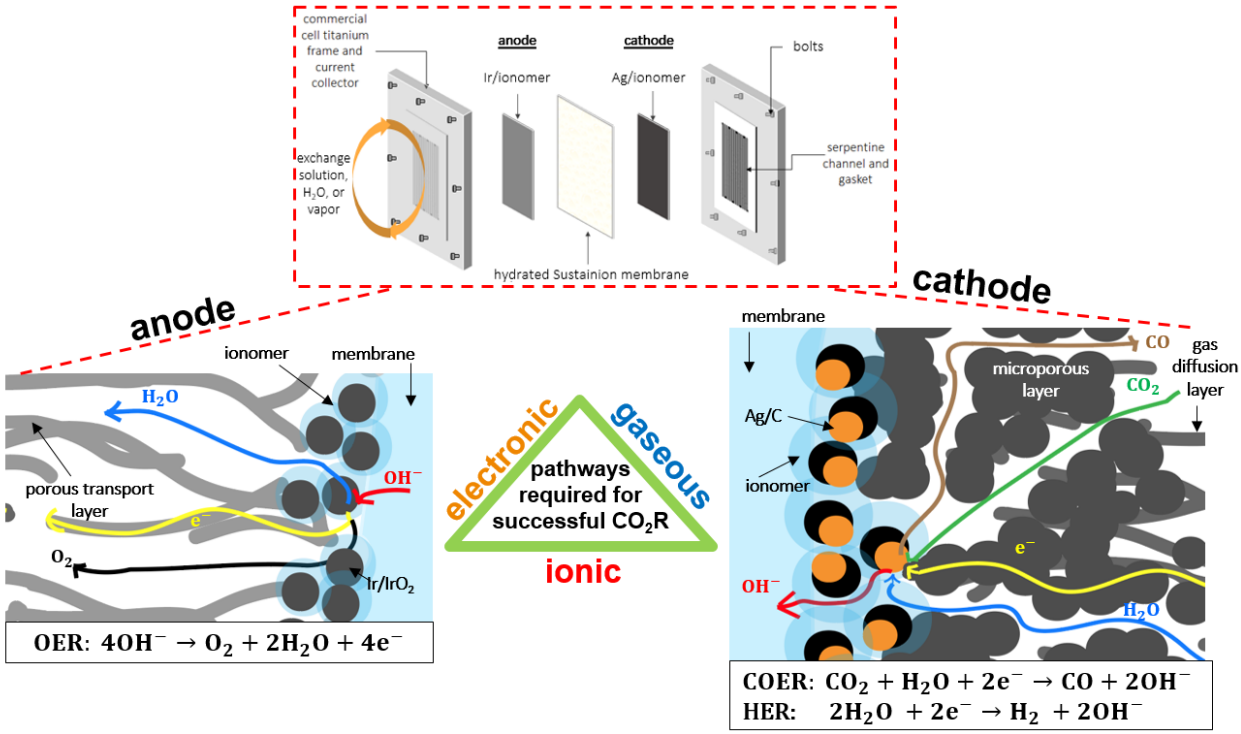

Figure 1.4. Schematic of the complex catalyst-layer microenvironments at the anode and cathode in the MEA. *Designs modified from Ref.* [58].

In addition, homogenous buffer reactions (see **Equations 1.5 thru 1.8**) can occur in the dissolved/hydrated ionomer phase, where CO_2 is consumed at the cathode and released at the anode. Based on a recent comprehensive modeling study, these processes present a potential major cause of poor CO_2 utilization in this system.[46]

Homogenous buffer reactions at the cathode

$$CO_2 + OH^- \leftrightarrow HCO_3^- \quad (1.5)$$

$$HCO_3^- + OH^- \leftrightarrow CO_3^{2-} + H_2O \quad (1.6)$$

Homogenous buffer reactions at the anode

$$HCO_3^- \leftrightarrow CO_2 + OH^- \quad (1.7)$$

$$CO_3^{2-} + H_2O \leftrightarrow HCO_3^- + OH^- \quad (1.8)$$

Compared to the anode CL, the cathode CL is known to be a more crucial and direct determinant of CO_2R MEA activity and selectivity.[62] For Ag electrodes, increasing the local CO_2 concentration or pH serves to maximize the CO:H_2 ratio, which leads to an enhancement in the rate of CO_2R relative to the rate of the HER.[94,95] The cathode CL microenvironment directly adjacent to the catalyst surface is also influenced by cation and anion identity, where, for aqueous CO_2R systems, it has been found that hydrated alkali metal (and anion) identity and size can greatly impact CO_2R selectivity and product formation via electrostatic interactions and surface coverages.[96–100] Moreover, the choice of ionomer composition greatly influences water and ion transport in the cathode CL, where the rate determining step is not CO_2 transport to the ionomer surface but rather its transport through the ionomer to the catalyst surface.[56,101,102] In addition, the pH differences between the choice of CEM (cation exchange membrane) ionomers like Nafion® vs. AEM (anion exchange membrane) ionomers like Sustainion® in determining water content, CO_2 solubility, and selectivity are also important to consider.[79,103] Thus, a wide range of interconnected phenomena are at play in the cathode CL that can influence overall CO_2R MEA performance.

1.4 Scope of Dissertation

This dissertation addresses two primary goals:

1. The development of an efficient and selective device for CO_2 reduction
2. The elucidation of the role of foundational catalyst-layer properties on CO_2R MEA performance

As noted in the preceding subsections, the catalyst layer in an MEA is quite complex and, as illustrated in **Figure 1.5**, the many interrelated physical phenomena occurring specifically in the cathode CL contribute extensively to overall MEA performance. Thus, the unifying theme of this dissertation is the elucidation of the roles of key component (ionomer, catalyst, water) interactions in the cathode catalyst layer of a CO_2R MEA and how an understanding of their underlying physics contributes to improved CO_2R performance and selectivity.

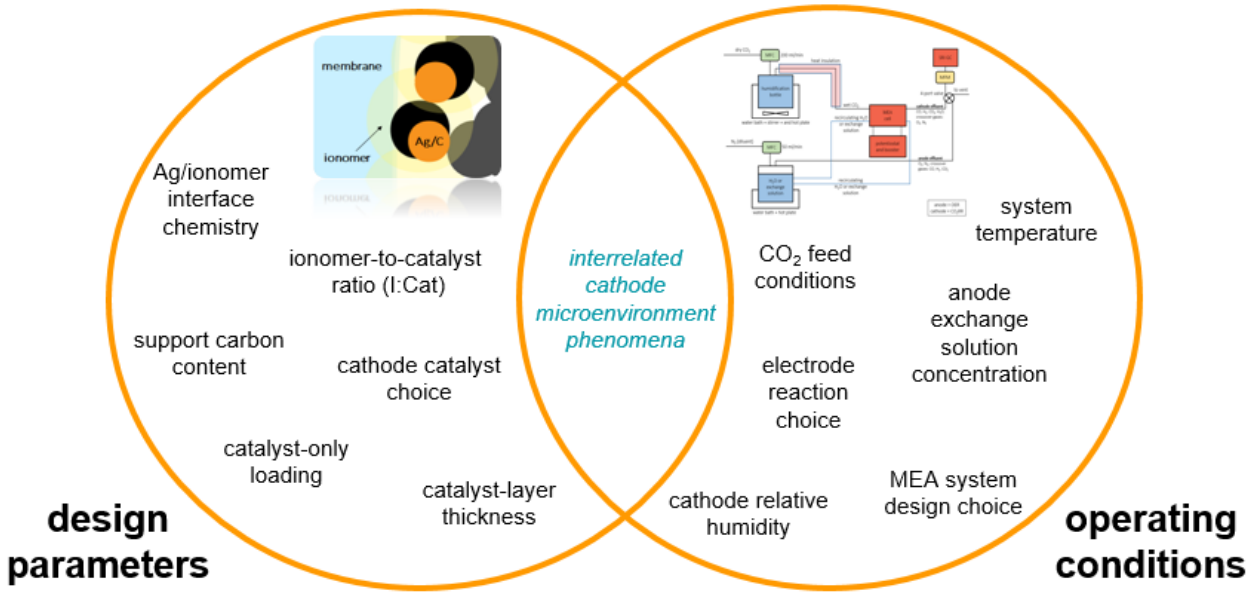

Figure 1.5. A Venn diagram depicting the various MEA research areas studied and documented within this dissertation. Both the design parameters and operating conditions explored influence the phenomena observed within the cathode catalyst-layer microenvironment and highlight its interconnected and complex nature. *Designs modified from Ref.* [58].

What follows are brief outlines of the contents of Chapters 2-5:

Chapter 2: Design and Engineering of the CO_2R MEA System

This chapter discusses recommended best practices and guiding principles discovered in the course of this dissertation project pertaining to MEA fabrication and testing, such as catalyst ink preparation, catalyst-layer deposition, choice of ionomer and membrane composition, and experimental methods used to obtain polarization curves and product selectivities. It also covers studies conducted on system-wide parameters, such as the effect of relative humidity and temperature changes on water management, and demonstrates a pathway towards reliable, reproducible, versatile, and scalable CO_2R MEA fabrication and operation.

Chapter 3: Tuning Catalyst-Ionomer Coverage and Interactions Towards Selective and High Current Density CO_2 Reduction

Critical components of the MEA catalyst layer are catalyst nanoparticles and ionomer, with the latter component providing a pathway for ion transport from the catalyst to the ion-conducting membrane. The foundational materials design parameters that characterize these ionomer-based catalyst-layers are the ionomer-to-catalyst ratio (I:Cat), catalyst loading, and catalyst-layer thickness. In this chapter, the effects of these parameters on the activity and product selectivity of a Ag cathode CO_2R MEA are systematically analyzed. An optimum I:Cat ratio of 3 is rationalized based on electrochemically-active surface area (ECSA) and ionomer coverage/distribution arguments, where the extent of this coverage and the resulting ionomer-catalyst interaction significantly impacts the total current density and CO selectivity. A range of ionomer coverages of catalyst particles was explored, extending from a patchy/sparse ionomer distribution at low I:Cat

ratios (*i.e.,* I:Cat < 3) – which have poor electrochemically active surface area (ECSA) and limited ionic pathways – to excessive coverages at high I:Cat ratios (*i.e.,* I:Cat > 3) that suffer from poor electronic contact and CO_2 utilization. The effect of decreasing the catalyst loading and/or catalyst-layer thickness changes mainly the CO_2R product selectivity (in agreement with previous modeling work) and the CO FE is shown to be highly sensitive to this metric. By changing these catalyst-layer design parameters, these results demonstrate that the MEA architecture can behave similarly to traditional aqueous electrolyte cells in their ability to tune CO_2R selectivity by an adjustment of the electrode/electrolyte interface. The crucial insights gained from the reported trends are compounded to yield an efficient Ag CO_2R MEA cell that operates at current densities of 200 mA cm^{-2} to 1000 mA cm^{-2}, CO faradaic efficiencies of 78 to 91%, and an area-specific resistance under 1 Ω cm^2. These findings can be applied to a broad range of CO_2R MEA-based devices, including CO_2-to-CO tandem devices and flexible manufacturing systems where changing the aforementioned catalyst-layer properties can effectively tune the outlet CO:H_2 ratio for various syngas applications.

Chapter 4: Studies on the Ag/ionomer Interface and its Impact in CO_2 Reduction Systems

A more in-depth understanding of the cathode catalyst-layer microenvironment and its catalyst/ionomer interfaces is essential and this chapter probes and characterizes these interfaces as they greatly impact CO_2R MEA activity and selectivity, considering that optimal CO_2R should stem from a cathode microenvironment with a high local pH and [CO_2]:[H_2O] ratio. It addresses how the choice of Ag/ionomer interface chemistry or pH influences modeled and experimental kinetic behavior, morphology, total current density, selectivity, and CO_2 crossover, as well as interfacial capacitance, establishing a more definitive link between macroscale MEA performance and fundamental multiphysics phenomena to help explain previously observed CO_2R behaviors.

Chapter 5: A Pathway to Industrial Carbon Neutrality: Summary and Future Perspectives on CO_2 Reduction in MEA Devices

This final chapter succinctly summarizes the preceding chapters and provides an in-depth exploration of important open questions the CO_2 electrosynthesis field can address in the near- and medium-term. Various improvement and optimization efforts towards scaled commercial deployment of CO_2 reduction devices, such as inlet feed perturbation studies and single-cell design changes, are discussed and more fundamental work, such as catalyst ink, applied-voltage-breakdown, and model system studies, is also suggested for exploration.

2 Design and Engineering of the CO_2R MEA System

† Portions of this chapter were previously published as "**O. Romiluyi**, N. Danilovic, A. T. Bell, and A. Z. Weber, "Membrane-electrode assembly design parameters for optimal CO_2 reduction", Electrochemical Science Advances, ISSN: 2698-5977, 2698-5977; DOI: 10.1002/elsa.202100186 (2022)" and are adapted with permission from all co-authors.

2.1 Introduction

The current chapter examines the essentials involved in fabricating an MEA, starting from its components (catalyst layer/ink, electrode substrate, membrane), then moving to the catalyst-layer deposition method and cell assembly. Water management in the MEA and the choice operating parameters used to acquire the results presented in Chapters 3 and 4 are also described, as well as the justification for materials selection and experimental methodologies.

2.2 Catalyst-Layer Fabrication

Both the anode and cathode in the MEA consist of a porous, conducting material onto which the catalyst layer is deposited. The following subsections detail how each of these electrode components are constructed.

2.2.1 Electrode substrate preparation

The material used for each electrode differ so as to meet the requirements of its working environment. A porous, carbon-based gas-diffusion layer (GDL) is used for the cathode substrate, while a titanium porous transport layer (PTL) is used for the anode substrate because this electrode operates under highly oxidizing conditions. Both layers possess good electrical conductivity and high surface area. Both electrodes are cut to a 5 cm^2 geometric/active area, inspected for defects, and cleaned using ultra-pure nitric acid to remove any electrochemically-active trace impurities.[104] In order to obtain accurate loading measurements before catalyst-layer deposition, the dry weight of the electrode must be obtained. This is achieved by heating the electrode on a hot plate and recording its weight after any residual moisture has been evaporated.

2.2.2 Catalyst ink preparation

Formulation of the catalyst ink is very important because its properties impact the properties of the catalyst layer. The major components in each catalyst ink are (1) the catalyst nanoparticles, either unsupported or supported with a high surface area material such as Vulcan® carbon, (2) the alkaline or acidic ionomer solution, which is typically dissolved in ethanol, and (3) the solvents for both organic (n-propanol, iso-propanol, ethanol) and inorganic (pure water) ink components. The relative loadings of catalyst, carbon support, and ionomer determine the degree of ionic, electronic, and gaseous transport in the catalyst layer, especially in the cathode catalyst layer where CO_2R occurs.[58] Based on recent work,[58] an intermediate amount of ionomer relative to catalyst (*i.e.,* I:Cat ratio) and a relatively low catalyst-only loading for the cathode catalyst ink

are highly recommended. An insufficient or excessive ionomer content or catalyst-only loading leads to myriad inefficiencies in ionic and electronic ECSA and CO_2 mass-transport and utilization, resulting in suboptimal CO_2R performance.[58] Solvent quantities can be determined after the desired ionomer and catalyst quantities have been established; the relative solvent volume required depends on the number of sprays and spray duration. Although a nominal water-to-propanol ratio of 1 (weight basis) is often used, the solvent quantity has its own set of requirements and considerations: (1) for spray coating, the ratio of solids (catalyst, carbon) to solvent must be kept below 0.4% in order to avoid clogging of the spray nozzle, (2) an ink volume in excess of the calculated amount is required in order to account for the ink loading line volume, overspray, and any minor spills that may occur, and (3) the ionomer:solvent ratio determines the viscosity of the ink and its evaporation characteristics, which in turn determines the catalyst-layer porosity, morphology, and subsequent CO_2R MEA current-voltage response.[105–109] Once these quantities (on a weight basis) have been determined, the catalyst (supported or unsupported) must be added into the ink vial first, with care taken to avoid transfer losses, especially for catalysts supported on carbon, since the carbon tends to adhere to surfaces. Pure Milli-Q® water is then added and the catalyst/carbon/water mixture is vigorously mixed to facilitate dissolution of the inorganic components. Organic solvents, such as n-propanol, iso-propanol, or ethanol, can then be added to the container, followed by the desired quantity of ionomer solution. This is done by careful pipetting (to avoid overshooting because ionomer solutions can be quite viscous) and then a swirling of the ink vial to facilitate mixing of the organic components. Care is taken to use impurity-free utensils and to avoid cross-contamination between utensils throughout this ink preparation process.

After the catalyst ink for each electrode has been prepared, it is sonicated to ensure adequate mixing of the components and to reduce the extent of particle settling and agglomeration. For cathode catalyst inks containing Ag, Au, Pt, or Cu, using a beaker sonicator for at least 30 min is sufficient, with enough water available in the sonication beaker to completely cover the ink level in the vial. However, for Ir inks used for the anode electrode, a more powerful probe sonicator is used because this ink tends to agglomerate easily and can be less stable when present in higher concentrations.[110] The ink vial is submerged in an ice bath beneath the probe tip (covered and secured with a parafilm) in order for the temperature of the ink to be moderated since the frictional heat generated from the rigorous sonication process could lead to ionomer deformation or denaturing.[111] The ice bath level should again cover the ink level in the vial and the ice level and content should be monitored and maintained throughout the sonication process. The probe sonicator controller power/amplifier level is typically 20% or 38% (depending on the level of sonication desired) and the sonication duration is typically 30 min. After probe sonication, the Ir ink is then placed in a beaker sonicator for 1-2 min, with an ice bath, to finalize the mixing process.

To assess the average particle size of the nanoparticles in the as-prepared inks and the degree of stability of the ink, dynamic light scattering (DLS) can be used. This technique enables assessment of critical factors such as ink component quantity (*i.e.,* ionomer, catalyst, or support carbon content) on particle size, as well as solvent content and ink age on ink stability. It is highly recommended that the catalyst ink be made the same day as it is used for deposition in order to minimize particle settling, particle instability, and agglomeration/aggregation, which can take place in as little as a couple of hours for some catalysts. If this is found to be the case, the ink recipe, specifically the volume of solvents, and the ink preparation process should be revised accordingly.

2.2.3 Spray coating deposition procedure

A retrofitted Sono-Tek® spray coater, shown in **Figure 2.1**, was used primarily to deposit layers of as-prepared catalyst ink onto porous electrodes.

Figure 2.1. Sono-Tek® spray coater test station used for MEA fabrication.

Key elements of the instrument include an automated spray program (*i.e.,* PathMaster®), ink loading and syringe pump system, and a vacuum hot plate. A vacuum of ~1 bar is applied to the spray area to keep the substrate, especially carbon GDLs, from being shifted or blown away by the spray stream/shaping air, as well as to keep membranes flat and prevent them from buckling during the preparation of catalyst-coated membranes (*i.e.,* CCMs). A spray temperature of 90ºC is used since it facilitates sufficiently rapid evaporation of solvents in the ink after deposition and avoids liquid pooling on the electrode active area. Separate ink lines are used for each catalyst ink to avoid major cross-contamination. To facilitate vacuum during spray coating, gasketing materials are used both above and underneath the electrode substrate: a porous fibrous gasket is placed beneath the substrate and a non-porous fibrous gasket is placed on top, with a section cut out to match the approximate size of the substrate active geometric area. The porous material on the bottom allows the substrate to be pulled by the vacuum directly underneath and protects the substrate from any contamination on the vacuum plate. The non-porous material on top acts as a mask and ensures a clean, well-defined spray area. A much larger and thicker PTFE gasket, with a section cut out to a size slightly larger than the substrate areas being sprayed, is placed on top of the gasket/substrate assembly. This thick gasket is needed to ensure a proper seal against the vacuum plate and for protection from its hot surface and it must not contact any membrane substrates since ink leaching could occur. If a good seal is made, the pressure on the vacuum pump below should read between 0.8 and 1 bar and the seal should be adjusted if this is not the case.

The PathMaster® spray program used is based on a larger area than the substrate being spray coated to ensure uniform catalyst-layer deposition and to avoid edge effects, especially for spraying on membranes. For example, if the substrate is 5 cm^2, the PathMaster® program and the prepared ink volume should be sufficient to spray at least a 7.5 cm^2 area to account for overspray, the ink line volume, and any minor spills/losses during the spray process. Recommended settings for the spray program and tools are given in **Table 2.1**. After the spray program has concluded, the substrate should be weighed (or returned for further ink deposition) until the desired loading has been achieved. The ink lines used during the spray should be thoroughly flushed with isopropanol and air several times to remove residual ink and to prevent future contamination between sprays. Proper ink waste handling, safety, and housekeeping procedures should also be adhered to.

Component	Recommended Settings	Relevant Notes
125 kHz nozzle	• Path speed: 10 - 50 mm s^{-1} (depending on substrate) • Ink deposition rate: 0.1 - 0.2 mL min^{-1} • Nozzle tip height (above vacuum plate): 40 mm • Shaping air (N_2) = 1.0 - 1.1 kPa • Run power = 2.06 W • Idle power = 0.75 W	The 125 kHz high-frequency nozzle allows for a higher degree of atomization of the catalyst ink (*i.e.,* more well-dispersed sprays).
25 kHz nozzle	• Path speed: 25 mm s^{-1} (depending on substrate) • Ink deposition rate: 0.2 mL min^{-1} • Nozzle tip height (above vacuum plate): 40 mm • Shaping air (N_2) = 0.96 kPa • Run power = 4.60 W • Idle power = 0.75 W	
Membrane spraying	• Ink deposition rate: 0.1 - 0.2 mL s^{-1} • Path speed: 25 mm s^{-1}	A higher shaping air pressure can cause deposited nanoparticles to be dusted up during the spray, resulting in major material loss. Depending on the weight of the substrate, a high shaping air pressure could also shift or blow away the substrate from the spray area, if it is not securely vacuum sealed. Thus, ink deposition rates and path speeds may need to be optimized for specific substrates.
Gas-diffusion layer spraying	• Ink deposition rate: 0.2 mL s^{-1} • Path speed: 25 mm s^{-1} or 50 mm s^{-1}	

Table 2.1. Recommended settings for Sono-Tek® spray coating procedure.

2.3 Membrane Selection

The choice of membrane for use in the CO_2R MEA is also important as it influences the pH in the catalyst layers and determines the selectivity of ion species transferring between the electrodes, which influences macroscale metrics such as CO_2 crossover, utilization, and activity. These effects are also part of the findings presented in Chapter 4. An alkaline environment has been found to be superior for CO_2R across a range of devices[34,40–44] and thus, experiments were conducted to benchmark and compare the performance of state-of-the-art AEM ionomer and membrane configurations. The experiments were conducted using water electrolysis as a reaction system: the AEM system with the best performance in a water electrolysis hydroxide pump reaction system (*i.e.,* HER at the cathode, HOR at the anode) would potentially have the necessary membrane/cathode catalyst-layer interface microenvironment for optimal activity in a standard CO_2R reaction system (*i.e.,* CO_2R at the cathode, OER at the anode). For the water electrolysis hydroxide pump, Pt was used as the catalyst at both the anode and cathode (at relatively low loadings and moderate I:C or I:Cat ratios[58]) in order to facilitate efficient HER and HOR, respectively (see **Equations 2.1. thru 2.4**). With HOR at the anode, a pseudo-reference (DHE) reference was created with much lower overpotentials closer to 0 mV than with OER used in standard CO_2R MEA systems, allowing for a more accurate empirical measure of the cathode overpotential to be derived.

$$\text{CEM HER: } 2H^+ + 2e^- \rightarrow H_2 \ (U^\circ = 0 \text{ V vs. SHE}) \tag{2.1}$$

$$\text{CEM HOR: } H_2 \rightarrow 2H^+ + 2e^- \ (U^\circ = 0 \text{ V vs. SHE}) \tag{2.2}$$

$$\text{AEM HER: } 2H_2O + 2e^- \rightarrow H_2 + 2OH^- \ (U^\circ = -0.83 \text{ V vs. SHE}) \tag{2.3}$$

$$\text{AEM HOR: } H_2 + 2OH^- \rightarrow 2H_2O + 2e^- \ (U^\circ = 0.83 \text{ V vs. SHE}) \tag{2.4}$$

Three different AEM ionomer and membrane systems were studied: Sustainion®, Georgia Tech® (GT), and Versogen® (W7). The different properties and the polymer chemistries of these systems, as well as that of Nafion®, are shown in **Table 2.2**. The AEM membranes were each pretreated in 1 M KOH for at least 24 h and rinsed several times with Milli-Q® water before cell testing.

Membrane	Backbone	Function group	Dry thickness (μm)
Sustainion®	polystyrene	imidazolium	50
Nafion®	polytetrafluoroethylene (PTFE)	sulfonate	50
Versogen® (W7, PiperION)	poly(aryl)	piperidinium	30
Georgia Tech® (GT)	poly(norbornene)	quaternary ammonium	30

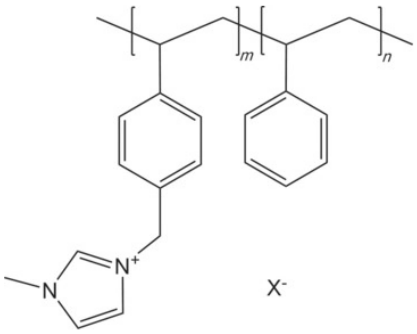

Sustainion®

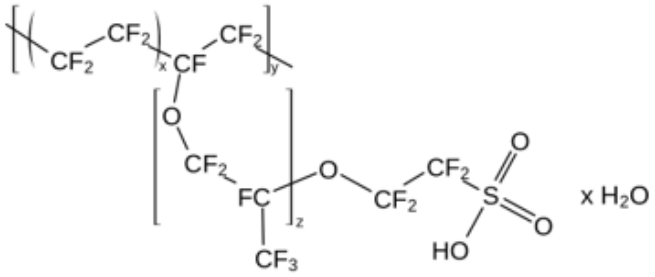

Nafion®

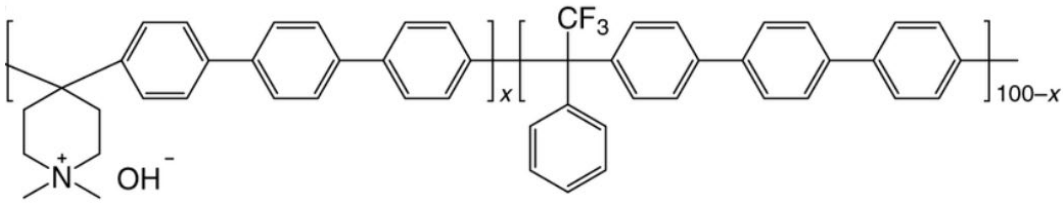

Versogen® (W7, PiperION)

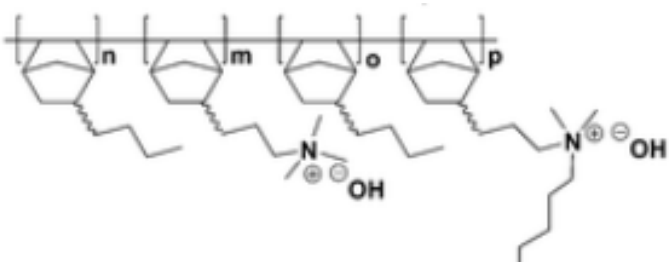

Georgia Tech® (GT)

Table 2.2. Various membrane and ionomer polymer chemistry systems and their respective properties. *Structures obtained from Ref.* [112–116]

Figure 2.2 shows the recorded polarization activity of all three AEM systems, with the Nafion/CEM system included for reference. MEAs based on GDE-deposited CLs, which used either W7 or Sustainion as the membrane, had comparable performance across the potential window, indicating that both polymer systems conduct the aforementioned reactions at similar efficiencies despite having very different polymer chemistries. The GT membrane performed the least effectively (*i.e.,* exhibited the lowest current for a given cell voltage) at most voltages but appeared to outperform the other two systems at higher voltages. In addition, various combinations of the AEM configurations were attempted (*e.g.,* Sustainion ionomer with W7 membrane), but such systems proved too incompatible, resulting in very poor performance. Thus, selecting Sustainion as the AEM for both water electrolysis, and CO_2R by extension, is justified.

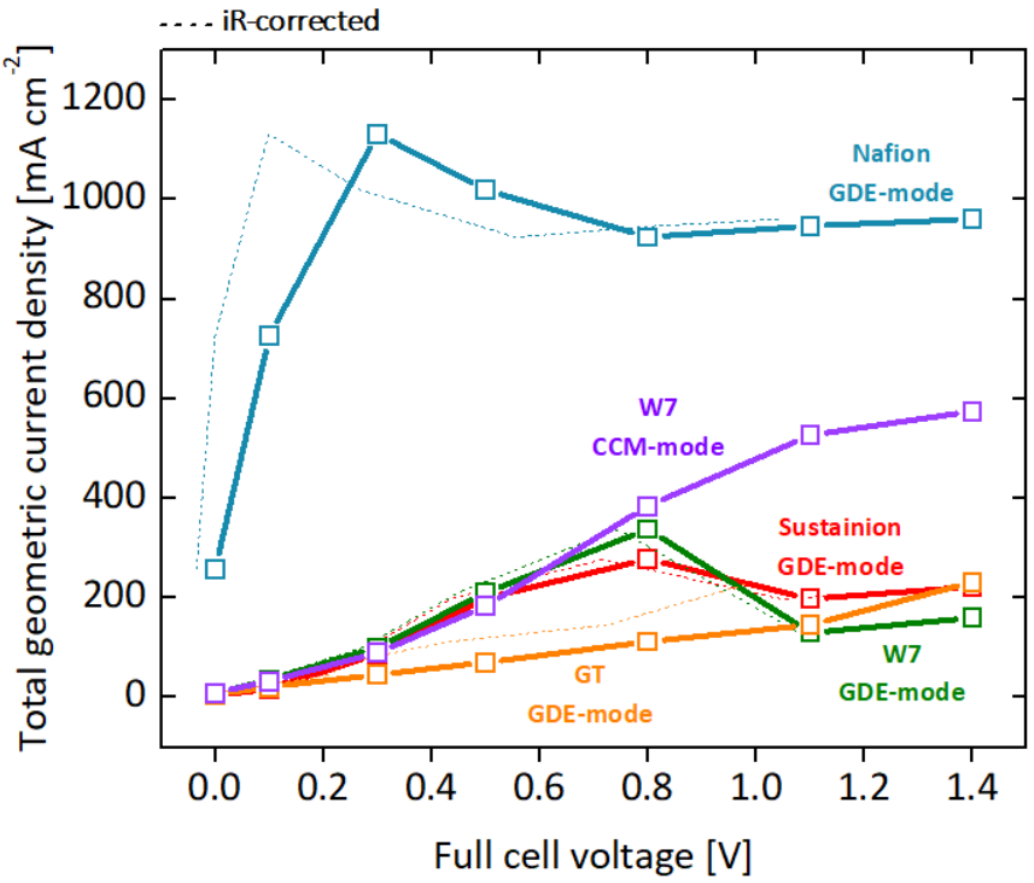

Figure 2.2. Polarization curves for various AEM ionomer and membrane systems. A CEM/Nafion system was also tested for reference. Test conditions: 80°C system temperature, Full-MEA configuration, 100% RH at both electrodes, HER at the cathode (flowing gas: Ar at 200 ml min^{-1}), HOR at the anode (flowing gas: H_2 at 200 ml min^{-1}), Pt/C weight fraction of around 46%, I:C (ionomer-to-carbon) ratio was 0.6, and Pt-only loading was 0.3 mg_{Pt} cm^{-2} for both anode and cathode. The following systems are depicted: (1) Nafion®: Nafion 212 CEM and Nafion ionomer, GDE-mode (2) Versogen® (W7): W7 30μm AEM and ionomer, CCM-mode and GDE-mode, (3) Sustainion® system: Sustainion AEM and Sustainion ionomer, GDE-mode, and (4) Georgia Tech® (GT): GT 72-10 membrane and GT 72-5 ionomer, GDE-mode.

2.3.1 CCM vs. GDE catalyst-layer deposition

Good contact between the membrane and the catalyst layer is important as this determines the current-voltage response of the resulting MEA, particularly its ohmic characteristics. Thus, the mode of MEA fabrication was also investigated: a catalyst-coated membrane (CCM) vs. a catalyst-coated gas-diffusion electrode (GDE), both fabricated via spray coating. The W7 membrane was used for this comparison (its CCM fabrication is depicted in **Figure 2.3**) due to its ability to withstand direct heat during spray coating. Higher MEA activity was demonstrated by the CCM-mode W7 system, as shown in **Figure 2.2**: it yielded better performance than the GDE-mode W7 system (which had the same polymeric components) and the other AEM GDEs. This confirms that much improved membrane/catalyst-layer contact (and lower contact resistances) was established via CCM fabrication, wherein the catalyst ink is deposited directly onto the membrane as opposed to onto a GDL.

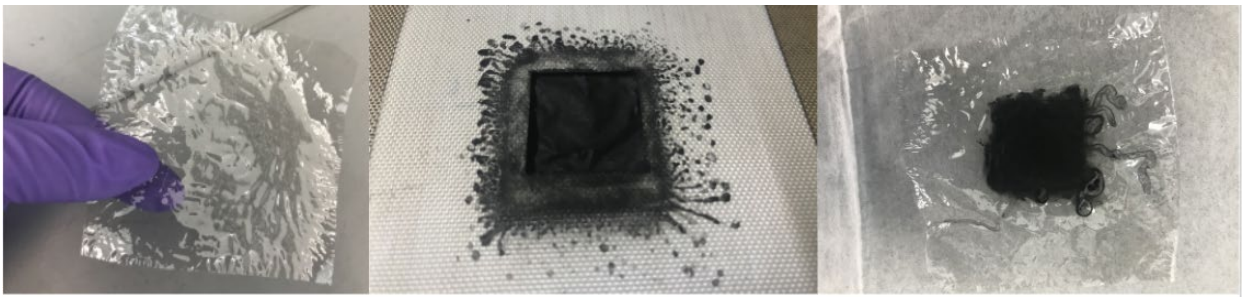

Figure 2.3. Photo of catalyst-coated Versogen® (W7) membrane preparation process. Wet, as-received W7 30 µm membranes were used for CCM sprays and the spray coating temperature was maintained at 40°C. The catalyst ink recipe was modified to allow for a 90:10 nPA:water ratio in the prepared ink, which allowed for visibly improved ink solubilization/stability and better evaporation despite the lower spray temperature and lack of vacuum.

2.4 MEA System Operation

After the membrane is selected and the catalyst layer for each electrode has been fabricated, the MEA is ready to be assembled into a cell system. The following subsections outline the assembly and operating procedure, as well as recommended best practices and guidelines.

2.4.1 Cell assembly

Before cell assembly, each cell component (end plate, current collector, O-rings, gas tubes, gaskets flow field, cell heater) is cleaned to remove impurities. As shown in **Figure 2.4**, the membrane is sandwiched between the two catalyst-coated electrodes and the resulting MEA is placed into a 5 cm^2 commercial cell (Fuel Cell Technologies®). The membrane is cut to an area larger than the geometric/active area to allow room for slight shifting of components during assembly and to avoid edge effects. In addition, care must be taken to avoid cross-contaminating the membrane with used utensils or puncturing/damaging the membrane during treatment or assembly since the resulting pin-hole defects and tears could lead to increased CO_2 crossover, cell shorting, and poor performance.[117] A torque wrench is used to tighten each cell bolt to 40 in-lb in 10 in-lbs increments per bolt, which is done by placing the cell in a vice grip. This procedure ensured even distribution of pressure across the cell and allowed it to be tightened reproducibly. Under-tightening or over-tightening the assembly can lead to cell failure, leaks, poor performance, and safety issues. PTFE gaskets are used on each gas channel to ensure reproducible and uniform compression across the MEA during assembly and to prevent leakages.

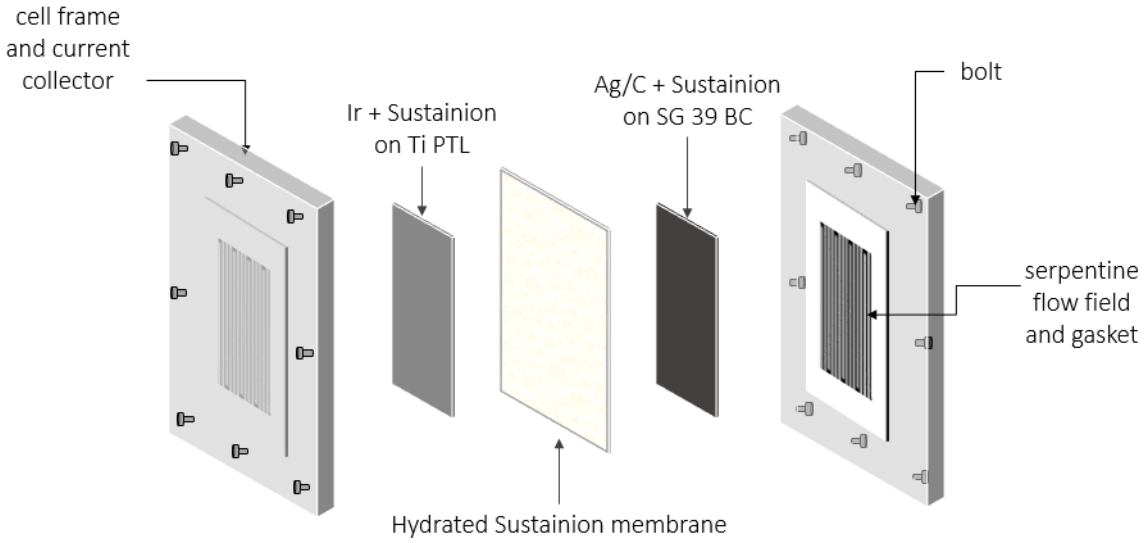

Figure 2.4. MEA electrolyzer, exploded view. The 5 cm^2 commercial cell was purchased from Fuel Cell Technologies®. Each electrode (Ir anode and Ag cathode) was 5 cm^2 with the anode substrate being a titanium porous transport layer (PTL) and the cathode substrate is a carbon gas-diffusion layer (GDL). A 50 µm hydrated Sustainion membrane is sandwiched between the two electrodes and single serpentine gas channels, with the assembled cell being compressed under a 40 in-lb torque. *Schematic used with permission from Ref.* [58].

A photo of a disassembled MEA electrolyzer cell is shown in **Figure 2.5**. The graphite gas-channel flow field, gold-plated current collector, and aluminum endplate components of each electrode should be aligned using the provided alignment pins and holes so that both electrode catalyst layers fully cover the gas-channel active area. This is important since exposed edges or misalignments in the MEA can cause gas or liquid leaks, as well as poor performance, shorting, overheating, and potential fire hazards. All connections should be tight and secure, with attention paid to any leaks, cracks, or damage to lines that could occur because of misalignment during cell assembly, worn gaskets, or over- or under-tightening of the cell screws.

Figure 2.5. Components of the 5cm^2 CO_2R electrolyzer used: the aluminum end plates, gold-plated current collectors, graphite gas channels, bolts, and other key components are visible. This set-up was used in obtaining the data for a previous study.[58] *Photo credit: Jeremy Snyder, LBNL (2022)*

2.4.2 Operating conditions

Figure 2.6 and **Figure 2.7** show a schematic and a photo of the CO_2R MEA electrolyzer test system, respectively. The CO_2 entering the cathode compartment was humidified via bubbling through a bottle of Milli-Q® water maintained at a desired system temperature using a hot-water bath. A flow of pure water or ion solution at the desired system temperature was fed and recirculated behind the anode as the MEA exchange solution using a peristaltic pump. The MEA cell itself was also heated and maintained at the desired system temperature. A cathode feed flow rate of at least 200 mL min^{-1} of humidified CO_2 (measured using a mass-flow controller) was used in order to avoid reactant supply limitations and mass-transfer effects stemming as a consequence of large fractional conversions. The exchange solution fed behind the anode was also circulated rapidly so that concentrations in the gas channels and porous electrodes remained uniform and gradients were minimized. Flow rates of the cathode and anode outlet gases were verified using mass-flow meters (MFM) to ensure no leakages across the entire system and for faradaic efficiency (FE) calculation purposes.

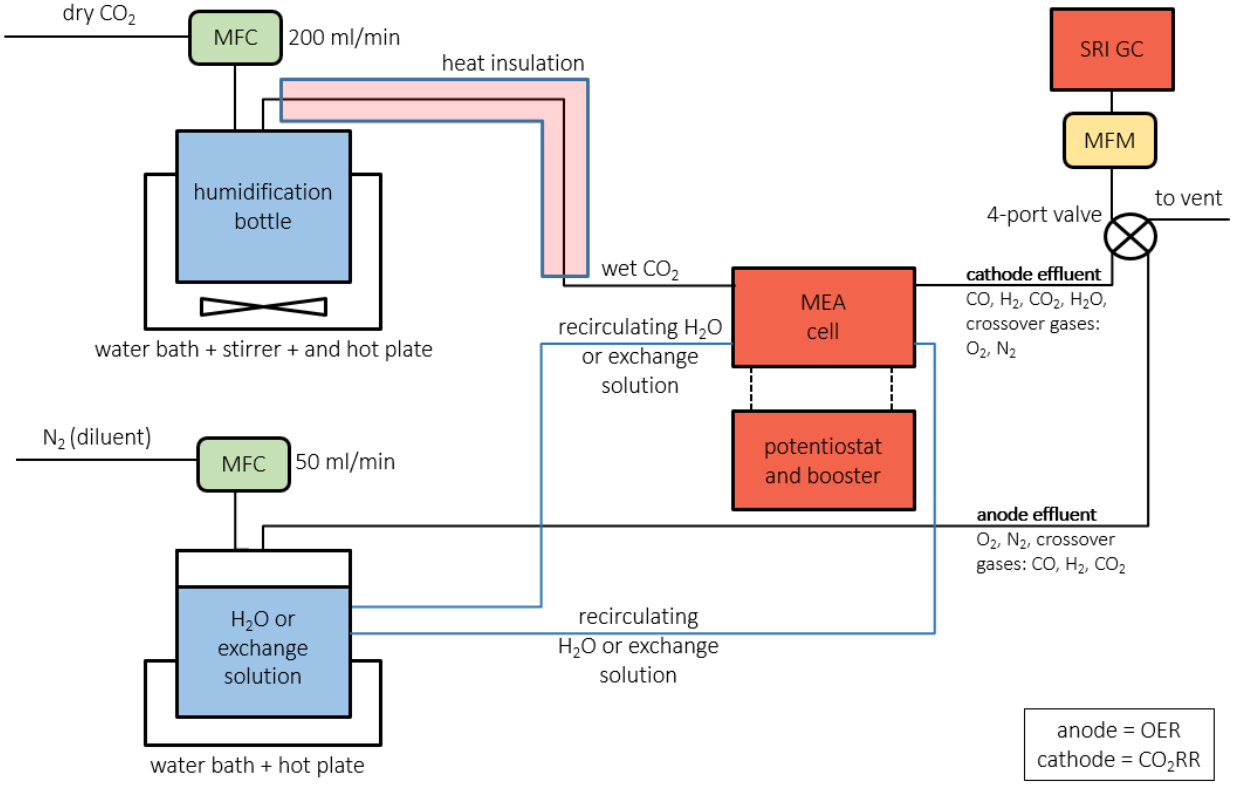

Figure 2.6. CO_2R MEA experimental system. The experimental set-up was built for operation between the H_2O-MEA or Exchange-MEA modes and with a gas humidification system at the cathode. Hot plates, cell heating, and heat insulation for gas flow were used to maintain thermal settings. At each cell potential, both the cathode and anode gas effluents were analyzed in-line with the GC using a 4-way valve. *Schematic used with permission from Ref.* [58].

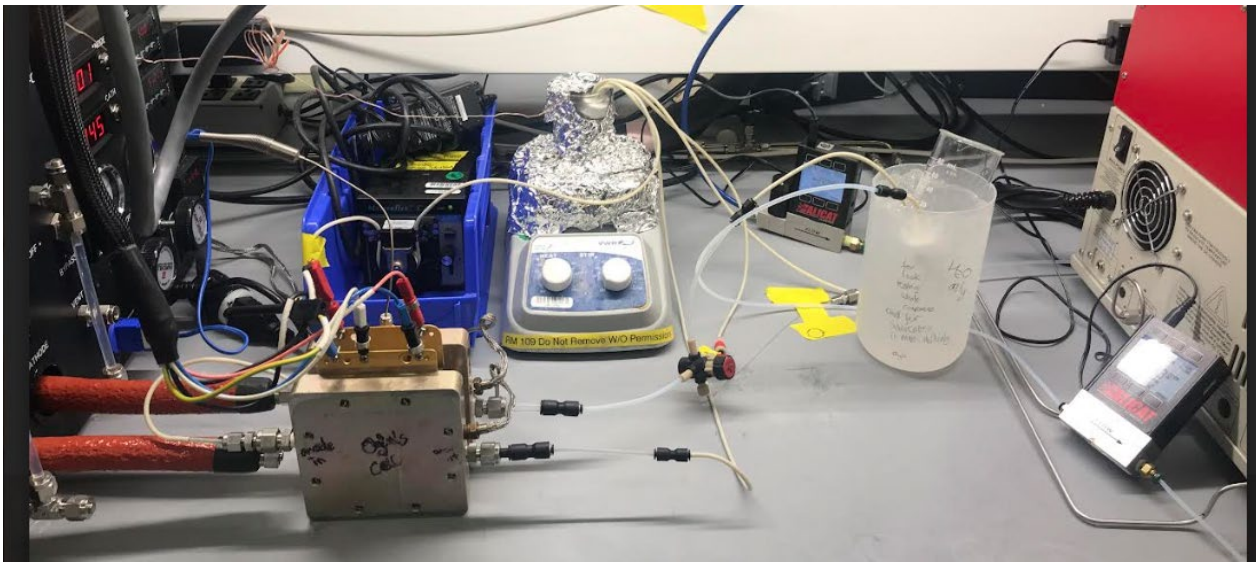

Figure 2.7. Custom-built CO_2R electrolyzer test station system. This set-up was used in obtaining the data for a previous study[58], as well as the other contents of this dissertation.

2.4.2.1 Anode exchange solution system

The anode exchange solution container was immersed into a hot-water bath, with ports for a nitrogen purge line, an outlet line leading to a gas chromatogram (GC) for gas analysis, and inlet and outlet lines for the peristaltic pump that allows for anode exchange solution recirculation. The exchange solution should be sparged with nitrogen to prevent CO_2 contamination of the solution being introduced into the MEA system. The hot-water bath used for thermal control of the anode exchange solution has a water level that is sufficient to completely cover the solution container. To avoid inclusion of gaseous or liquid products accumulated from previous electrochemical runs, refreshing the feed solution after each voltage/current measurement is important. Thus, ample exchange solution should be prepared beforehand, ready for frequent pipette transfer into the container. After operation, the peristaltic pump is run in reverse to transfer any remaining exchange solution from the anode chamber back into the solution container in the water bath. Milli-Q® water should then be used to flush both the anode and cathode feed and outlet lines of used solution and to ensure that the lines are cleaned and free of contamination between runs.

2.4.2.2 System humidification

Figure 2.8 shows the electrolyzer connected to the humidification test station in a vertical alignment.[71] Once the MEA electrolyzer is assembled, the anode inlet is connected to a peristaltic pump or a humidification gas line, depending upon the choice of MEA configuration (*i.e.,* Full-MEA or Exchange-MEA). After the gas/liquid line connections are secured, the thermocouple from the humidification station adjacent to the cell is connected to measure and regulate the cell temperature. System and cell temperatures and relative humidities can be controlled manually on the humidification station or remotely via a LabVIEW® program.

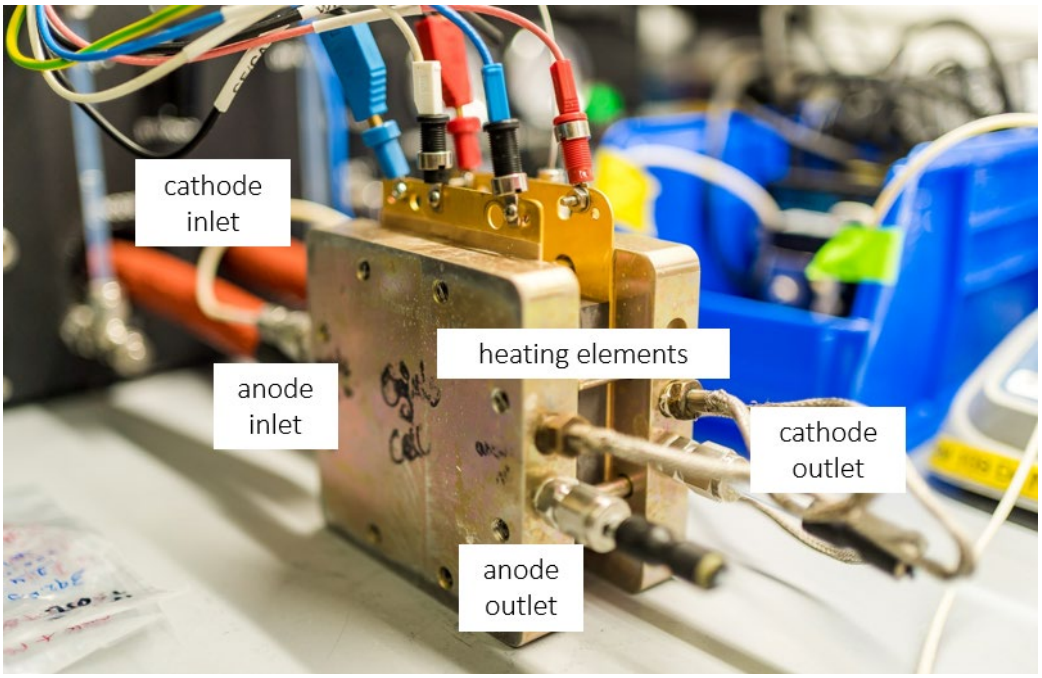

Figure 2.8. Fully-connected CO_2R MEA electrolyzer, ready for experimentation. This set-up was used in obtaining the data for a previous study.[58] *Photo credit: Jeremy Snyder, LBNL (2022)*

2.4.2.3 Gas and liquid product sampling and measurement

An SRI® GC (gas chromatograph) is used for gas analysis of gaseous CO_2R products (carbon monoxide, hydrogen, methane, ethane, and ethylene) using both an FID-methanizer (flame ionization detector for detection of carbon-containing/combustible compounds) and a TCD (thermal conductivity detector for detection of hydrogen, nitrogen, and oxygen). CO_2 peaks can also be measured using the appropriate PeakSimple® GC control file and this is most useful for measuring CO_2 crossover occurring at the anode electrode. Once a desired temperature program for the GC is set (an 80°C isothermal program was typically used), a time per injection can be determined. For example, an optimal elution time for all the gases is approximately 8 min when an isothermal (80°C or 90°C) temperature program is used and, thus, doing single injection gas analyses for both electrodes will take a minimum of 16 min per voltage/current measurement. Extra time should be factored in to account for time taken to collect liquid condensate (if required) and refresh the anode solution before the next voltage/current step begins. This timing sequence is reflected in the associated EC-Lab® method used during electrochemical measurements. A manual IDEX® 4-way gas switching valve, located upstream of the GC, is used to direct gases either to an exhaust vent or to the inlet of the SRI® GC, which has an outlet that also goes to the exhaust vent. When CO_2R product gases need to be tested for either electrode (including those that crossover to the anode), the 4-way valve can be timed to switch ~3 min before the programmed GC injection. This allows enough time for previously injected gases to be flushed out and replaced with the new product gas composition before the next GC injection. All gas streams go through an ice-trap before entering the GC inlet in order to avoid a large amount of water vapor being injected into the column. This procedure also allows any liquid products made during CO_2R, such as ethanol, 1-propanol, and formic acid, to be collected as a liquid condensate that can be subsequently analyzed via HPLC (high-performance liquid chromatography) (or NMR (nuclear magnetic

resonance) spectroscopy, if desired). The ice-trap comprises a bottle with inlet and outlet ports that has sufficient tubing coiled inside it to allow the flowing gas to be cooled and the condensable products to accumulate. In between voltage/current step measurements, the condensate is collected with a pipette and dispensed into HPLC vials for storage in a refrigerator until all liquid samples can be run at one time. The exiting gas streams also pass through an MFM before entering the GC, allowing the flow rate of the dry gas mixture to be measured and used for leakage checks during experimentation and for post-experimental calculations such as faradaic efficiencies.

2.4.2.4 The effect of relative humidity

CO_2R MEA performance can be influenced substantially by the degree of ionomer and membrane hydration, where insufficient hydration can lead to non-optimal performance.[46,58,71,72,81] In order to elucidate the impact of relative humidity (RH) on MEA activity, studies for a range of asymmetric and symmetric relative humidity profiles at both electrodes were conducted. RHs over 100% were achieved via an inlet line temperature that was set higher than the cell temperature, while RHs less than 100% were achieved via inlet line temperatures that were set lower than the cell temperature.

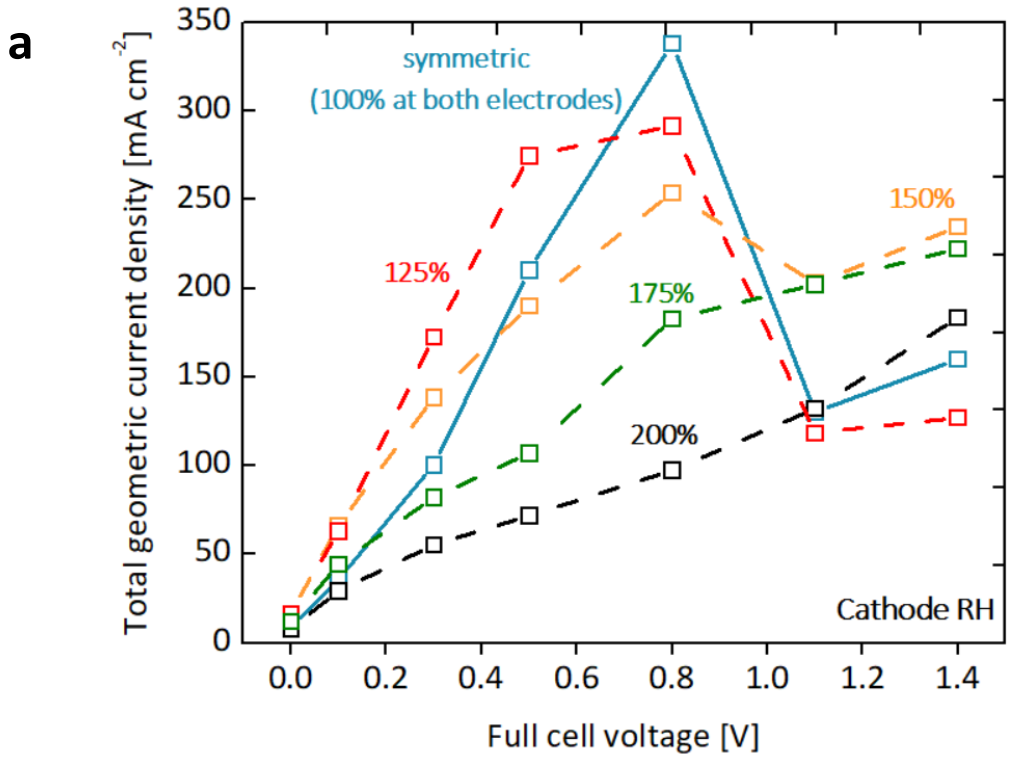

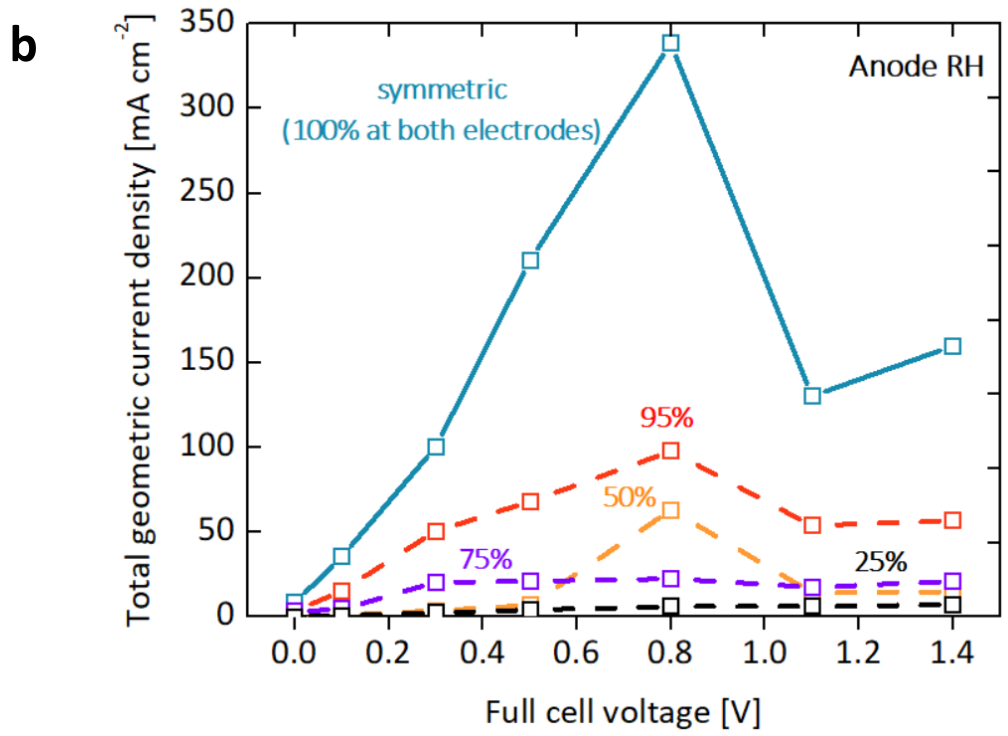

Figure 2.9. Polarization curves showing various cathode (a) and anode (b) relative humidity profiles. Test conditions: 80℃ system temperature, Full-MEA configuration, HER at the cathode (flowing gas: Ar at 200 ml min^{-1}), HOR at the anode (flowing gas: H_2 at 200 ml min^{-1}), Pt/C weight fraction of around 46%, I:C (ionomer-to-carbon) ratio was 0.6, and Pt-only loading was 0.3 mg_{Pt} cm^{-2} for both anode and cathode. A Versogen® (W7) W7 30µm AEM and ionomer fabricated in GDE-mode was used.

A Full-MEA performing water electrolysis (with HER at the cathode and HOR at the anode) and using a GDE-mode Versogen® (W7) membrane and ionomer system was chosen as a test-bed. The RH profile that yielded the highest current for a given cell voltage for water electrolysis was assumed to also perform most favorably for CO_2 reduction, for which water is a primary and potentially limiting reactant. Considering that water is consumed at the cathode and produced at the anode for both water electrolysis and CO_2R, specifically at the alkaline conditions of interest (see **Equations 1.1 thru 1.3**), efficient water management in the MEA should avoid both flooding and membrane/ionomer dehydration at the electrodes. As evidenced in **Figure 2.9**, a symmetric RH of 100% at both the anode and cathode yielded the highest current density. On the cathode side, an elevated cathode RH of 125% is more than enough to balance water consumption and supply at the cathode (and possibly throughout the MEA), with higher RHs as high as 200% being detrimental to performance, possibly due to excess water in or flooding of the cathode electrode. The 125% cathode RH appears to be better than the 100% case at moderate cell voltages, after which the 100% case becomes more advantageous. It is also clear that any RH below 100% at the anode is very detrimental, with operation even at the slightly lower RH of 95% leading to drastically poorer performance. Thus, a minimum RH of 100% is required to maintain adequate performance in both the anode and cathode chambers. With CO_2R systems having higher overpotential requirements than water electrolysis in general, this makes the 100% symmetric RH case at both anode and cathode more advantageous to operate with and was thus used in subsequent tests throughout this dissertation.

2.4.2.5 The effect of system temperature

The literature has shown that system temperature is a key factor in determining CO_2R electrolyzer performance.[118–120] Thus, the effects of system temperature were explored for a CO_2R MEA operated as an Exchange-MEA and the chosen temperature range was between 50°C and 70°C, above which severe polymer denaturing in the membrane/ionomer phases could occur.[111,121]

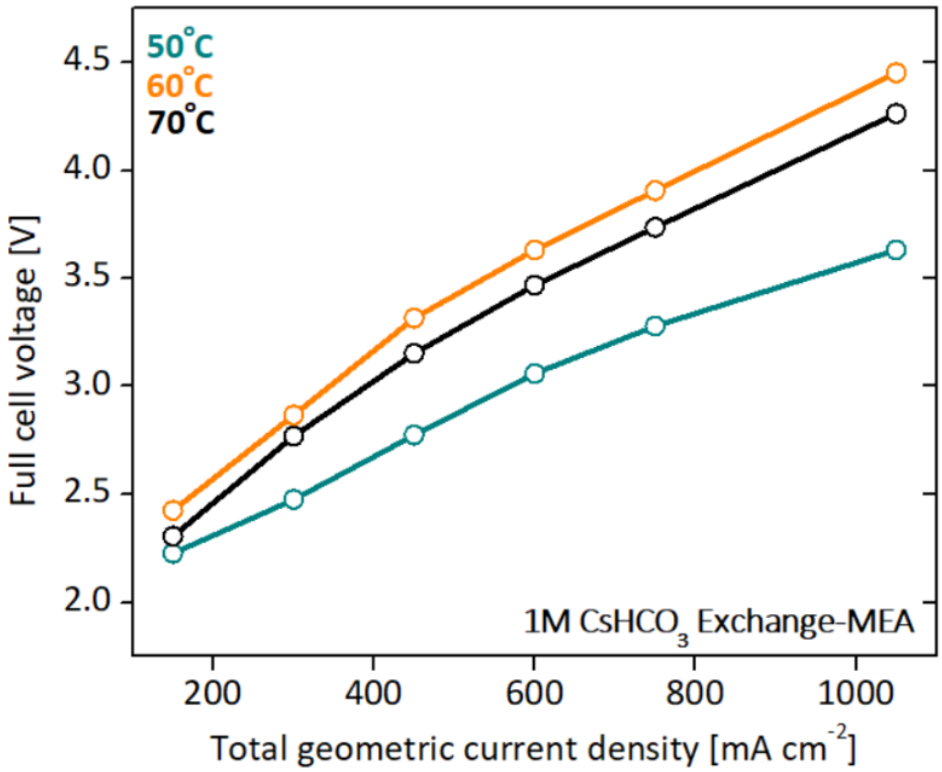

Figure 2.10. CO_2R polarization curves for various system temperatures: 50, 60, and 70°C. Test conditions: 100% RH at both electrodes, CO_2R at the cathode (flowing gas: CO_2 at 200 ml min^{-1}), OER at the anode (recirculating 1M $CsHCO_3$), Ag/C weight fraction of 20%, I:Cat (ionomer-to-catalyst) ratio was 3, and Ag-only loading was 0.1 mg_{Ag} cm^{-2} for the cathode, the Ir I:Cat (ionomer-to-catalyst) ratio was ~0.1, and Ir-only loading was ~1 mg_{Ir} cm^{-2} for the anode. A Versogen® (W7) W7 30µm AEM and ionomer fabricated in GDE-mode was used.

As shown in **Figure 2.10**, the lowest system temperature of 50°C surprisingly outperformed the higher temperature systems, 60°C and 70°C. This signifies an apparent tradeoff between certain physical phenomena occurring locally in the cathode catalyst layer when the cell temperature is increased: differences in reactant and water concentration (since humidity and total pressure are fixed), faster transport processes, and faster kinetics as well as potential microscopic ionomer/membrane dehydration/degradation at higher temperatures.[46,111,121] Thus, the 50°C Exchange-MEA configuration was used in the subsequent studies presented in Chapters 3 and 4.

2.5 Electrochemical Measurements

The CO_2R electrolyzer system described above was used to investigate the effects of materials choice and operating condition on CO_2 reduction in an MEA. An EC-Lab® software was used to measure the open circuit voltage (OCV) of the system, followed by measurements of the cell current as a function of time for a fixed cell potential, chronoamperometry (CA), and measurements of cell voltage as a function of time for a fixed current, chronopotentiometry (CP). Electrochemical-impedance spectroscopy (EIS) was also performed to determine cell resistance.

After cell assembly and system set up, the MEA is connected to a Bio-Logic® potentiostat via the cell current collectors: working electrode leads were connected to the cathode, while counter and reference electrode leads were connected to the anode. After steady feed and liquid flows (*i.e.,* CO_2, H_2, Ar, water, exchange solution *etc.*) are established, the MEA is allowed to equilibrate thermally and electrochemically. OCV measurements were made for at least 60 min before any electrochemical perturbations were induced. After these and other baseline tests were completed, the CA (constant-voltage hold) or CP (constant-current hold) were performed for at least 30 min each, together with product analysis, to generate a polarization curve. CP holds have the advantage of allowing for analysis of product selectivity and activity at fixed current/ion fluxes. For each voltage or current density step, the corresponding current density or full-cell voltage is averaged over the last 15 min. At least two gas or liquid samples were taken at both the anode and cathode and the measured product concentrations, the corresponding current densities, and the outlet flow rates are used to determine the product selectivities for each voltage or current density step. CO_2 crossover measurements are also conducted at the anode. Multiple MEA experiments and repeated electrochemical tests were typically performed to determine reproducibility and error bars are used to show the spread in these measurements.

2.5.1 Impedance measurements

Electrochemical-impedance spectroscopy (EIS) was used to measure the ohmic resistance of the MEA cell. Low-frequency EIS measurements (on the order of 1 Hz) give insight into ohmic/ionic effects occurring at the interfaces in the membrane/catalyst-layer region, while higher frequency EIS measurements (up to 1000 kHz) provide ohmic/ionic conductivity information pertaining to bulk media like membranes. After thermal uniformity and complete hydration of an MEA is achieved and a consistent OCV measurement is established, EIS was used to measure the high-frequency resistance (HFR) of the cell. This was typically under 0.2 Ω or 1 Ω cm^2 for all experiments. In addition, EIS was performed at each voltage or current density step to observe cell resistance trends across the polarization curve range and to construct corresponding *iR*-corrected curves. The *iR*-corrected graphs indicate current-voltage responses when the cell resistance has been accounted for, giving a clearer picture of the electrode activity-specific polarization performance. Deriving the EIS HFR resistance data involves performing a ZFit® on the measured resistance-impedance data (*i.e.,* Nyquist plot), as shown for a sample MEA in **Figure 2.11**, and choosing the estimated equivalent circuits for a given system. For example, a serial resistance element R1 symbolizes an electrolytic-type resistance between the anode and cathode, which is the membrane. A resistance element in parallel with a capacitive element (*i.e.,* R2) symbolizes a charge transfer resistance that involves electron transfer to the catalyst and ion transfer to the ionomer. The capacitance-like element (*i.e.,* Q2) denotes a constant phase element or imperfect

capacitor, which is a measure of double layer capacitance. For planar systems, which have much more defined electrode surfaces/interfaces, an ideal capacitor element (*e.g.,* C2) would be used for better accuracy. Thus, the secondary parallel circuit with the resistive and capacitive elements in parallel symbolizes the catalyst layer, which has both ionomer and electrocatalyst elements. Once a physically representative equivalent circuit for the MEA system has been chosen, an empirical fit of the model to the data in a Nyquist-plot is performed to determine the equivalent circuit values of R1, R2, and Q2.

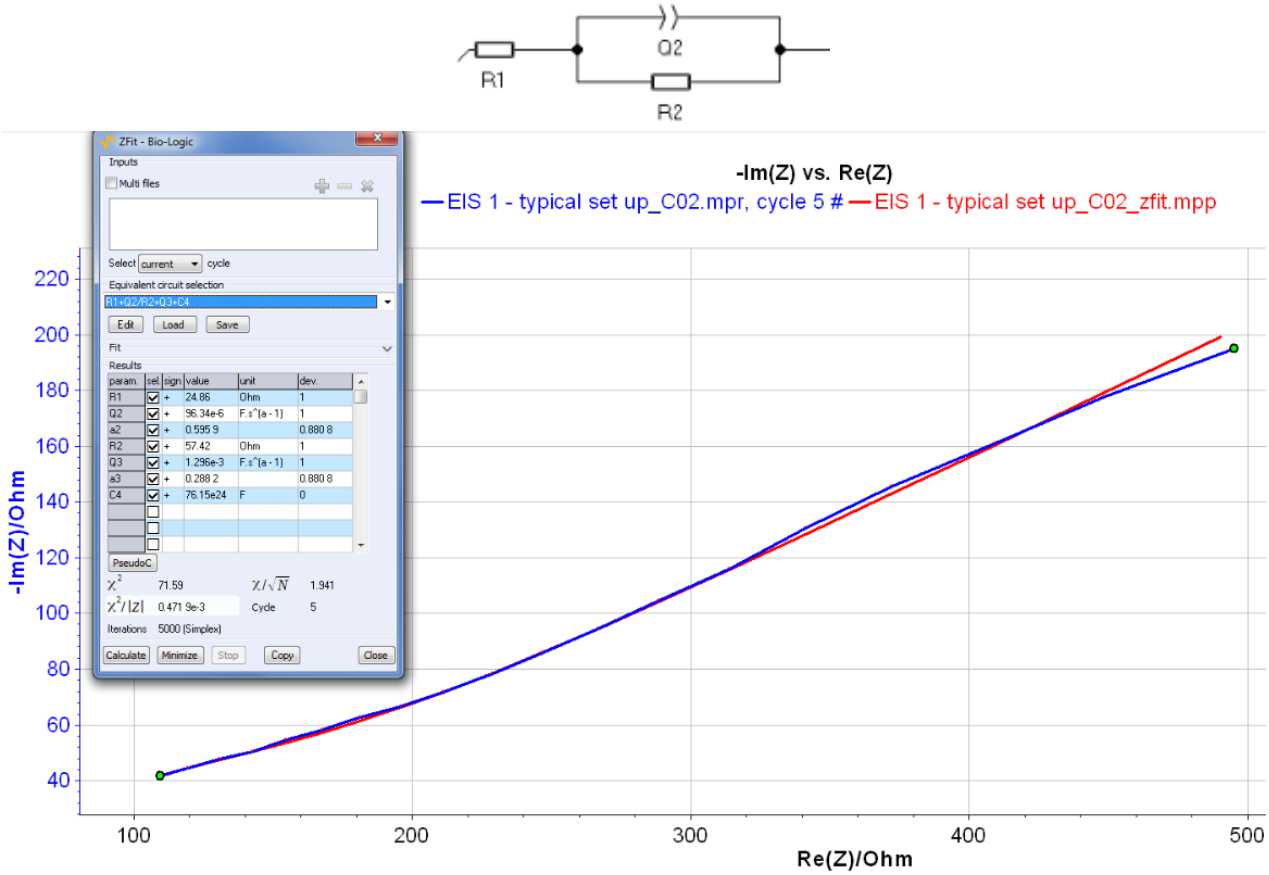

Figure 2.11. Depiction of a Nyquist plot, ZFit® parameters, and representative equivalent circuit for an early MEA prototype. A high-frequency resistance electrochemical impedance spectroscopy (EIS HFR) procedure was performed to generate the above plot and derive an estimate of the cell resistance via empirical fitting. Typical values of R1 were under 0.2 Ω for all reported experiments.

Figure 2.12 shows the EIS HFR information derived from the AEM membrane and ionomer benchmarking studies presented earlier in this chapter (see **Figure 2.2**). Interestingly, the resistance of Sustainion and Versogen (W7) cell systems were comparable with that of Nafion for most of the potential window studied, especially for full-cell voltages that ranged from 0.5 to 1.1V. This indicates that the different polymer chemistries in these three systems are not hugely crucial determinants of the ohmic properties of these systems and that the catalyst-layer microenvironment created by the operating conditions (*i.e.,* temperature, water content) may instead be more important. The highest ohmic resistance was for the Georgia Tech (GT) membrane and ionomer system, which would also explain its comparatively poor catalyst activity shown in **Figure 2.2**.

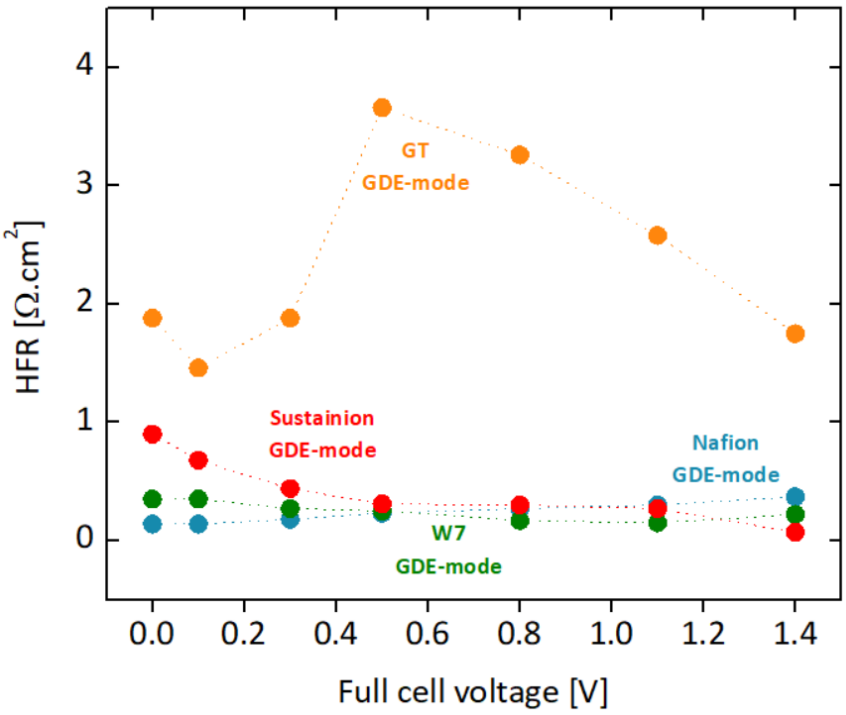

Figure 2.12. High-frequency resistance electrochemical-impedance spectroscopy (EIS HFR) for various AEM ionomer and membrane systems. A CEM/Nafion system was also included for reference. Test conditions are the same as those in **Figure 2.2.** Test conditions: 80°C system temperature, Full-MEA configuration, 100% RH at both electrodes, HER at the cathode (flowing gas: Ar at 200 ml min^{-1}), HOR at the anode (flowing gas: H_2 at 200 ml min^{-1}), Pt/C weight fraction of around 46%, I:C (ionomer-to-carbon) ratio was 0.6, and Pt-only loading was 0.3 mg_{Pt} cm^{-2} for both anode and cathode. The following systems are depicted: (1) Nafion®: Nafion 212 CEM and Nafion ionomer, (2) Versogen® (W7): W7 30μm AEM and ionomer, GDE-mode, (3) Sustainion® system: Sustainion AEM and Sustainion ionomer, GDE-mode, and (4) Georgia Tech® (GT): GT 72-10 membrane and GT 72-5 ionomer, GDE-mode.

2.5.2 Other important considerations

Once any desired electrochemical measurements are concluded, all equipment, especially heating elements and electrical devices, are shut off and sufficient time is allowed for cool down of hot objects before handling and disassembly. Cell electrolyzer components are thoroughly cleaned, dried, and stored in a cool, dry area ahead of next use and the used MEA components (*i.e.,* anode PTL, cathode GDL, and hydrated membrane) are stored in appropriately labelled sample bags for future reference or post-experimental characterization. Before, during, and after operation, safety precautions must be observed: heating and electrical equipment and lines should be handled with care and proper corrosive chemical handling and spill cleanup awareness should be ensured. Using alligator clips for electrical connections is highly discouraged as they can corrode and cause poor contact overtime: secure banana plugs should be used instead to ensure good electrical contact. In addition, hydrogen gas is fed into the anode of the electrolyzer when performing HOR: metal tubing should always be used for lines containing hydrogen and, as much as possible, these should be kept away from electrical connections and cables, as well as other potential fire sources such as hot surfaces.

3 Tuning Catalyst-Ionomer Coverage and Interactions towards Selective and High Current Density CO_2 Reduction

† Portions of this chapter were previously published as "**O. Romiluyi**, N. Danilovic, A. T. Bell, and A. Z. Weber, "Membrane-electrode assembly design parameters for optimal CO_2 reduction", Electrochemical Science Advances, ISSN: 2698-5977, 2698-5977; DOI: 10.1002/elsa.202100186 (2022)" and are adapted with permission from all co-authors.

Commercial-scale generation of carbon-containing chemicals and fuels by means of electrochemical CO_2 reduction (CO_2R) requires electrolyzers operating at high current densities and product selectivities. Membrane-electrode assemblies (MEAs) have been shown to be suitable for this purpose. In such devices, the cathode catalyst layer controls both the rate of CO_2R and the distribution of products. In this study, we investigate how the ionomer-to-catalyst ratio (I:Cat), catalyst loading, and catalyst-layer thickness influence the performance of a cathode catalyst layer containing Ag nanoparticles supported on carbon. We explore how these parameters affect the cell performance and establish the role of the exchange solution (water vs. $CsHCO_3$) behind the anode catalyst layer in cell performance. We show that a high total current density is best achieved using an I:Cat ratio of 3 at a Ag loading of 0.01–0.1 mg_{Ag} cm^{-2} and with a 1.0 M solution of $CsHCO_3$ circulated behind the anode catalyst layer. For these conditions, the optimal CO partial current density depends on the voltage applied to the MEA. The work also reveals that the performance of the cathode catalyst layer is limited by a combination of the electrochemically active surface area and the degree to which mass transfer of CO_2 to the surface of the Ag nanoparticles and the transport of OH^- anions away from it limit the overall catalyst activity. Hydration of the ionomer in the cathode catalyst layer is found not to be an issue when using an exchange solution. The insights gained allowed for a Ag CO_2R MEA that operates between 200 mA cm^{-2} and 1 A cm^{-2} with CO faradaic efficiencies of 78–91%, and the findings and understanding gained herein should be applicable to a broad range of CO_2R MEA-based devices.

3.1 Introduction

Chapter 1 presented the case for the CO_2R MEA, outlined the complexity of the cathode catalyst-layer microenvironment, and explained why it is of scientific importance, while Chapter 2 delved into the engineering and experimental methods employed to obtain a reliable, reproducible, and versatile CO_2R MEA system. This current chapter combines the aforementioned elements to systematically investigate key cathode catalyst-layer design parameters (*i.e.,* the ionomer-to-catalyst ratio (I:Cat), the catalyst loading, and the catalyst-layer thickness) and operating conditions (*i.e.,* the anode exchange solution concentration as well as the choice of MEA cell design and degree of hydration), extract physical insights from the trends and features observed, and develop a high performance (*i.e.,* selective and high current density) Ag-based CO_2R MEA. The findings described within this chapter should be applicable to a broad range of CO_2R MEA-based devices and it outlines a pathway towards high-throughput commercial applications. Key to achieving industrial scale CO_2R is the development and fundamental understanding of a cell that can efficiently and selectively produce value-added CO_2R products. Specifically, a CO_2R

electrolyzer must operate at current densities in excess of 200 mA cm^{-2} under moderate applied cell potentials (< 4 V) in order to minimize capital costs and achieve high energy efficiency.[122] Prior studies have shown that these targets can be best achieved with a membrane-electrode-assembly (MEA) (*i.e.,* a zero-gap cell) because of its efficiency advantages stemming from low ohmic resistance and improved mass transport compared to traditional planar electrode and aqueous gas-diffusion-electrode (GDE) cells with aqueous electrolyte.[45,46,50–56]

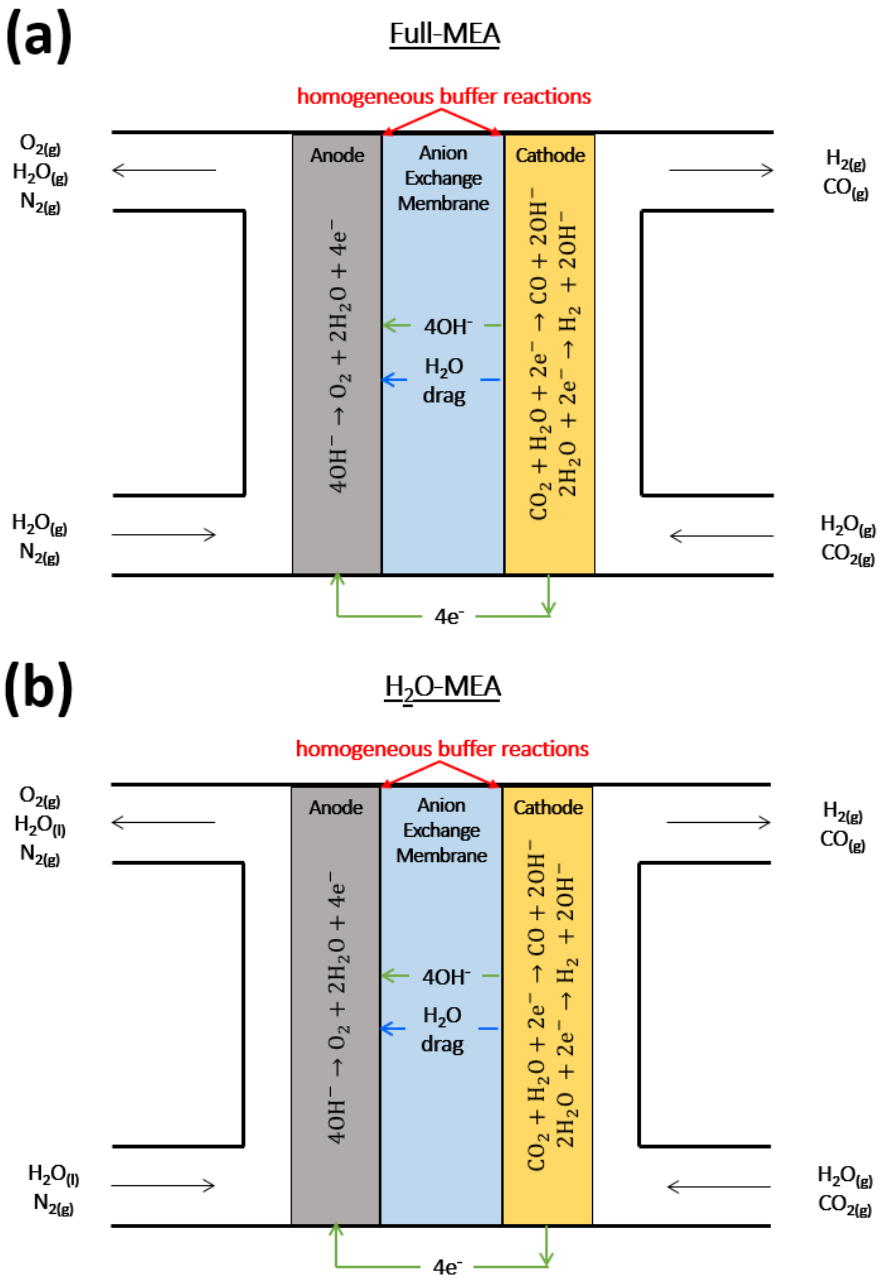

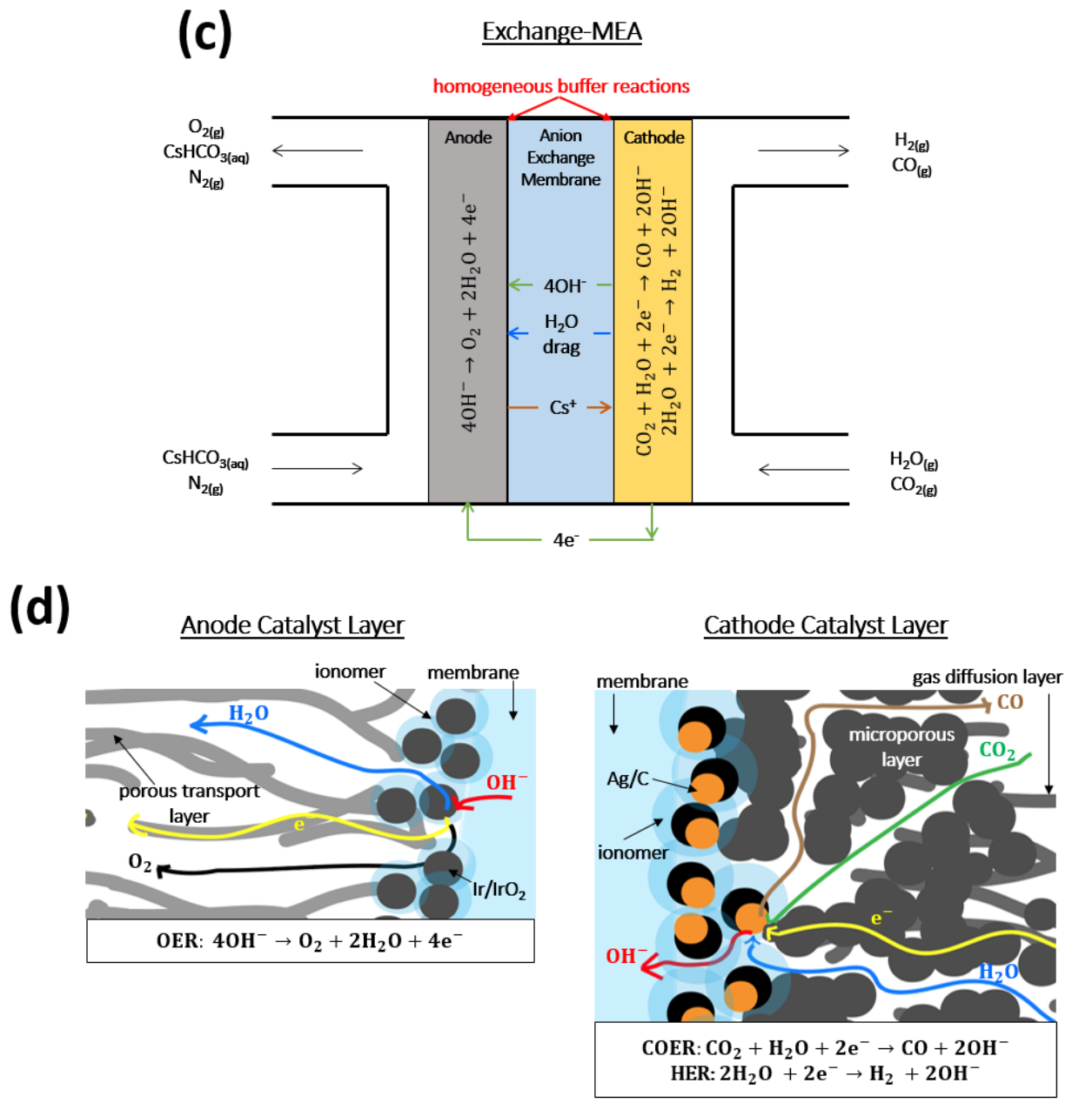

Figure 3.1. Schematics of the ionomer-catalyst-membrane microenvironment in a Ag cathode, Ir anode CO_2 reduction MEA system: (a) Full-MEA schematic (b) H_2O-MEA schematic (c) Exchange-MEA schematic (d) Blow ups of the cathode and anode catalyst layers. The schematics provide a system-wide overview of the MEA device for Ag CO_2R with associated reactants and products. Homogenous buffer reactions, electroosmotic water drag, and migration of exchange solution cations occur in the device.

Figure 3.1 illustrates the structure of an MEA for the electrochemical reduction of CO_2 to CO and H_2. The cathode is composed of a catalyst layer (CL) deposited onto a microporous layer (MPL) residing on top of a gas-diffusion layer (GDL), while the anode is composed of a CL deposited onto a porous-transport layer (PTL). The cathode CL consists of carbon-supported silver (Ag)

nanoparticles, while the anode CL consists of unsupported iridium/iridium oxide (Ir/IrO_2) nanoparticles. An anion-conducting polymer is used between the electrodes because prior findings have demonstrated that lower hydrogen-evolution-reaction (HER) rates correlate with the lower proton availability that is observed in high pH environments for Ag cathodes; these conditions enhance carbon monoxide evolution.[34,40–44] Specifically, the anion-exchange membrane (AEM) enables the transport of hydroxide (OH^-) anions, produced at the cathode via CO_2R and HER (see **Equations 3.1 and 3.2**), to the anode where they are consumed via the oxygen-evolution reaction (OER) (see **Equation 3.3**). For similar reasons, the catalyst particles at both electrodes are covered with a solid-state anion-conducting ionomer. We note that homogeneous buffer reactions occur in the hydrated ionomer and membrane (see **Equations 3.4 and 3.5**), which lead to the formation of HCO_3^- and CO_3^{2-} that are transported across the membrane, essentially pumping CO_2 from the cathode to the anode and representing a major loss in the utilization of CO_2.[46]

Three MEA designs were explored in this study: one in which a humidified stream of CO_2 was supplied to the cathode and a humidified stream of N_2 was supplied to the anode (*i.e.,* Full-MEA), the second design consisting of a humidified stream of CO_2 supplied to the cathode and liquid H_2O recirculating behind the anode (*i.e.,* H_2O-MEA), and a third design that is similar to the second except that an ionic solution ($CsHCO_3$) was recirculated behind the anode (*i.e.,* Exchange-MEA). $CsHCO_3$ was chosen as the ion solution because it can supply hydrated Cs^+ cations to the cathode CL, which have been shown to enhance the rate of CO_2R over Ag relative to other alkali metal cations.[96] Bicarbonate (HCO_3^-) was chosen as the anion, rather than hydroxide, in order to avoid significant loss of CO_2 due to the aforementioned CO_2 pumping phenomenon.[46] The half and buffer reactions occurring at each side of this device are

$$\text{Cathode} - \text{COER: } CO_2 + H_2O + 2e^- \rightarrow CO + 2OH^- \ (U^\circ = -0.11 \text{ V vs. SHE}) \quad (3.6)$$

$$\text{Cathode} - \text{HER: } 2H_2O + 2e^- \rightarrow H_2 + 2OH^- \ (U^\circ = -0.828 \text{ V vs. SHE}) \quad (3.7)$$

$$\text{Anode} - \text{OER: } 4OH^- \rightarrow O_2 + 2H_2O + 4e^- \ (U^\circ = 0.401 \text{ V vs. SHE}) \quad (3.8)$$

$$CO_2 + OH^- \leftrightarrow HCO_3^- \ (pK_a = 6.37) \quad (3.9)$$

$$HCO_3^- + OH^- \leftrightarrow CO_3^{2-} + H_2O \ (pK_a = 10.3) \quad (3.10)$$

The total current density (TCD) and product distribution obtained with an MEA used for CO_2R depend on a number of interrelated factors, such as membrane and ionomer hydration, cell temperature, reactant partial pressure, *etc*. Prior research has shown that the distribution of CO_2R products is a strong function of both the catalyst composition and its surrounding microenvironment.[34,45,46,48,123] In the case of an MEA, the ionomer-to-catalyst (I:Cat) ratio, the catalyst loading, and the thickness of the CL also impact cell performance.[124,125] However, the effect of all these design factors on CO_2R are not yet fully understood. In this present study, we conduct a systematic investigation of the effect of these parameters on the activity and product distribution of a CO_2R MEA using a Ag cathode. Ag is of particular interest as an electrocatalyst because it produces only H_2 and CO, a product mixture that can be readily converted to a spectrum of hydrocarbons via Fischer-Tropsch synthesis.[25,38] Tandem systems that convert CO_2 to CO and subsequently convert CO to C_{2+} products using Ag-Cu electrodes[126,127] can also benefit from this study in terms of informing their system designs to maximize CO production.[128]

3.2 Experimental Methods

3.2.1 Catalyst inks and electrode substrates

The Ag cathode ink comprised of Ag/C particles (*i.e.,* 20% Ag on Vulcan XC-72 carbon support, Premetek®), Sustainion® ionomer (5% in ethanol, Dioxide Materials®), water (Milli-Q®, 18 mΩ), and n-propanol (Sigma-Aldrich®). The Ir anode catalyst ink comprised of IrO_2 nanoparticles (Tanaka®, SA=100), Sustainion® ionomer (at an optimal ionomer content of 11.6 wt.-%)[129], water, n-propanol, and ethanol (Sigma-Aldrich®). Detailed ink recipes are provided in **Table S3.1**. The inks were sonicated ultrasonically (Symphony® Sonicator) for 30 min.

The cathode electrode substrate consisted of a microporous layer (MPL) covering a gas-diffusion layer (GDL) made of carbon fibers and 5 wt.-% PTFE and with a total composite porosity of 0.52 (Sigracet® 39BC). The anode electrode substrate was a proprietary mesoporous titanium (Ti) porous transport layer (PTL) provided by NEL Hydrogen®. Before deposition, both electrode substrates were cleaned with ultra-pure nitric acid in order to remove electrochemically-active trace impurities.[104] Catalyst inks were then spray-coated onto the cathode and anode substrates using an ultrasonic spray coater (Sono-Tek® Exactacoat). For each electrode, the spray coating time was adjusted to achieve a desired loading. After deposition, each electrode was pretreated in 1 M KOH for at least 24 h to facilitate anion exchange in the ionomer.

3.2.2 Membrane and cell assembly

A 50 μm-thick hydrated Sustainion® X37-50 Grade RT membrane (Dioxide Materials®) was pretreated in 1 M KOH for at least 24 h. The membrane was sandwiched between the two prepared electrodes and the resulting MEA was assembled into a 5 cm^2 commercial cell (Fuel Cell Technologies®). A torque wrench was used to tighten each cell bolt to 40 in-lb and 10-mil (*i.e.,* 0.01") thick PTFE gaskets (Fuel Cell Technologies®) were used on each gas channel to ensure reproducible and uniform compression across the MEA and to prevent leakages. The cell was then connected to a potentiostat with a 10A booster (Bio-Logic®).

The CO_2 entering the cathode compartment was humidified by bubbling it through a bottle of deionized water (Milli-Q®, 18 mΩ) maintained at 50°C via a hot-water bath. A flow of deionized water (Milli-Q®, 18 mΩ) or cesium bicarbonate ($CsHCO_3$) (Sigma-Aldrich®) at 50°C was fed behind the anode as the MEA exchange solution . The MEA cell was heated and operated at 50°C. The cathode feed flow rate was set to or above 200 mL min^{-1} of humidified CO_2 (measured using a mass-flow controller (Alicat Scientific®)) in order to avoid reactant supply limitations and mass-transfer effects stemming from large fractional conversions. The exchange solution fed behind the anode was rapidly circulated (24.6 mL min^{-1}) using a peristaltic pump (Masterflex®) so that concentrations in the gas channels and porous electrodes remained uniform and gradients were minimized. Flow rates of the cathode and anode outlet gases were verified using a mass-flow meter (MFM) (Alicat Scientific®) to ensure no leakage across the entire system and for faradaic-efficiency (FE) calculation purposes.

3.2.3 Electrochemical testing

The cell was first monitored at open circuit for 30 to 60 min to ensure thermal uniformity and complete hydration of the cell membrane and the ionomer in the CLs. After equilibration, electrochemical-impedance spectroscopy (EIS) was used to measure the high-frequency resistance (HFR, 1 Hz to 1000 kHz) of the cell (which was consistently under 0.2 Ω or 1 Ω cm^2 for all experiments. After these baseline tests were completed, chronoamperometry (CA, constant-voltage hold) was performed together with in-line gas-chromatography (GC) analysis (SRI Instruments®) using both a flame-ionization detector and a thermal-conductivity detector. A polarization curve was obtained, with each voltage step of 0.4 V being held for at least 30 min. For each voltage step, the reported current density was averaged over the last 15 min. Two GC samples were taken per electrode: the measured CO and H_2 product concentrations, the corresponding current density, and the outlet flow rate were used to determine the product FE at each voltage step. Error bars denote multiple separate measurements with different MEAs.

3.3 Results & Discussion

3.3.1 System design choice

Exploratory experiments conducted at the outset of this work established that in order to ensure adequate hydration of the ionomer and the membrane, the MEA should be operated as either an H_2O-MEA or an Exchange-MEA. As seen in **Figure S3.1**, operation of the MEA as a Full-MEA increases the cell voltage required to achieve a given current density and this problem becomes more severe at higher current densities, with poorer stability (*i.e.,* larger hysteresis between voltage sweeps) being demonstrated in the Full-MEA compared to the H_2O-MEA. This pattern is believed to be a consequence of the decrease in the ionomer and membrane conductivity as the current density rises, thus leading to dehydration of the polymeric components.[46] Raising the cell temperature of the H_2O-MEA from 25 to 50°C resulted in superior overall performance due to the higher water content and faster kinetics and mass transport at the elevated temperature (see **Figure S3.2**). Thus, an H_2O-MEA operated at 50°C was used as the baseline for the following studies.

3.3.2 The effect of cathodic I:Cat ratio

The catalyst loading at both the anode and cathode CLs was fixed at 1 $mg_{catalyst}$ cm^{-2}, while the ionomer-to-catalyst (I:Cat) ratio for the cathode CL was varied from 1 to 5 on a weight basis. **Table S3.2** shows how the I:Cat ratio is related to the more often-used ionomer-to-carbon (I:C) ratio presented in the fuel-cell literature, but that metric is less relevant here since carbon is not always necessarily present in the CL.

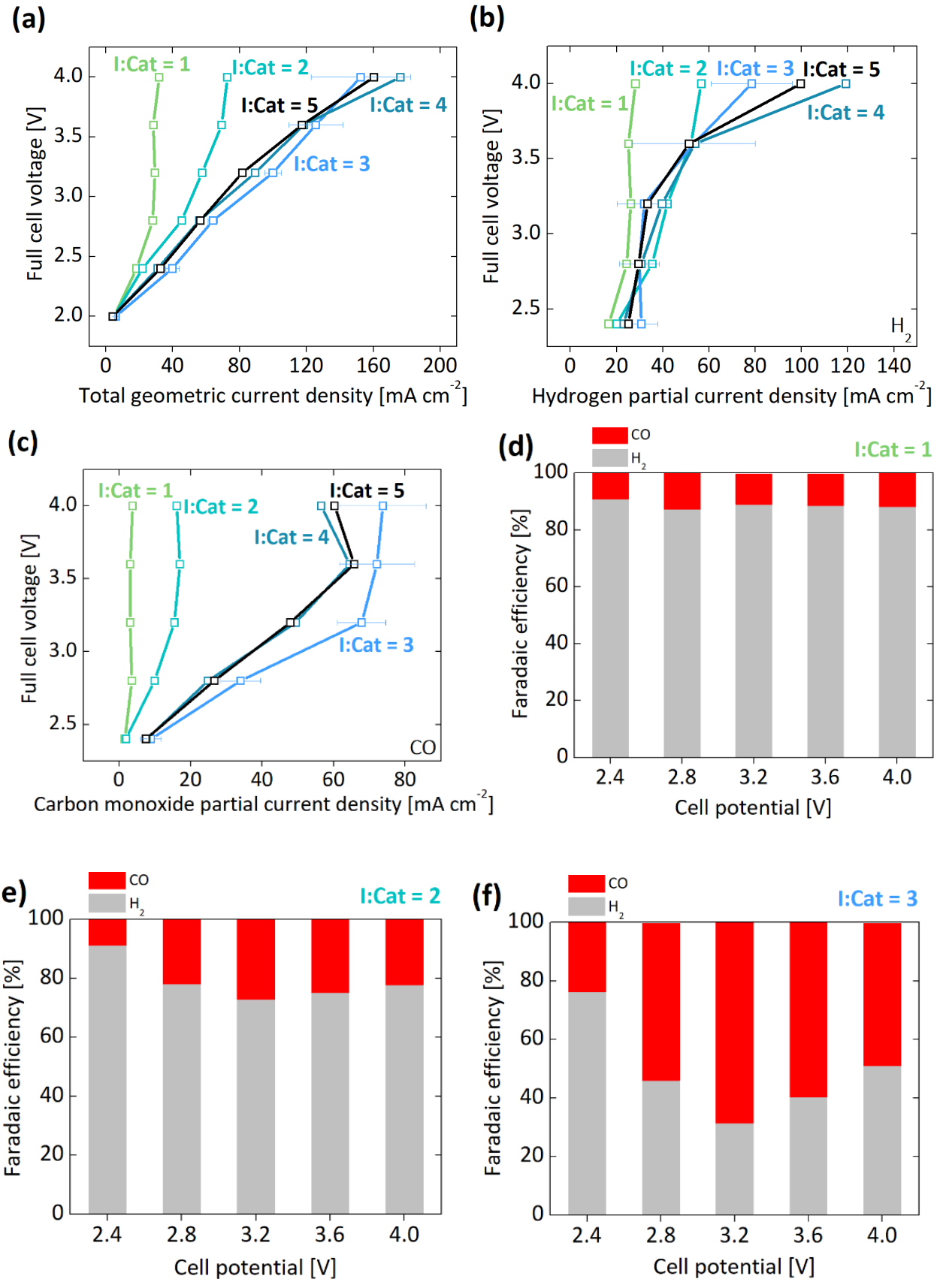
(a)
I:Cat = 1
I:Cat = 2
I:Cat = 5
I:Cat = 4
I:Cat = 3
Full cell voltage [V]
Total geometric current density [mA cm-2]
(b)
I:Cat = 2
I:Cat = 3
I:Cat = 5
I:Cat = 1
I:Cat = 4
H2
Full cell voltage [V]
Hydrogen partial current density [mA cm-2]
(c)
I:Cat = 1
I:Cat = 2
I:Cat = 5
I:Cat = 4
I:Cat = 3
CO
Full cell voltage [V]
Carbon monoxide partial current density [mA cm-2]
(d)
CO
H2
I:Cat = 1
Faradaic efficiency [%]
Cell potential [V]
(e)
CO
H2
I:Cat = 2
Faradaic efficiency [%]
Cell potential [V]
(f)
CO
H2
I:Cat = 3
Faradaic efficiency [%]
Cell potential [V]

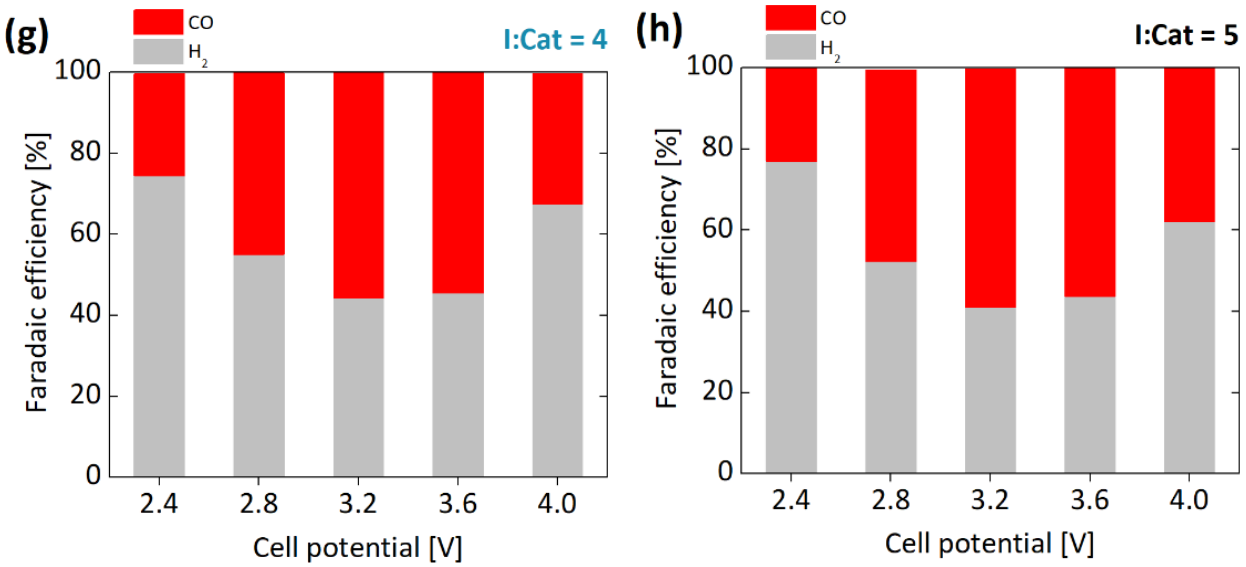

Figure 3.2. Polarization (a), hydrogen partial current density (b), and carbon monoxide partial current density (c) behavior as a function of cathodic ionomer-to-catalyst ratio. Faradaic efficiency as a function of potential for the different ratios: I:Cat = 1 (d), I:Cat = 2 (e), I:Cat = 3 (f), I:Cat = 4 (g), I:Cat = 5 (h) in a Ag cathode, Ir anode MEA. Test conditions: 50°C, atmospheric pressure, 200 mL min^{-1} fully humidified CO_2 feed at the cathode, liquid water behind the anode.

Polarization curves for different cathode CL I:Cat ratios presented in **Figure 3.2(a)** demonstrate that, for a given cell potential, the TCD increases as the I:Cat increases from 1 to 3, with I:Cat ratios from 3 to 5 exhibiting nearly identical behavior. **Figure 3.2(b) and (c)** display how the I:Cat ratio impacts the partial current densities for H_2 and CO, respectively. As the I:Cat increases from 1 to 3, the partial current density for H_2 increases monotonically, whereas for CO, the partial current density increases up to an I:Cat ratio of 3 and then decreases for higher I:Cat ratios, especially once the cell potential increases above 3.5 V. The observed trends in the partial current densities of H_2 and CO with I:Cat ratio and cell potential lead to an increase in the FE for CO and a decrease in the FE for H_2, as seen in **Figure 3.2(d) thru (h)**. For I:Cat = 1, the FE for both products is relatively insensitive to the cell potential, whereas for the other I:Cat ratios, the CO FE reaches a pronounced maximum at 3.2 V, especially for I:Cat = 3. Furthermore, the CO partial current levels off with increasing cell potential for I:Cat = 2 and 3, whereas the H_2 partial current rises monotonically with increasing I:Cat. A CO FE (68%) and partial current (74 mA cm^{-2}) are observed for I:Cat = 3 at 3.2 V. Analysis of product selectivity at constant current (*i.e.,* fixed OH^- flux) as given in **Figure S3.5(a) thru (c)** demonstrates that I:Cat = 3 still yields both a high CO partial current and FE and these characteristics are lower for the higher I:Cat = 4 and 5 systems.

Figure 3.3 illustrates our conceptual picture of the cathode CL structure. The electrochemically-active surface area (ECSA) refers to the surface area of Ag covered by ionomer for which there are accessible ionic and electronic pathways to the membrane and GDL, respectively. For CO_2R to occur on the Ag/C catalyst particles, it is essential that percolation pathways exist for electron flow from the cathode GDL to the Ag/C particle, for OH^- transport from the ionomer covering the Ag nanoparticles to the membrane, and for gas transport from the flow channel to the catalytically active sites. The pathway for electron flow is provided by good contact of the carbon particles

supporting the Ag nanoparticles with the carbon in the MPL and GDL. The pathway for OH^- anions, produced at the cathode, is via continuous ionomer tendrils connecting the surface of the Ag particles to the membrane. If the void space in the cathode CL is partially filled with liquid electrolyte (originating from the anode exchange solution), then this medium can also act as a pathway for OH^- transport, as occurs in the wetted pores of an aqueous GDE.[56] The existence of parallel pathways for ion transport from the catalyst surface to the membrane implies that the microenvironment in the CL and near the catalyst surface can be heterogeneous. Finally, the transport of CO_2 occurs from the flow channel on the cathode side of the MEA, through the pores in the GDL and MPL, and to the Ag/C catalyst particles. To reach the Ag surface, gaseous CO_2 must dissolve into a thin layer of ionomer or liquid electrolyte covering the Ag catalyst particles.

The cartoons in **Figure 3.3** illustrate how the structure of the cathode CL changes for cases of low, moderate, and high I:Cat ratio. For each case, the right side illustrates the specific coverage of the Ag/C nanoparticle and the supporting ionomer, whereas the left side illustrates the electronic, ionic, and pore-space connectivity throughout the CL. As the I:Cat ratio increases, the fraction of individual Ag/C particles covered with ionomer increases. For a H_2O-MEA, increasing ionomer coverage of the Ag particles increases its ECSA since the ionomer provides access for H_2O and CO_2 to the Ag surface and a path for the movement of OH^- anions from the Ag surface.

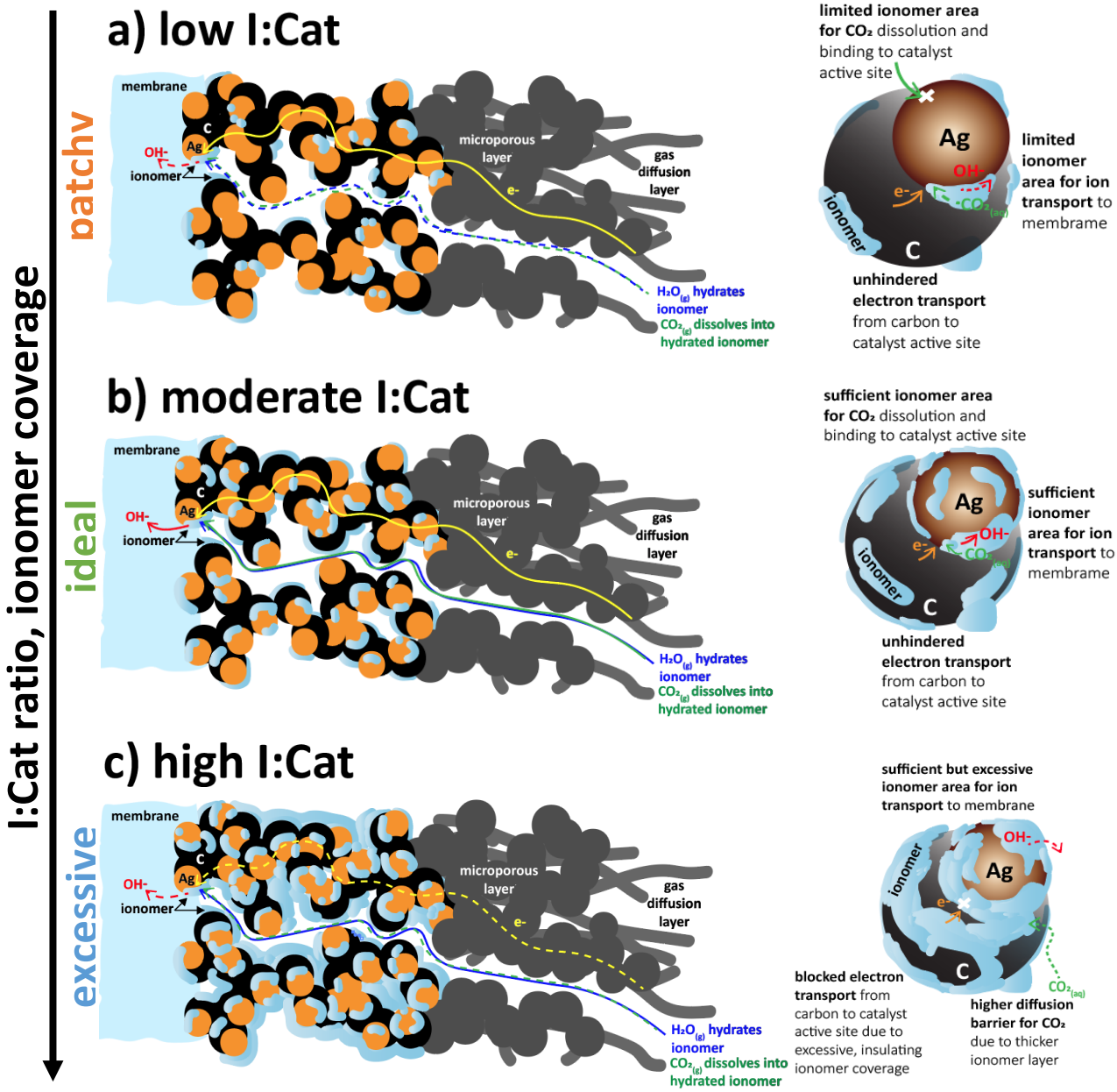

Figure 3.3. Schematic of catalyst-layer microenvironment and ionomer-catalyst distribution on a catalyst and support nanostructure based on I:Cat ratio and ionomer content/coverage. The patchy ionomer distribution depicts low I:Cat ≤ 2, the excessive distribution depicts high I:Cat ≥ 4, and the idealized distribution refers to the moderate I:Cat = 3. Electron, ion, and gaseous pathways and tradeoffs are also shown.

It should be noted that sufficient ionomer must be present so that a bridge develops between the individual Ag/C particles and the membrane since this bridge is essential for the flow of OH^- anions from the CL to the membrane. If these ionomer tendrils are insufficient in number, as in the case of low I:Cat ratios, then the existing ones must carry all of the ion current, inducing local mass-transport limitations of OH^-, and consequently low ion conductivity.[130] For the low number of active sites, the high current density in the tendrils coupled with their low conductivity can lead to ohmic heating that has the potential to dehydrate the CL. This loss due to ohmic heating is offset by the water flux through the membrane and into the ionomer tendril provided by the liquid H_2O present behind the anode. **Figure S3.4** depicts an ionomer dehydration model of how the cathode CL water activity changes with current density and I:Cat ratio. The results of the model clearly show that extensive ionomer dry out (*i.e.,* water activity falling well below 1.0) is not at all expected to occur in the cathode CL, especially in portions closest to the membrane (*i.e.,* the active thickness of the CL) at the current densities measured due to the existence of the water from the exchange solution. We note that low coverage of the Ag nanoparticles by ionomer reduces the ECSA, an issue that is particularly important in the case when the MEA operates with only water behind the anode CL.

The very steep rise in the cell voltage with TCD seen in **Figure 3.2(a)** for I:Cat ratios of 1 and 2 depicts limiting-current behavior that is attributed to both low ECSA and mass-transport limitations within the cathode CL. As noted above, patchy coverage of the Ag particles by ionomer at low I:Cat ratios reduces the active area for catalysis. This means that the overpotential applied to these particles rises sharper than would be anticipated, resulting in severe local mass-transfer limitations of CO_2, which accesses the surface of the Ag particles primarily via transport through the ionomer tendrils. Moreover, the pH in the portion of the tendrils close to the Ag/C nanoparticles increases due to the higher local reaction rate, causing a decrease in the local concentration of CO_2 due to its consumption by buffering reactions, as described above (see **Equations 3.11 and 3.12**).

Upon increasing the I:Cat ratio to 3, more of the Ag/C particles become covered by ionomer, which in turn increases the number of ionomer tendrils available to carry the ionic current. These changes result in an overall higher rate of CO_2R, as evidenced by the increased CO partial currents and FEs shown in **Figure 3.2(c) thru (f)**. The proposed interpretation of the effects of I:Cat ratio is in agreement with previous studies of local conditions in CO_2R systems.[13134,40–44] For I:Cat ratio = 3 to 5, the current carrying capacity of the ionomer tendrils no longer limits the TCD, as evidenced by the polarization curves becoming more ohmic in character (*i.e.,* exhibiting a linear relationship between current and potential). However, if the I:Cat ratio is raised above 5, the extra ionomer decreases the CL porosity (see **Figure S3.5**) and can interfere with electron conduction from the cathode MPL and GDL to the Ag/C particles and with the passage of CO_2 to the Ag/C particles. Under these conditions, the cell potential for a given TCD is expected to again rise.

Figure 3.3 also helps rationalize the changes in the partial current densities for H_2 and CO seen in **Figure 3.2(b) and (c)**. Simulations of Ag MEAs have shown that the product partial current densities are very sensitive to the overpotential at the Ag particles that drives CO_2R.[46] In the present study, the composition and structure of the anode CL remain fixed as the I:Cat ratio of the cathode CL increase. Since the anode CL is in intimate contact with liquid water, it is reasonable to assume that the ionomer in the anode CL remains fully hydrated, as does the membrane. Under these constraints, the overpotential due to anode kinetics should be independent of the I:Cat ratio for the cathode CL and should only depend on the TCD. Likewise, if the membrane remains fully

hydrated, its conductivity will not change significantly and, hence, the ohmic loss across the membrane should increase linearly with the current density. Moreover, CO_2 can be lost due to buffer reactions involving OH^-, which produce HCO_3^- and CO_3^{2-}. As noted above, the latter process becomes increasingly severe as the extent of mass-transfer resistance increases at high TCD since OH^- is produced in direct proportion to the current. For I:Cat = 1 and 2, the number of ionomer tendrils connecting the Ag/C particles to the membrane is low, resulting in a relatively low cathode overpotential and subsequently mainly H_2 production.[59] When the I:Cat ratio increases to 3, there is now a sufficient number of ionomer tendrils to carry the current even at high current densities. Under these conditions, the cathode overpotential shifts to more positive values, thereby increasing the CO partial current density and FE. However, for yet higher current densities, mass-transfer effects start to set in, causing a decrease in the local CO_2 concentration due to the homogeneous buffer reactions, and, consequently, the CO partial current density does not rise as rapidly as that of H_2: the CO FE decreases as a result. When the I:Cat ratio rises to 4 and 5, the effects of CO_2 and OH^- transfer limitations are expected to become more significant because of thicker ionomer layers covering Ag/C particles.

These same I:Cat ratio trends were observed experimentally for the case of H_2O electrolysis (*i.e.,* HER-only at the cathode) in a H_2O-MEA containing an Ir anode CL and an Ag/C CL (see **Figure S3.6**). An I:Cat of 3 was again found to be best, suggesting that the CL structure (and perhaps associated water- and ion-transport limitations) dominate performance. The findings are consistent with the data of Xu *et al.*,[132] who characterized the CL microstructure by scanning electron microscopy (SEM) and nanometer-scale X-ray computed tomography (nano-XCT), which revealed that larger aggregates of ionomer-catalyst-carbon are formed with excessive ionomer amounts, resulting in a decrease in the ECSA.[132] It is important to note that several complexities and considerations arise when trying to link macroscale device performance to microscale ionomer-catalyst binding and distribution[125] and that, across a range of ionomer types and equivalent weights, changing the ionomer content or I:C ratio also influences the uniformity, morphology, and transport resistances of the CL.[133] Finally, the preferred I:Cat ratio of 3 found in our study (*i.e.,* an I:Cat of 3 corresponds to an I:C of 0.75 (see **Table S3.2**)) agrees with what was found for a proton-exchange-membrane fuel cell, where the preferred I:C ratio was close to 1.[134]

3.3.3 The effect of exchange-solution concentration

Previous studies have shown that adding an electrolyte behind the anode of an MEA improves the TCD obtained for a given cell potential relative to what is observed using pure water.[50,135–140] In this study, $CsHCO_3$ was added to the water circulated behind the anode CL, effectively producing an Exchange-MEA. For these experiments, the cathode CL I:Cat was 3 and the catalyst loading was 1 mg_{Ag} cm^{-2}.

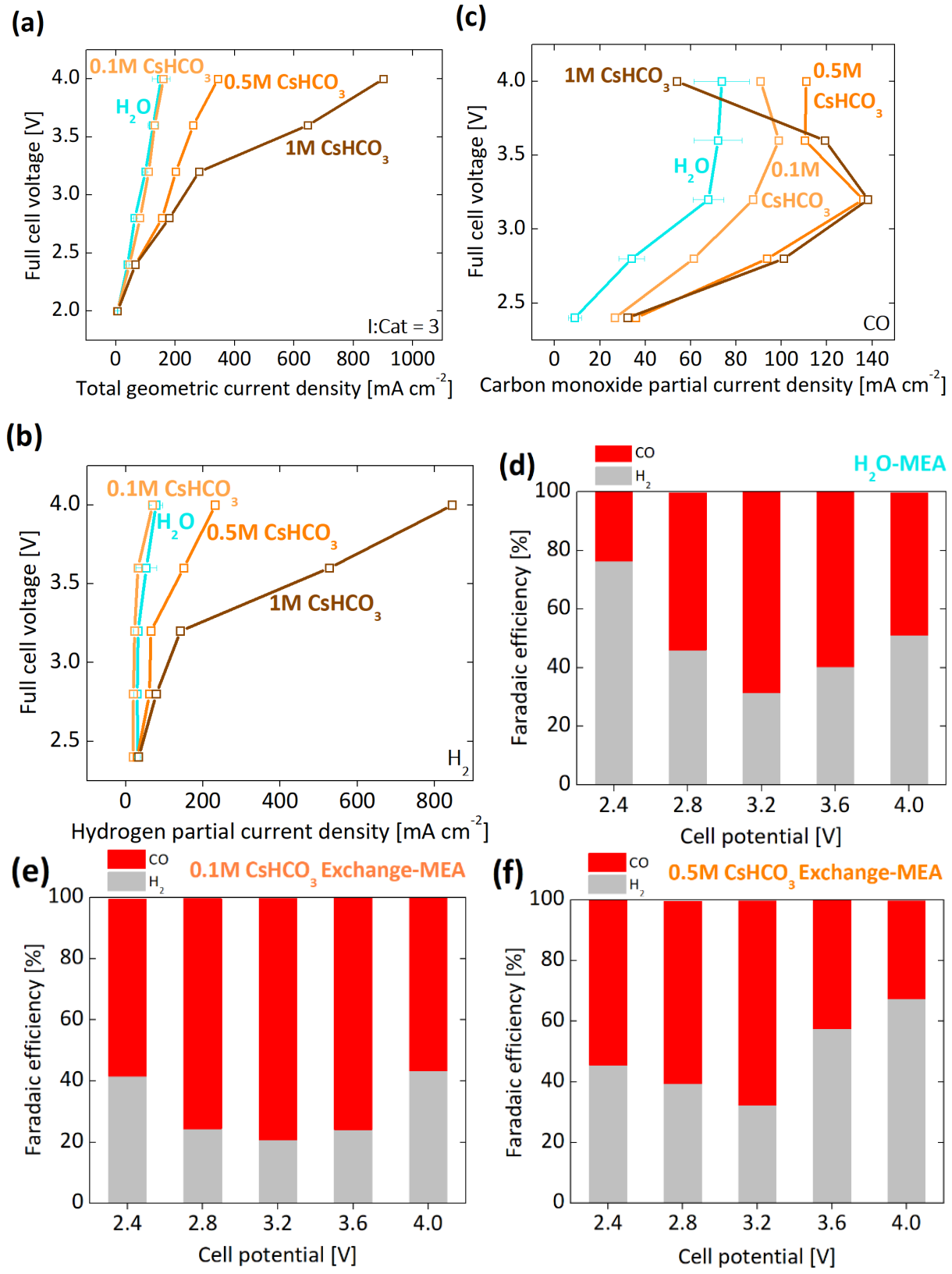
(a)
0.1M CsHCO3
H2O
0.5M CsHCO3
1M CsHCO3
I:Cat = 3
Full cell voltage [V]
Total geometric current density [mA cm-2]
(c)
1M CsHCO3
0.5M CsHCO3
H2O
0.1M CsHCO3
CO
Full cell voltage [V]
Carbon monoxide partial current density [mA cm-2]
(b)
0.1M CsHCO3
H2O
0.5M CsHCO3
1M CsHCO3
H2
Full cell voltage [V]
Hydrogen partial current density [mA cm-2]
(d)
CO
H2
H2O-MEA
Faradaic efficiency [%]
Cell potential [V]
(e)
CO
H2
0.1M CsHCO3 Exchange-MEA
Faradaic efficiency [%]
Cell potential [V]
(f)
CO
H2
0.5M CsHCO3 Exchange-MEA
Faradaic efficiency [%]
Cell potential [V]

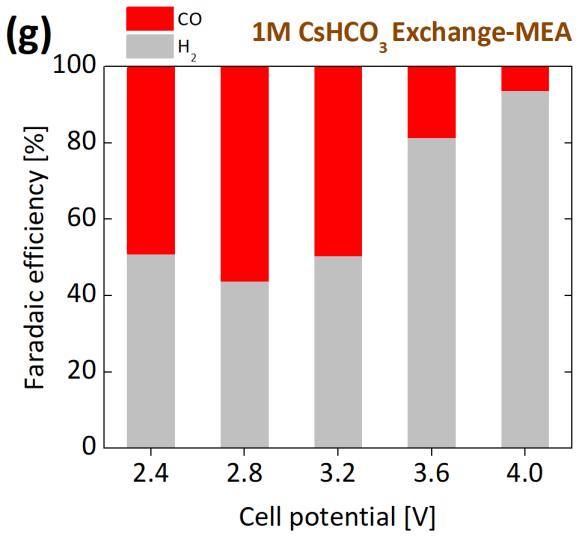

Figure 3.4. Polarization (a), hydrogen partial current density (b), and carbon monoxide partial current density (c) behavior as a function of exchange-solution concentration. Faradaic efficiency as a function of potential for the different concentrations: H_2O-MEA (d), 0.1 M $CsHCO_3$ (e), 0.5 M $CsHCO_3$ (f), 1 M $CsHCO_3$ (g) in a Ag cathode, Ir anode MEA. Test conditions are the same as those in **Figure 3.2** except that the cathodic I:Cat was fixed at 3 (weight basis) and that liquid water or $CsHCO_3$ was circulated behind the anode.

The addition of $CsHCO_3$ to the water fed behind the anode of the MEA has a noticeable impact on the TCD, as shown in **Figure 3.4(a)**, especially for concentrations approaching 1 M where current densities approach 1 A cm^{-2}. The increase in current density for a given applied potential is particularly significant above a cell potential of 2.5 V. These effects on the TCD are attributed to the creation of additional OH^- conduction pathways through the pores in the cathode CL (see **Figure 3.3**), which provide parallel pathways to the ionomer tendrils between the Ag/C particles and the AEM. We note that the migration of cations from the electrolyte behind the anode to the cathode CL through AEMs at high current densities has been predicted in simulations of Exchange-MEAs[46] and experimental studies have observed salt precipitation at the cathode when the electrolyte concentration exceeds its solubility limit.[75] As the ion concentration behind the anode increases, Donnan exclusion from the membrane is overcome and Cs^+ and HCO_3^- ions can now transport across the membrane. The creation of an electrolyte conduction pathway within the CL also increases the ECSA and improves CL utilization. These effects are consistent with the increased partial current density for CO and H_2 observed at higher cell potentials. A similar impact of electrolyte has been reported for a hydroxide-exchange-membrane water electrolyzers,[141] where the additional liquid-based ionic pathway becomes more favorable than the ionomer pathway as the exchange-solution ion concentration increases, further contributing to an increase in the ECSA.

The selectivity trends seen in **Figure 3.4(b) thru (g)** are attributed to the effect of the cathode overpotential coupled with the effect of CO_2 and OH^- transport at higher applied potentials. The presence of Cs^+ cations at the electrolyte/Ag interface and at a similar interface beneath the Sustainion® ionomer also enhances the activity of Ag for CO_2R because the accumulation of hydrated Cs^+ cations on the catalyst surface has been shown to strengthen the electrostatic field in the double layer and thereby enhance the CO_2 adsorption.[96,97] Furthermore, since the bicarbonate

ion has a lower pKa than water, at higher concentrations in the CL, it becomes a significant proton donor supply and buffering agent, which reduces the local pH and promotes HER.[100,142] In addition, when HFR EIS was conducted for the MEA and operated at a fixed current density of 500 mA cm^{-2} with a 0.5 M or a 1 M $CsHCO_3$ solution behind the anode catalyst layer, the total resistance measured was 0.14Ω and 0.13Ω, respectively. By contrast, within its current density range, the resistance of the H_2O-MEA system was just under 0.2 Ω. Thus, ohmic resistance was not a controlling factor in the performance of the Exchange-MEA. These various effects are coupled and not readily deconvoluted without additional advanced characterization techniques or mathematical models that are beyond the scope of the current study. The effects of the applied cell potential on the partial current densities and the FE for CO are qualitatively similar to those seen in **Figure 3.2**, but are more dramatic. While the CO FE is highest (79%) for 0.1 M $CsHCO_3$ Exchange-MEA (see **Figure 3.4(e)**), the CO partial current density is highest for 0.5 and 1 M $CsHCO_3$ (*i.e.,* CO partial current densities > 100 mA cm^{-2}, see **Figure 3.4(c)**). Furthermore, for a constant current density, the CO partial current density for 1 M $CsHCO_3$ system is higher than that for 0.5 M $CsHCO_3$. These observations reinforce why FE trends are an insufficient basis for judging CO_2R performance and why it also important to look at the CO partial current density.[143,144]

3.3.4 The effect of catalyst loading and catalyst-layer thickness

As noted above, substitution of water by a $CsHCO_3$ solution enhances the activity of the Ag/C particles in the cathode CL and reduces the net resistance of the CL to anion transport. The next question explored was the effect of changing the number of active sites by changing the catalyst mass loading (mg_{Ag} cm^{-2}) and, hence, the thickness of the cathode CL. These experiments were carried out with a fixed Ag to carbon ratio (Ag/C) of 20 wt.-%, a cathodic I:Cat = 3, and a 1 M $CsHCO_3$ exchange solution behind the anode.

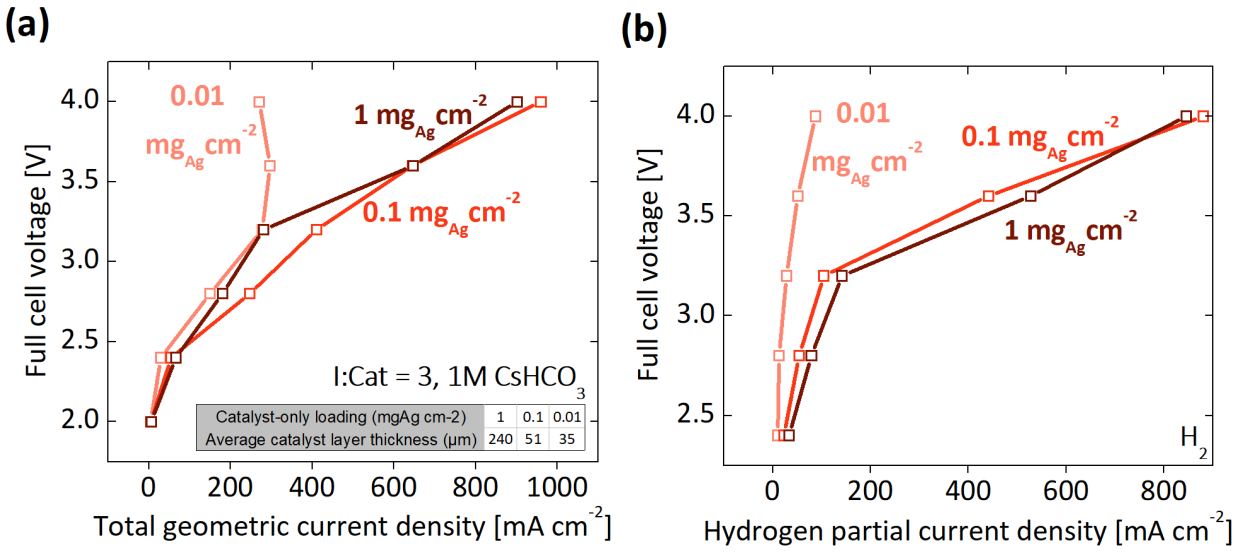

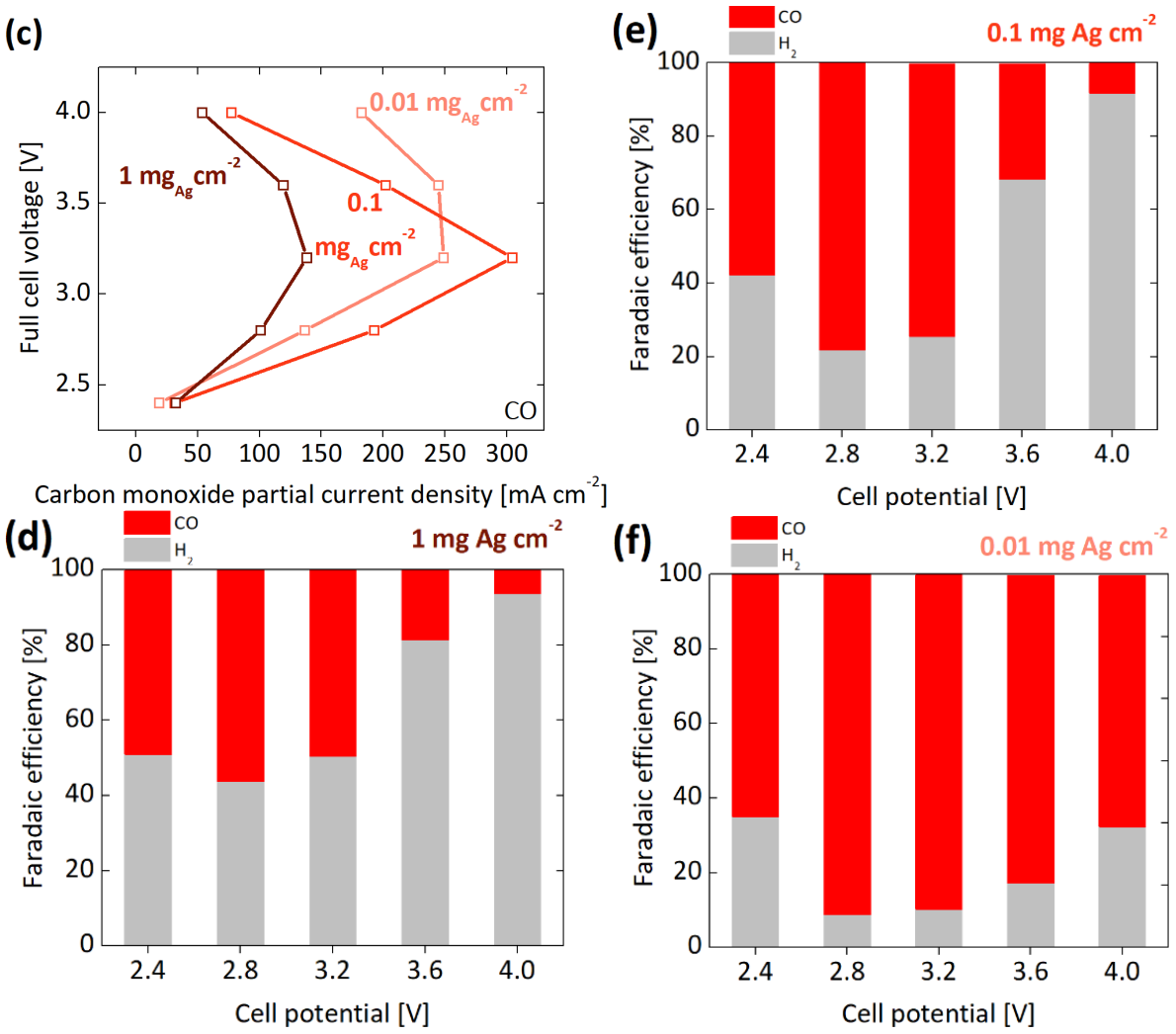

Figure 3.5. Polarization (a), hydrogen partial current density (b), and carbon monoxide partial current density (c) behavior as a function of Ag catalyst loading. Faradaic efficiency as a function of potential for the different loadings: 1 mg_{Ag} cm^{-2} (d), 0.1 mg_{Ag} cm^{-2} (e), 0.01 mg_{Ag} cm^{-2} (f) in a Ag cathode, Ir anode MEA. Test conditions are the same as those in **Figure 3.2** except that the cathodic I:Cat was fixed at 3 (weight basis) and 1M $CsHCO_3$ was circulated behind the anode. A pressure-sensing Mitutoyo® micrometer was used to obtain the catalyst-layer thickness measurements shown in the inset table in (a).

Figure 3.6(a) thru (c) shows the effect of catalyst loading on the TCD and the partial currents for H_2 and CO. Decreasing the Ag loading from a nominal value of 1 to 0.1 mg_{Ag} cm^{-2} did not significantly alter the TCD over the whole range of cell potentials. However, when the loading was further reduced to 0.01 mg_{Ag} cm^{-2}, the TCD exhibited similar limiting-current behavior to that seen when the I:Cat ratio was reduced from 3 to 1 (see **Figure 3.2**). This pattern suggests that the most active part of the CL is that located near the membrane surface, consistent with earlier studies of CO_2R in an MEA system.[59,77,145] One of these studies[59] revealed that the cathode potential on the Ag particles in the cathode CL became significantly more positive with increasing distance from

the CL/membrane interface as a consequence of the increasing resistance to OH^- mass transfer. Consistent with this reasoning, **Figure 3.7(a)** suggests that only about 10% of the CL layer at a catalyst loading of 1 mg_{Ag} cm^{-2} is actually active (*i.e.,* ~20 μm). Further reduction of the Ag loading to 0.01 mg_{Ag} cm^{-2} reveals that, if the loading is too low, the current that needs to be supplied by each particle in the CL rises, resulting in an increase in mass-transport limitations to and from the catalyst surface due to the decreased ECSA, as well as a reduction in the availability of conduction pathways via the electrolyte in the pores of the CL due the smaller CL volume (at fixed I:Cat) having reduced contact sites of the electrolyte with ionomer tendrils and Ag/C particles. These phenomena help explain the observed sudden rise in the cell potential required to achieve current densities of more than ~250 mA cm^{-2}.

It is notable that reducing the catalyst loading from 1 to 0.1 mg_{Ag} cm^{-2} does not have a large effect on the partial current density for H_2, yet results in a substantial increase in the partial current density and FE for CO. For cell potentials below the optimal 3.2 V, in which the TCD is essentially independent of Ag loading, the partial current density for CO increases as the Ag loading decreases but remains largely unchanged from 0.1 mg_{Ag} cm^{-2} to 0.01 mg_{Ag} cm^{-2}. However, the CO FE greatly increases over this same loading range (*i.e.,* a CO FE of 78% was attained at 0.1 mg_{Ag} cm^{-2} and a very high CO FE of 91% was attained at 0.01 mg_{Ag} cm^{-2} at a 3.2 V). This is not due to a particularly large increase in the CO partial current density, but rather due to a significant decrease in the H_2 one. For each loading, the CO partial current density goes through a broad maximum, while the H_2 partial current density increases monotonically as the overpotential increases. A constant-current comparison of the selectivity data (see **Figure S3.3(g) thru (i)**) also shows this maximum in CO partial current density as a function of Ag loading, most especially for 0.1 mg_{Ag} cm^{-2}. We believe that this is attributable to the higher cathode overpotential preferentially shifting the product selectivity to products with larger transfer coefficients.[59] For Ag, the product with the larger transfer coefficient is CO ($\alpha_{COER} = 0.44$ and $\alpha_{HER} = 0.36$).[56] It is also notable that decreasing the catalyst loading to 0.01 mg_{Ag} cm^{-2} dramatically decreases the partial current density for H_2, but has a much more modest effect on the partial current density to CO. This pattern may reflect a lower H_2O/CO_2 ratio at the catalyst surface.

3.4 Conclusions

This work explored the role of the cathodic ionomer-to-catalyst (I:Cat) ratio, catalyst loading, catalyst-layer thickness, and anode exchange-solution concentration in CO_2 reduction (CO_2R) for a membrane-electrode-assembly (MEA) containing supported Ag/C catalysts at the cathode. The aim of this work has been to understand the influence of these parameters on the total current density, the rate of CO formation, and its associated faradaic efficiency (FE). We have found that when only water is present in the anode compartment behind the anode CL, both the anion-exchange membrane (AEM) and associated ionomer in contact with the Ag particles are essentially completed hydrated, avoiding dehydration phenomena that can limit catalytic performance. However, the total current density and the CO partial current density are both sensitive to the I:Cat ratio. For I:Cat ratios of 1 and 2, the electrochemically-active surface area (ECSA) is low and the total current density is limited by mass transport of CO_2 and OH^- through the ionomer tendrils connecting the Ag particles to the AEM. Under these conditions, the OH^- concentration and production rate near the Ag surface are high, which reduces the local

concentration of CO_2 due to reaction with OH^- to produce HCO_3^- and CO_3^{2-}; this results in H_2 being the primary product. For I:Cat ratios of 3 and greater, the ECSA is higher and these mass-transfer limitations are ameliorated at lower total current densities, and, consequently, CO is produced with greater FE and current density. However, mass-transfer limitations are observed at high current densities. The addition of $CsHCO_3$ to the water in the anode compartment increases significantly the total current density attained for a given applied potential. This is ascribed to the creation of parallel channels for OH^- conduction from the Ag particles via electrolyte present in the pores of the CL, between the ionomer tendrils and the AEM. The presence of electrolyte in the cathode CL also increases the CO partial current density relative to that for H_2, but at high applied potentials where mass-transfer limitations set in, the CO partial current density decreases relative to that for H_2. The catalyst loading, expressed as milligrams of Ag per square centimeter of cathode area ($mg_{Ag}\,cm^{-2}$), also has an effect on the total current density and the CO partial current density. For an I:Cat ratio of 3 and a $CsHCO_3$ concentration of 1 M, reducing the catalyst loading from 1 to 0.1 $mg_{Ag}\,cm^{-2}$ has little effect on the total current density but increases the CO FE substantially. A further decrease in the Ag loading to 0.01 $mg_{Ag}\,cm^{-2}$ leads to a significant reduction in total current density for a given cell potential and a significant reduction in the H_2 partial current density relative to the CO partial current density. The observed effects suggest that for a loading of 1 $mg_{Ag}\,cm^{-2}$, only a tenth of the catalyst is active for CO_2R, but that reducing the loading below 0.1 $mg_{Ag}\,cm^{-2}$ leads to a large loss in ECSA and the onset of significant local mass-transfer limitations; however, the high ratio of CO to H_2 partial currents and very high CO FEs in this latter case cannot be fully explained and warrants further study. Overall, at low enough catalyst loading with constant I:Cat *or* at low enough I:Cat with constant catalyst loading, the CO_2R MEA system becomes severely limited by ECSA, poor CO_2 utilization, and mass-transfer limitations.

In summary, this present study illustrates the importance of cathode CL design for achieving high, industrially-relevant total current densities (*i.e.,* 200 mA cm^{-2} to 1 A cm^{-2}) and concurrently high CO FEs (*i.e.,* 78% to 91%), with a recommended range of cathode parameters being catalyst loadings of 0.01 to 0.1 $mg_{Ag}\,cm^{-2}$ with thicknesses on the order of tens of micrometers and with an intermediate I:Cat ratio of 3, as well as a 1 M $CsHCO_3$ anode exchange solution. Our findings also revealed that, despite its solid-state ionomer-based design, under certain operating conditions, the MEA architecture can behave similarly to planar and aqueous GDE cells in their inherent ability to highly tune CO_2R selectivity with their electrode/electrolyte interfaces. This points to an increased possibility of knowledge transfer of fundamental scientific insights from the wider aqueous CO_2R literature across seemingly disparate device systems. Moreover, we find that our interpretations and hypotheses of the effects of catalyst-layer design factors (such as I:Cat, catalyst loading, and catalyst-layer thickness) on performance are largely correlated due to the interrelated nature of the metrics themselves and how a change in one factor can influence the other in the complex and interconnected catalyst-layer microenvironment. These findings not only provide much needed engineering guidance in the form of design factor optimization, but they also provide foundational scientific insights that improve our understanding of the physical phenomena tradeoffs in CO_2R MEAs and should be readily applicable to a broad range of commercializable CO_2R MEA-based devices.

3.5 Supporting Information

Cathode catalyst ink recipe

I:Cat	Ag/C catalyst (mg)	water (g)	n-propanol (g)	ionomer solution (mg)
1	81	8.1	8.1	324
2	81	8.1	8.1	648
3	81	8.1	8.1	972
4	81	8.1	8.1	1296
5	81	8.1	8.1	1620

Anode catalyst ink recipe

Ir catalyst (mg)	water (g)	n-propanol (g)	ethanol (g)	ionomer solution (mg)
41	8.3	13.3	6.5	96

Table S3.1. Catalyst ink recipes. Recipes are for a catalyst-only loading of 1 $mg_{catalyst}$ cm^{-2}. Ag catalyst weight is 20 wt.-% with Vulcan carbon support. The Sustainion® ionomer solution contains 5 wt.-% ionomer dispersed in ethanol. The iridium catalyst is IrO_2 (Tanaka Kikinzoku Kogyo K.K®, SA=100).

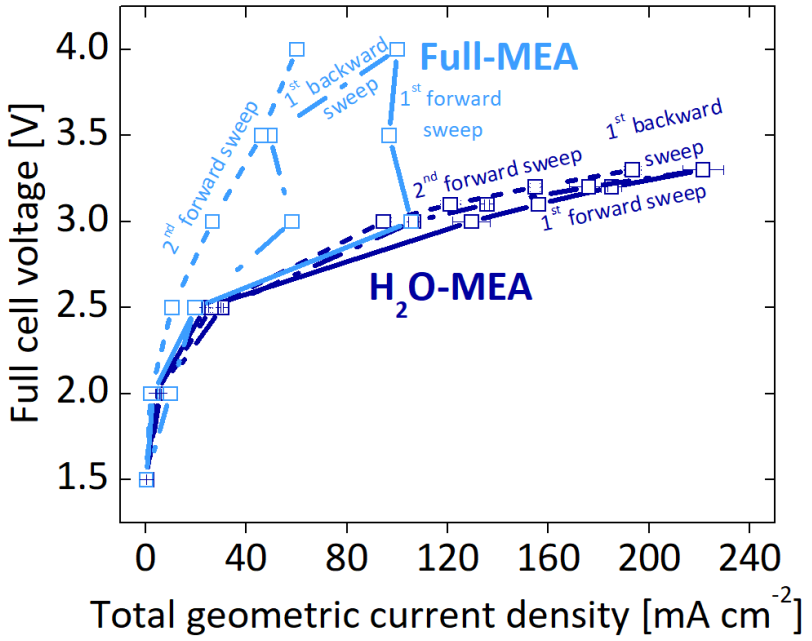

Figure S3.1. The effect of MEA cell design on the AEM water electrolysis polarization curve and hysteresis in a Ag cathode, Ir anode MEA system: Full-MEA vs. H_2O-MEA. Forward and backward

voltage sweeps were conducted to obtain a hysteresis/stability measure. The system temperature was maintained at ambient (22-25ºC) temperature and under atmospheric pressure conditions. Sustainion® ionomer and membrane were used and the catalyst loading at each electrode was 1 $mg_{catalyst}$ cm^{-2}. The anodic ionomer content and cathodic I:Cat were fixed at 11.6 wt.-% and 2, respectively (weight basis). Humidified Ar feed flow rate at the cathode inlet was at least 200 mL min^{-1}, while liquid water was circulated behind the anode. H_2 faradaic efficiencies were consistently above 95%. The H_2O-MEA cell design outperforms the Full-MEA in terms of total current density and stability between voltage sweeps. This is due to its increased water availability, which provides more reactant for cathode reactions and an increased degree of hydration, staving off (reversible) dehydration and (irreversible) degradation of the membrane and ionomer phases, especially at higher current densities.

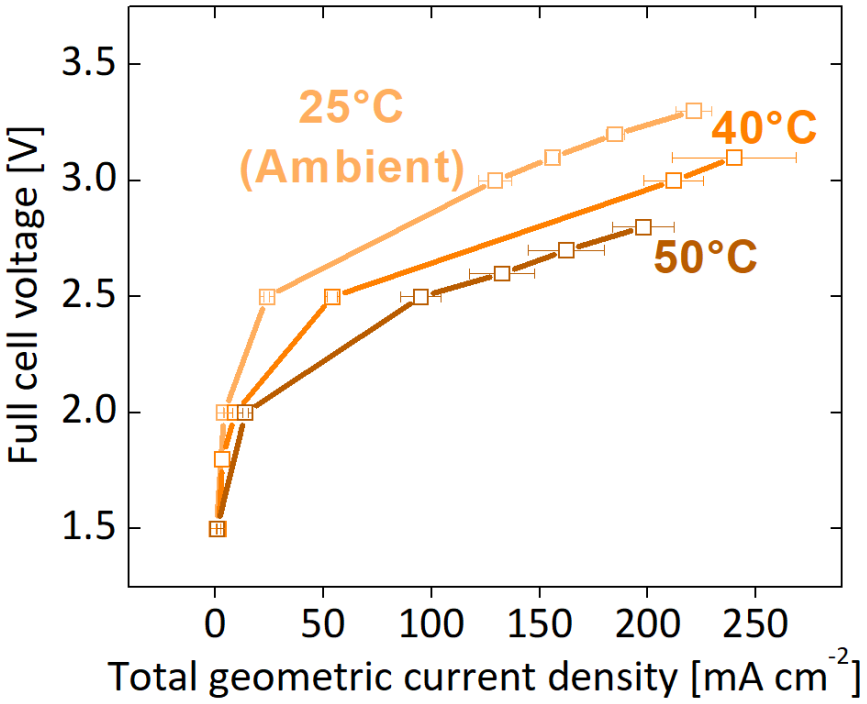

Figure S3.2. The effect of system temperature on the AEM water electrolysis polarization curve in a Ag cathode, Ir anode H_2O-MEA system. Test conditions were the same as those in **Figure S3.5** except that the system temperature was varied. As expected, operating at elevated system temperatures yields a marked increase in the current-voltage response, leading to almost a doubling of the performance at some applied potentials. This supports the notion of increased kinetic activity and transport observed in electrolyzers due to increased system temperature.

I:Cat	1	2	3	4	5
I:C	0.25	0.5	0.75	1	1.25

Table S3.2. Ionomer-to-catalyst ratio (I:Cat) and ionomer-to-carbon ratio (I:C) conversion table. Ag catalyst weight is 20 wt.-% with Vulcan carbon support.

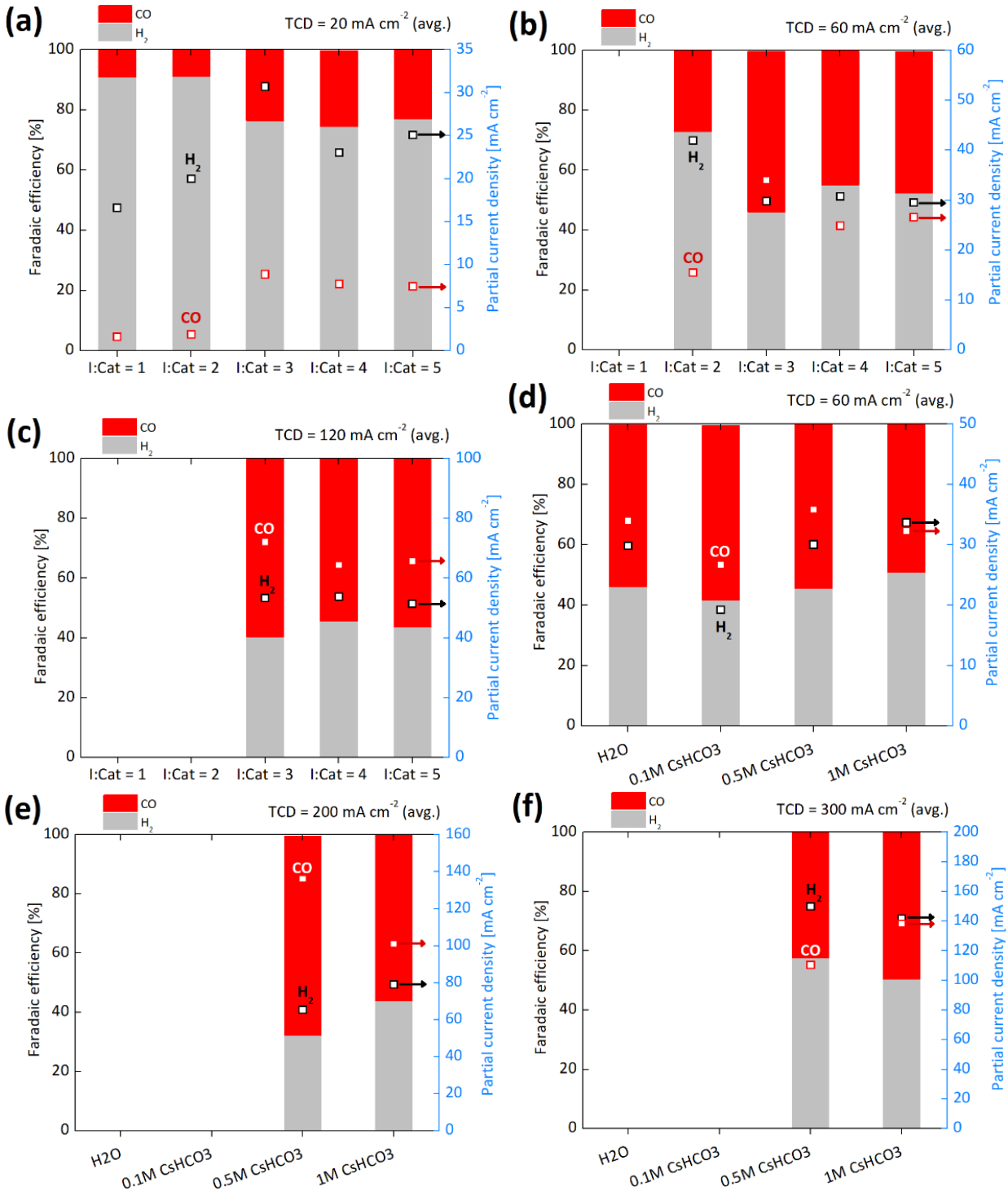
(a)
TCD = 20 mA cm-2 (avg.)
(b)
TCD = 60 mA cm-2 (avg.)
(c)
TCD = 120 mA cm-2 (avg.)
(d)
TCD = 60 mA cm-2 (avg.)
(e)
TCD = 200 mA cm-2 (avg.)
(f)
TCD = 300 mA cm-2 (avg.)
CO
H2
Faradaic efficiency [%]
Partial current density [mA cm-2]
I:Cat = 1
I:Cat = 2
I:Cat = 3
I:Cat = 4
I:Cat = 5
H2O
0.1M CsHCO3
0.5M CsHCO3
1M CsHCO3

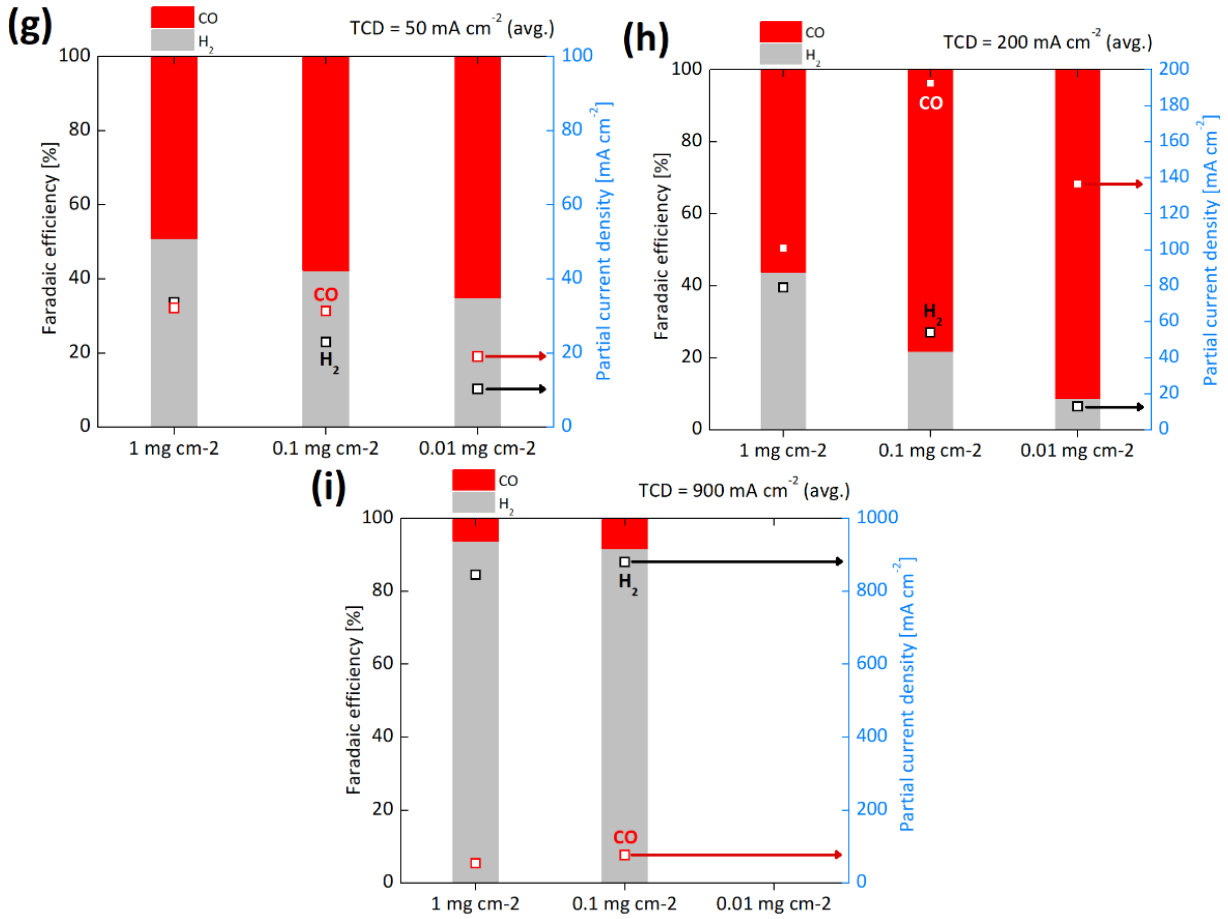

Figure S3.3. Comparison of the CO_2 reduction (*i.e.*, CO and H_2) faradaic efficiency and partial current density selectivity behavior of each experimental study (*i.e.*, I:Cat ratio [(a) – (c)], anode exchange solution concentration [(d) – (f)], and catalyst loading [(g) – (i)]) at similar current densities in a Ag cathode, Ir anode MEA. Test conditions are the same as those in **Figure 3.2**, **Figure 3.4**, and **Figure 3.5**, respectively. **Note that the scale of the right y-axis for the partial currents (in light blue) varies widely across experiments.**

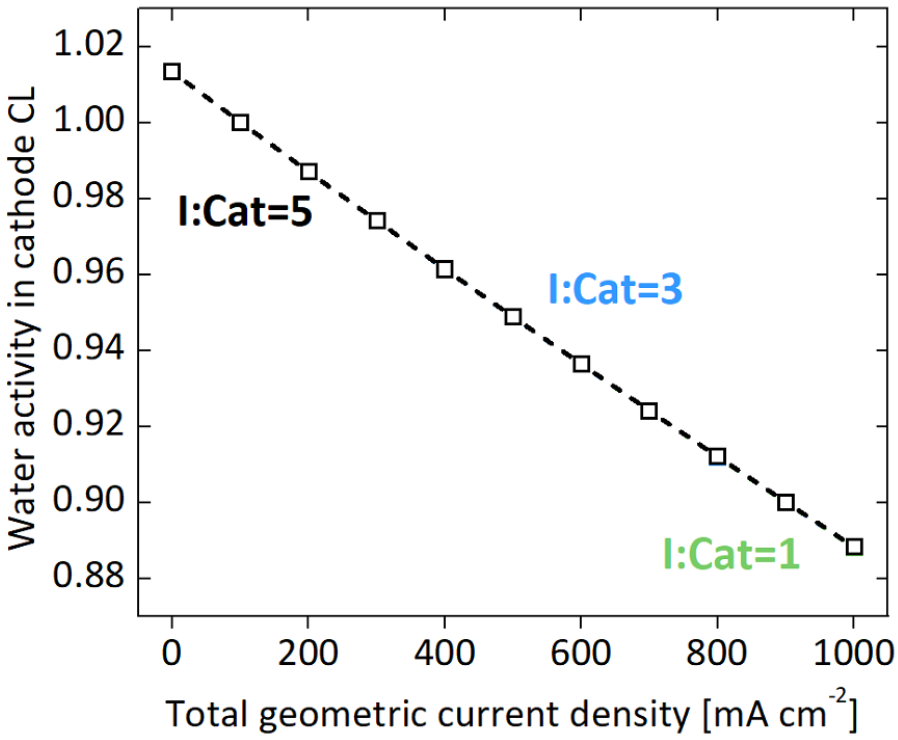

Figure S3.4. Ionomer dehydration model of the cathode catalyst layer across various total current densities and cathodic I:Cat ratios. The total current density is employed as a sweeping parameter, while the dependent variable is the water activity in the cathode catalyst-layer (CL) control volume. This sensitivity analysis is carried out for cathode I:Cat ratios 1, 3, and 5. It is clear that ionomer dehydration (*i.e.,* water activity = 0) does not occur at all across the wide current density range (even at current densities reaching 1 A cm^{-2}) and that the CL is mostly well hydrated, enough for possibly the emergence of a separate liquid phase in the CL. The contribution of ohmic heating to the drying phenomena in the CL was the least of the water fluxes obtained from the model. Although hard to distinguish from the figure, the I:Cat = 1 system has the overall lowest water activities, followed by the I:Cat = 3 system and then the I:Cat = 5 system. Testing out lower CL utilizations (*i.e.,* 10% = 0.1 mg_{Ag} cm^{-2} vs. 1% = 0.01 mg_{Ag} cm^{-2}) revealed that lower CL utilizations yielded slightly higher water activities across the board, indicating that the cathode CL is more hydrated in the regions or thicknesses closer to the membrane. A number of water transport coefficients and properties used in the model were based on Nafion® yet AEMs like Sustainion® are expected to have higher water transport properties, meaning that the water activities likely present in the CL during operation would actually be higher than what is shown in the figure above. This model was programmed using Python® and a scipy.optimize solver.

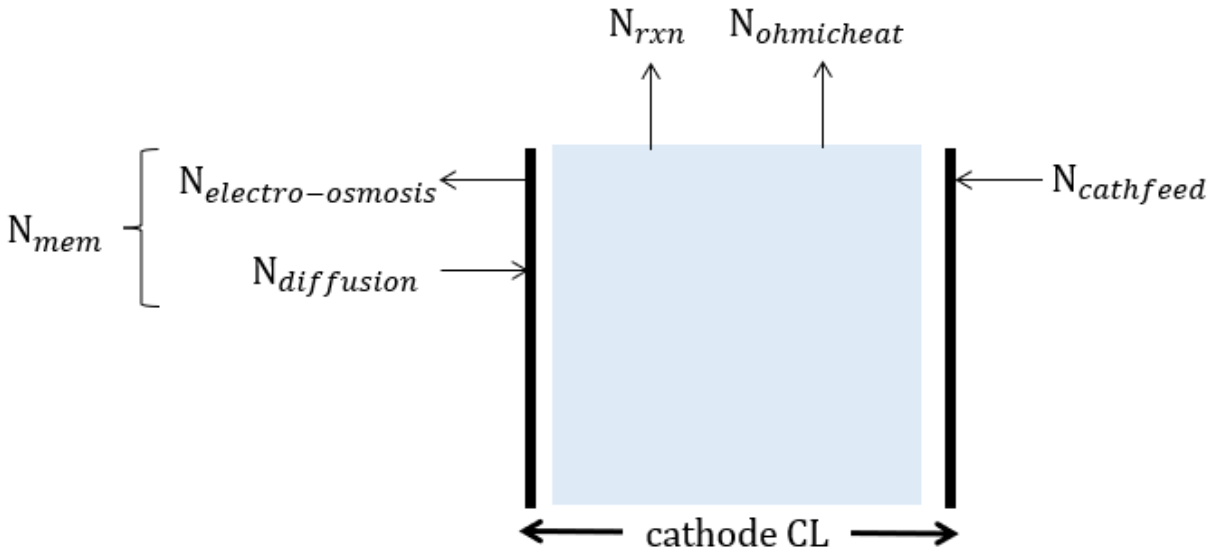

Term	Equation/Value	Source/Assumptions
total net water flux/accumulation	total water flux in – total water flux out $[\frac{\text{mol}}{\text{cm}^2\ \text{s}}]$	
total water flux in	$N_{\text{diffusion}} + N_{\text{cathfeed}}\ [\frac{\text{mol}}{\text{cm}^2\ \text{s}}]$	
total water flux out	$N_{\text{ohmicheat}} + N_{\text{rxn}} + N_{\text{electro-osmosis}}\ [\frac{\text{mol}}{\text{cm}^2\ \text{s}}]$	
total current density, i	$0 - 1000\ \left[\frac{\text{mA}}{\text{cm}^2}\right] = 0 - 1\ [\frac{\text{A}}{\text{cm}^2}]$	
geometric surface area, A_{geo}	$5\ [\text{cm}^2]$	
water activity in CL (also a measure of relative humidity)	$a_{\text{water,CL}}$	
$N_{cathfeed}$, amount of water into CL from humidified cathode feed	$k_{g,\text{feed}} \times (a_{\text{water,feed}} - a_{\text{water,CL}}) \times \frac{P_{\text{water}}^{\text{vap}}}{RT}\ [\frac{\text{mol}}{\text{cm}^2\ \text{s}}]$	$P_{\text{water}}^{\text{vap}}$ is the vapor pressure of water at the system temperature and $a_{\text{water,feed}} = 1$ since the humidified cathode feed is at 100% RH
$k_{g,feed}$, mass transfer coefficient of water through the cathode GDL	$\frac{D_{\text{eff,water}}}{\delta_{\text{GDL}}}\ [\frac{\text{cm}}{\text{s}}]$	

$D_{eff,water}$, effective diffusion coefficient of water via the GDL	$0.138 \times \frac{\epsilon_{GDL}}{\tau_{GDL}} [\frac{cm^2}{s}]$	apparent diffusion coefficient from Table II[146] and ϵ_{GDL} = 0.52 (for SG 39 BC Sigracet®) and τ_{GDL} is obtained via Bruggeman's correlation
δ_{GDL}, GDL thickness	$325\ [\mu m] = 0.0325\ [cm]$	SG 39 BC, Sigracet®
T, system temperature	$50°C$	
$N_{diffusion}$, amount of water entering the CL from the membrane/anode	$\left(\frac{\alpha_{L_{mem}}}{\delta_{mem}} VdP\right) + \left(\frac{\alpha_{V_{mem}}}{\delta_{mem}} RT \times -\ln(a_{water,CL})\right) [\frac{mol}{cm^2\ s}]$	where V is the partial molar volume of water ($\overline{V_0}$) and dP is an assumed pressure differential between the water behind the anode and the membrane/cathode CL interface (1 atm)
$\alpha_{L_{mem}}$, membrane water transport coefficient based on a pressure gradient driving force	$\frac{k_{sat}}{\mu \times \overline{V_0}^2} \left[\frac{mol^2}{J\ cm^2\ s}\right]$	Equation 54[147] k_{sat} is the permeability of a completely liquid-filled membrane[147] and the viscosity and partial molar volume are that of water at the system temperature
$\alpha_{V_{mem}}$, membrane water transport coefficient based on a chemical-potential driving force	$5 \times 10^{-10}\ [\frac{mol^2}{J\ cm^2\ s}]$	Figure 6[147]
δ_{mem}, membrane thickness	$50\ [\mu m] = 0.005\ [cm]$	for Sustainion® membrane[46]
N_{rxn}, amount of water consumed by reaction	$\frac{100\% \times i}{2 \times F} [\frac{mol}{cm^2\ s}]$	based on Faraday's law, assuming 100% CO FE COER: $CO_2 + H_2O + 2e^- \rightarrow CO + 2OH^-$
$N_{ohmicheat}$, amount of water consumed/evaporated by ohmic heating	$\frac{\text{power generated in CL}}{\Delta H_{vap,water} \times \text{molar mass of water} \times A_{geo}}$ $[\frac{mol}{cm^2\ s}]$	
$\Delta H_{vap,water}$, enthalpy of vaporization of water	$2381.9\ [\frac{KJ}{kg}]$	at system temperature

power generated in CL	$I^2R = (i \times A_{geo})^2 \times R_{eff}$ [W]	
R_{eff}, effective resistance in CL	$\frac{\text{active CL thickness}}{\sigma_{ionomer} \times A_{geo}} \times \frac{\in}{\tau}$ [Ω]	
$\sigma_{ionomer}$, ionomer conductivity	$\sigma_{ionomer} = 2\ (0.006e^{6.21 \times a_{water,CL}})$ $[\frac{S}{m}]$	Table S2[59]
CL thickness	80 [μm] = 0.0080 [cm]	average CL thickness (see **Figure S3.7**)
active CL thickness	CL utilization × CL thickness	portion of CL that is actually generating current
CL utilization	10% (or 1%)	see **Figure 3.5**
∈, CL porosity	62% for I:Cat = 1, 34% for I:Cat = 3, 5% for I:Cat = 5	see **Figure S3.7**
τ, CL tortuosity	$\in^{-0.5}$	via Bruggeman's correlation
I:Cat ratio	1, 3, or 5	atalyst loading is 1 mg_{Ag} cm^{-2}
$N_{electro-osmosis}$, amount of water leaving the CL via the membrane due to electro-osmosis	$\frac{\varepsilon \times i}{F}$ $[\frac{mol}{cm^2\ s}]$	assuming mole fraction of hydroxide ion $y_{OH^-} = 1$ and the charge of ion $z_{OH^-} = 1$
ε, electroosmotic coefficient	3	for liquid equilibrated membranes[59]

Table S3.3. Modeling parameters used in ionomer dehydration model.

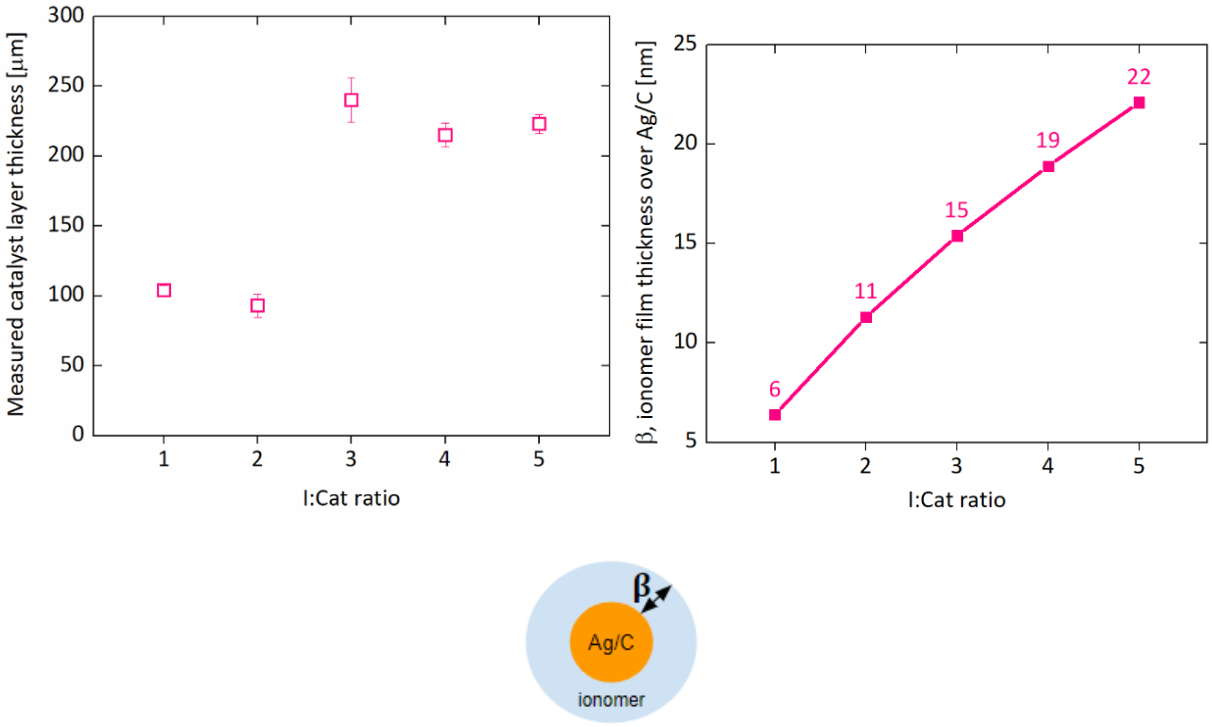

I:Cat	1	2	3	4	5
Estimated ionomer volume fraction	14%	29%	43%	57%	72%
Estimated catalyst volume fraction	1.19%	1.19%	1.19%	1.19%	1.19%
Estimated carbon volume fraction	22.1%	22.1%	22.1%	22.1%	22.1%
Resulting porosity	62%	48%	34%	19%	5%

Figure S3.5. Measured cathode catalyst-layer thickness, estimated ionomer thickness (β), and component volume fractions vs. cathodic I:Cat. An average empirical cathodic catalyst-layer thickness of 175 µm was obtained from pressure-sensing micrometer (Mitutoyo®) measurements. The ionomer, catalyst, carbon, and realistically expected pore void content were calculated on a volume basis for each I:Cat based on their catalyst ink recipe (see **Table S3.1**) and an assumed CL thickness of 80 µm. The ionomer volume content calculated was converted to an estimated ionomer thickness (β) based on spherical geometric arguments. Volume fractions were calculated based on loading, CL thickness, catalyst nanoparticle, carbon, and ionomer physical proprieties.

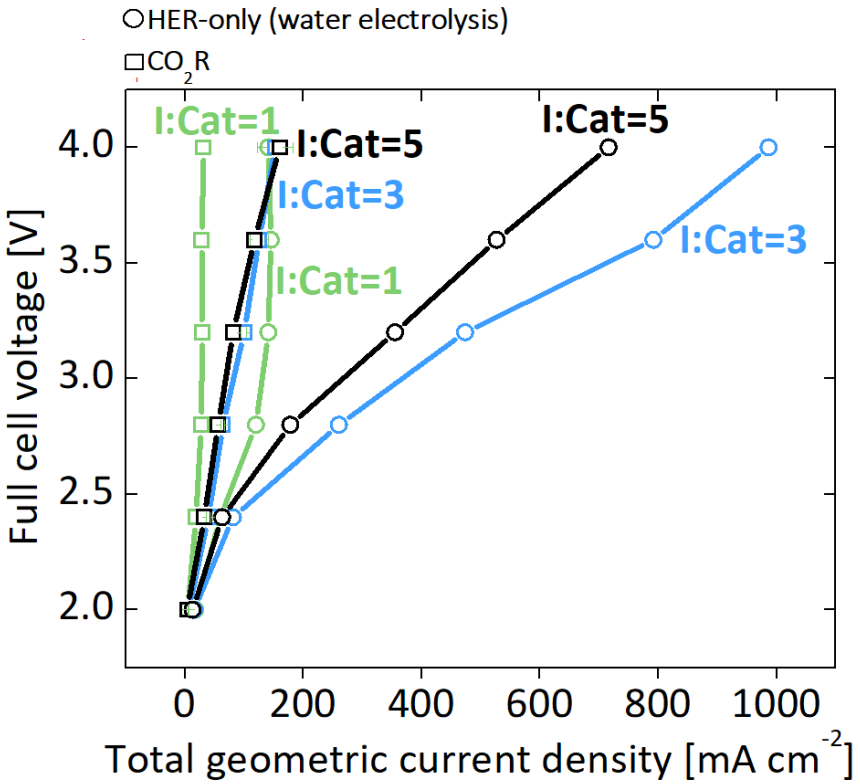

Figure S3.6. Comparison of CO_2 reduction and AEM water electrolysis polarization curves across constant cathodic I:Cat. HER-only test conditions: 50°C, atmospheric pressure, at least 200 mL min^{-1} fully humidified Ar feed at the cathode, liquid water on the anode. H_2 faradaic efficiencies were consistently above 95%. CO_2R test conditions: same as **Figure 3.2**. Comparing the MEA performance between these two separate processes (*i.e.,* the splitting of water and the reduction of CO_2) across the same potential range, operating conditions, and I:Cat ratio reveals that the mere presence of CO_2 causes a depression in the system's current-voltage response for a variety of reasons such as ohmic and anodic and cathodic Nernstian overpotential limitations.[148]

4 Studies on the Ag/ionomer Interface and Its Impact in CO_2 Reduction MEA Systems

The authors gratefully acknowledge Lawrence Berkeley National Laboratory's Laboratory Directed Research and Development (LDRD) Grant for funding. This material is also partially based upon work performed by the Joint Center for Artificial Photosynthesis, a DOE Energy Innovation Hub, supported through the Office of Science of the U.S. Department of Energy under Award Number DE-SC0004993.

A multiphysics continuum model was developed by Eric W. Lees and interfacial capacitance studies were performed by Dr. Arthur R. Dizon. Transmission electron microscopy (TEM) and powder X-ray diffraction (PXRD) were performed by Daewon Lee in Prof. Haimei Zheng's group, supported by the U.S. Department of Energy, Office of Science, Office of Basic Energy Sciences (BES), Materials Sciences and Engineering Division under Contract No. DE-AC02-05-CH11231 within the *in-situ* TEM program (KC22ZH). Work at the Molecular Foundry of Lawrence Berkeley National Laboratory (LBNL) was supported by the U.S. Department of Energy under Contract No. DE-AC02-05CH11231. D.L. acknowledges the Kwanjeong Study Abroad Scholarship from the KEF (Kwanjeong Educational Foundation) (KEF-2019).

4.1 Introduction

Membrane-electrode assemblies (MEAs) are key commercializable devices for CO_2 reduction (CO_2R) that warrant comprehensive investigation due to their ability to offer enhanced transport phenomena and selectivities at moderately applied overpotentials.[46] A critical aspect of MEAs are their characteristic ionomer-based, multicomponent catalyst layers (CLs), a complex microenvironment of ionic, electronic, and gaseous pathways.[58,62] The cathode CL in particular contributes heavily to the activity, selectivity, and overall performance observed in the CO_2R MEA.[62] Chapter 3 demonstrated the crucial impact of key cathode CL design parameters like the I:Cat ratio and CL thickness/loading on activity and selectivity and these findings outline a pathway towards high performance Ag CO_2R MEAs. Thus, it is necessary to have a more in-depth understanding of the cathode CL microenvironment and its catalyst/ionomer interfaces, considering that optimal CO_2R (*i.e.,* high CO_2R product selectivity and activity) should stem from a cathode microenvironment with a high local pH and $[CO_2]$:$[H_2O]$ ratio.[62] The interface and interaction between the ionomer and catalyst is of great importance in the CO_2R MEA system, yet, save for a few cursory studies and reviews,[149–153] the quantifiable impact of the Ag/ionomer interface and its pH or chemistry on activity, selectivity, CO_2 crossover, interfacial capacitance, and other performance behaviors is largely unknown. This chapter probes and characterizes this interface for different ionomer chemistries and explores how it influences controlling phenomena to help explain observed macroscale CO_2R behaviors, while simultaneously improving overall system performance by manipulating this interfacial microenvironment.

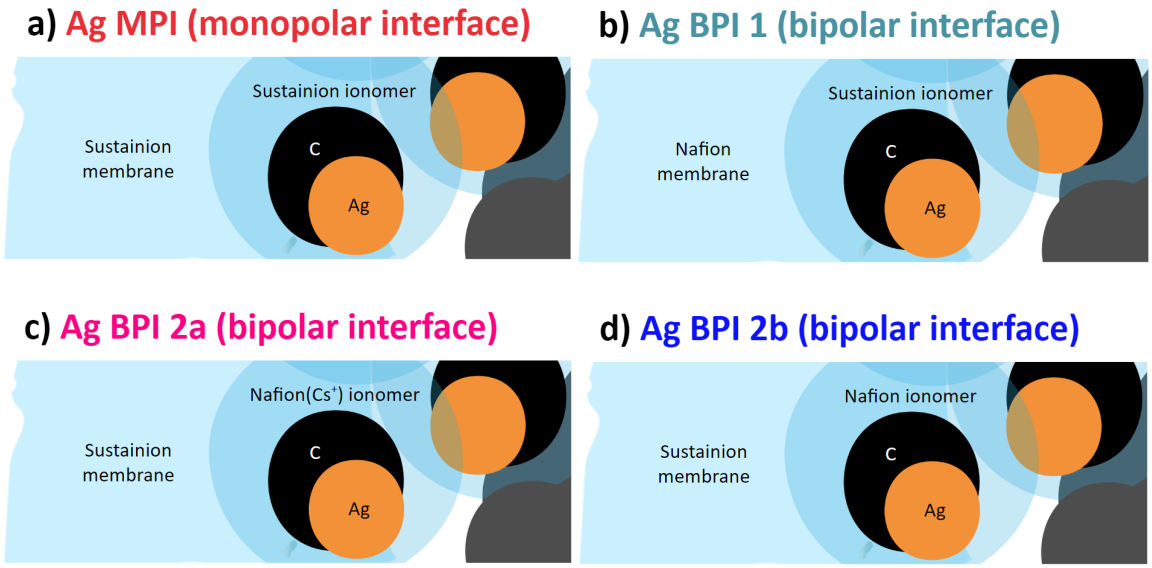

Figure 4.1. Schematic of the different Ag/ionomer interfaces explored within this study: a Ag monopolar interface (MPI) system that consists of a Ag/Sustainion ionomer with a Sustainion membrane (a), a Ag bipolar interface (BPI 1) system that consists of a Ag/Sustainion ionomer with a Nafion membrane (b), a Ag bipolar interface (BPI 2a) system that consists of a Ag/Nafion ionomer exchanged with Cs^+ cations with a Sustainion membrane (c), and a Ag bipolar interface (BPI 2b) system that consists of a Ag/Nafion ionomer (H^+-form) with a Sustainion membrane (d).

We have chosen to investigate both acidic and alkaline ionomer and membrane configurations, as depicted in **Figure 4.1**, via various experimental and theoretical techniques, allowing us to inform our current physical understanding of the CO_2R MEA interfacial microenvironment and form a more definitive holistic understanding of how CO_2R MEA behavior is governed by the Ag/ionomer interface and its surroundings. The earlier work of Patru et al[154] investigated various monopolar and bipolar ionomer configurations in a Au-based MEA. Although some performance tradeoff findings between that work and our current work are similar, this present work shines more focus on the ionomer pH/ion chemistry proximal or directly adjacent to the (Ag) catalyst surface, which directly impacts a variety of macroscale and microscale metrics: intrinsic CO_2R kinetic activity, local CO_2:H_2O ratio, CO intermediate stabilization, ion-transport rates, available ECSA, as well as CO_2 crossover and CO_2 utilization/extent of homogeneous buffer reactions (depending on the charge of the membrane used).[62]

4.2 Experimental Methods

4.2.1 Membrane-electrode assembly studies

The catalyst inks and electrode substrate preparation methods were identical to those used in Chapters 2 and 3.[58] The Ag cathode ink comprised of Ag/C particles (*i.e.,* 20% Ag on Vulcan® XC-72 carbon support, Premetek®), Sustainion® XA-9 ionomer (5% in ethanol, Dioxide Materials®) or Nafion® D521 ionomer (5% in ethanol, Fuel Cell Technologies®), water (Milli-Q®, 18 mΩ), and n-propanol (Sigma-Aldrich®). The Ir anode catalyst ink comprised of IrO_2 nanoparticles (Tanaka®, SA=100), Sustainion® ionomer (at an optimal ionomer content of 11.6

wt.-%)[129], water, n-propanol, and ethanol (Sigma-Aldrich®). The Ir loadings were fixed at 1 mg_{Ir} cm^{-2}. The Ag cathode loading was set at 0.1 mg_{Ag} cm^{-2} for all experiments based on optimal findings from Chapter 3.[58] The membrane and cell assembly procedures and electrochemical testing techniques were also identical to those used in a previous study.[58] Sustainion® X37-50 RT AEMs (anion exchange membranes) or Nafion® 212 CEMs (cation exchange membranes) were used depending on the desired test. Chronopotentiometry (*i.e.,* constant current) was used to obtain polarization curves that allowed for constant flux comparisons; error bars denote multiple separate measurements with different MEAs, as well as multiple measurements within the same MEA.

4.2.2 Morphological characterization

4.2.2.1 Powder XRD (PXRD)

PXRD spectra of the Ag/C and its carbon support (Vulcan XC-72) were recorded using a MiniFlex 6G X-ray diffractometer (Rigaku) equipped with a Cu K_α radiation (λ = 1.5418 Å). A tube voltage of 40 kV and tube current of 15 mA were used. The PXRD scanning rate was 5° min^{-1} in the scan range of 2θ from 2 to 80°. The mean crystallite size of the supported nanoparticles was calculated based on the Scherrer equation (see **Equation 4.1**),

$$\tau = \frac{K\lambda}{\beta \cos\theta} \tag{4.1}$$

where τ is the mean crystallize size, K is a shape factor (0.94)[155], λ is an X-ray wavelength (1.5418 Å for the Cu K_α radiation), β is the line broadening at full width at half maximum, and θ is the Bragg angle. Deconvoluted PXRD peaks showing clear $K_{\alpha 2}$ satellite peaks were constructed to only account for the $K_{\alpha 1}$ peaks in our estimation.

4.2.2.2 Transmission Electron Microscopy (TEM/STEM-EDS)

A FEI ThemIS 60-300 (Thermo Fisher Scientific) transmission electron microscope was used to acquire TEM, STEM, and STEM-EDS data of the Ag/C and the ionomer-coated Ag/C. The microscope was operated at an accelerating voltage of 300 kV and is equipped with an image aberration corrector and a Bruker SuperX energy dispersive x-ray spectroscopy detector. A Ceta2 CMOS camera and a high-angle annular dark field detector were used for TEM and STEM imaging, respectively.

4.3 Model Development

To interprete and further explore our experimental results, we developed a complementary 1D multiphysics COMSOL® model for the CL and membrane of the CO_2 electrolyzer, as depicted in **Figure 4.2**. The model contains governing equations for mass, charge, and momentum transport (similar to previously published continuum models),[56,156] which are used to solve for potentials and species concentrations. The membrane is composed entirely of an ionomer phase with diffusion coefficients that depend on the water content. Concentration-dependent Butler-Volmer

kinetics were used to determine the rate of CO and H_2 formation and both forward and reverse reactions were considered for the (bi)carbonate reactions. Finally, the boundary conditions were chosen to reflect the experimental conditions, with a constant concentration of 1 M $CsHCO_3$ at the anode and a continuous supply of humidified CO_2 gas at the cathode. Anode kinetics and effects are not currently accounted for in this model framework.

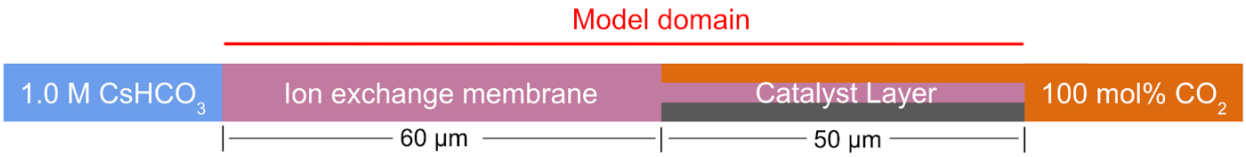

Figure 4.2. Schematic diagram of the 1D continuum model domain composed of an ion-exchange membrane (either Nafion or Sustainion) and CL.

4.1 Results & Discussion

A selection of membrane/ionomer multipolar interface combinations was investigated to probe the effect of a change in pH or chemistry near the Ag/ionomer interface. Sustainion® (a polystyrene vinylbenzyl methylimidazolium anion-conducting ionomer) was the alkaline (AEM) chemistry of choice, while Nafion® (a perfluorosulfonic acid cation-conducting ionomer) was the acidic (CEM) chemistry of choice: these two pH systems have demonstrated appreciable performance across various electrolyzer devices and reaction systems,[151] as presented in Chapter 2.

4.1.1 Ag/ionomer interface morphological characterization

By using several characterization techniques, insights into the relative volume fractions of key components in the Ag cathode CL microenvironment are obtained and used to inform our current physical understanding of this region. For instance, the amount and distribution of ionomer (relative to nanoparticle solids like support carbon or electrocatalyst) can influence the charge density, electrostatic stabilization, binding strengths, ohmic/charge transfer resistances, mass-transfer resistances, and ECSA within the CL microenvironment.[58,125,157,158]

Powder XRD data of Ag/C & Vulcan XC-72

Figure 4.3 shows the PXRD spectra of the Ag/C and Vulcan XC-72 carbon support using the Ag/C catalyst powders. The Ag/C spectrum exhibits pronounced four characteristics peaks, which correspond to (111), (200), (220), and (311) reflections based on the reference crystallographic data for silver-3C (face-centered cubic, *fcc*). The broad PXRD peak (at 2θ of ~25°) is attributed to the characteristic feature of the Vulcan XC-72 carbon support, as presented in the Vulcan XC-72 pattern. We used the Scherrer equation to estimate the mean crystallite size of the supported Ag nanoparticles (NPs), which is 37.5 ± 3.3 nm.

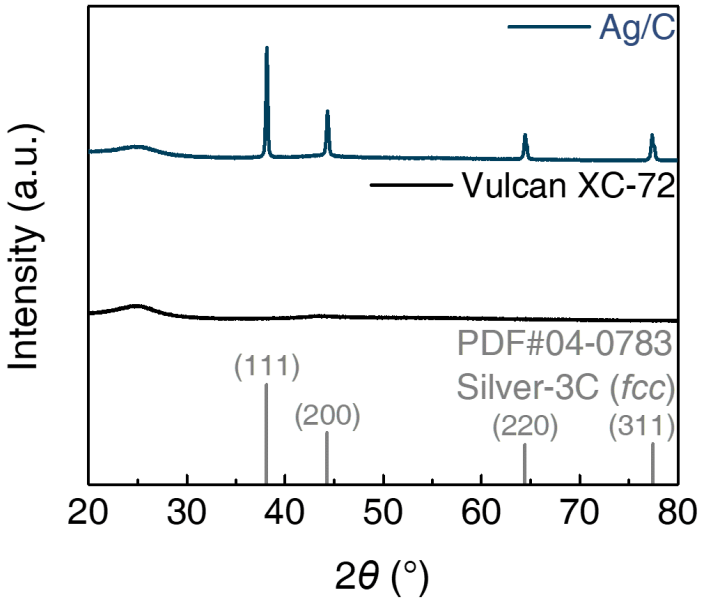

Figure 4.3. PXRD spectra of Ag/C (blue) and Vulcan XC-72 (black). The reference crystallographic data for silver-3C (*fcc*) (PDF#04-0783) is also presented.

TEM/STEM-EDS data of Ag/C and ionomer coatings

Figure 4.4 shows the TEM, STEM, and STEM-EDS data of the pristine Ag/C catalyst powders before coating the ionomer. The C *K*-edge and Ag *L*-edge maps locate both supported Ag NPs and Vulcan XC-72 carbon support. Based on the micrographs depicted, the (unsupported) Ag nanoparticle has a size of approximately 40 nm, which corroborates with the prior PXRD analysis. To compare the Ag NPs and Vulcan C supports in terms of their size, their average sizes must be measured manually, while surface area measurements (only based on TEM data) can be obtained via calculating the volume-area mean diameter (d_{VA}), from which both the specific surface area (S_{sp}) and the Ag nanoparticle metal dispersion (D) can be obtained.[159] However, to represent the ensemble behavior of the nanoparticles fully, electrochemical surface-area measurements, in addition to TEM-based surface area measurements, are recommended and are a subject of future work.

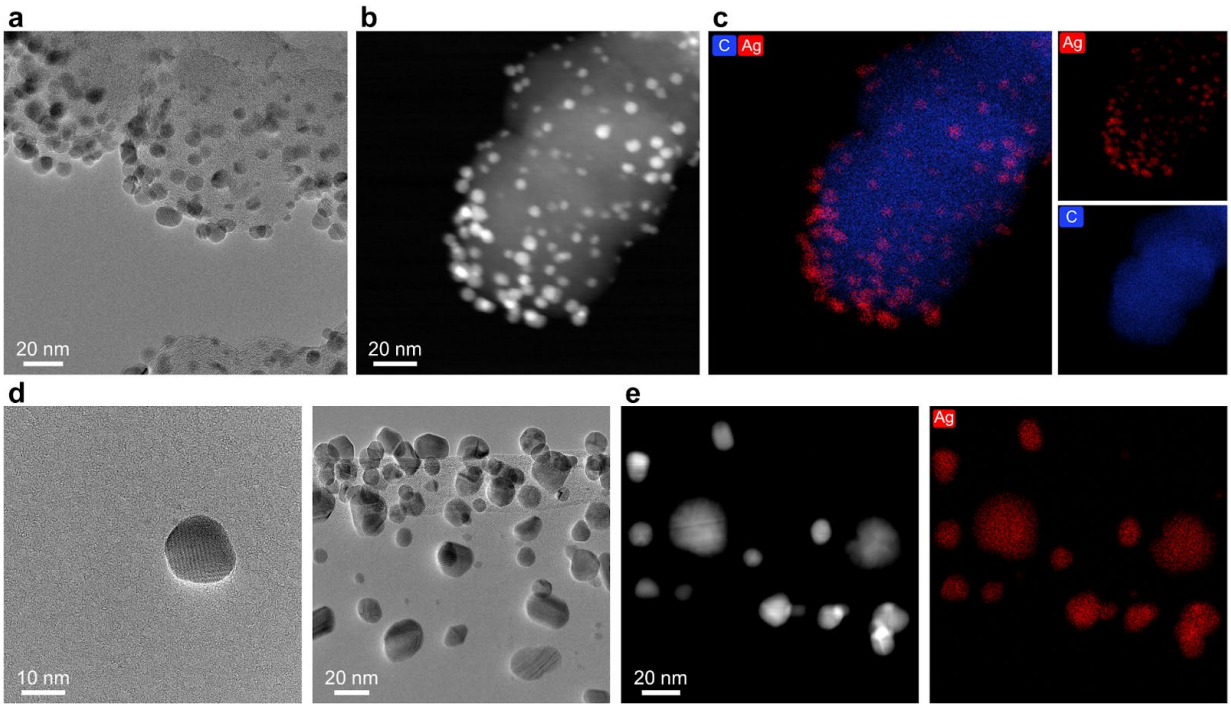

Figure 4.4. TEM (a), STEM (b), and corresponding STEM-EDS (c) images of the pristine Ag/C. For STEM-EDS elemental map data, the composite map, and its components, which are C *K*-edge and Ag *L*-edge maps are presented.

The effect of I:Cat ratio, explored in Chapter 3,[58] on the ionomer coverage and thickness on the Ag nanoparticle is visible from **Figure 4.5**. The ionomer thickness in the I:Cat = 3 system is approximately 13 nm, which corroborates well with the estimated ionomer thickness of 15 nm calculated for the I:Cat = 3 system.[58] Applying the same estimated component volume fractions for the I:Cat = 3 from that previous study[58] (*i.e.,* ionomer volume fraction = 43%, Ag catalyst volume fraction = ~1%, carbon volume fraction = ~22%), the CL porosity is expected to be ~34%, which provides a measure of how much volume is available for ion solution/electrolyte from the anode exchange solution to percolate into the cathode CL.

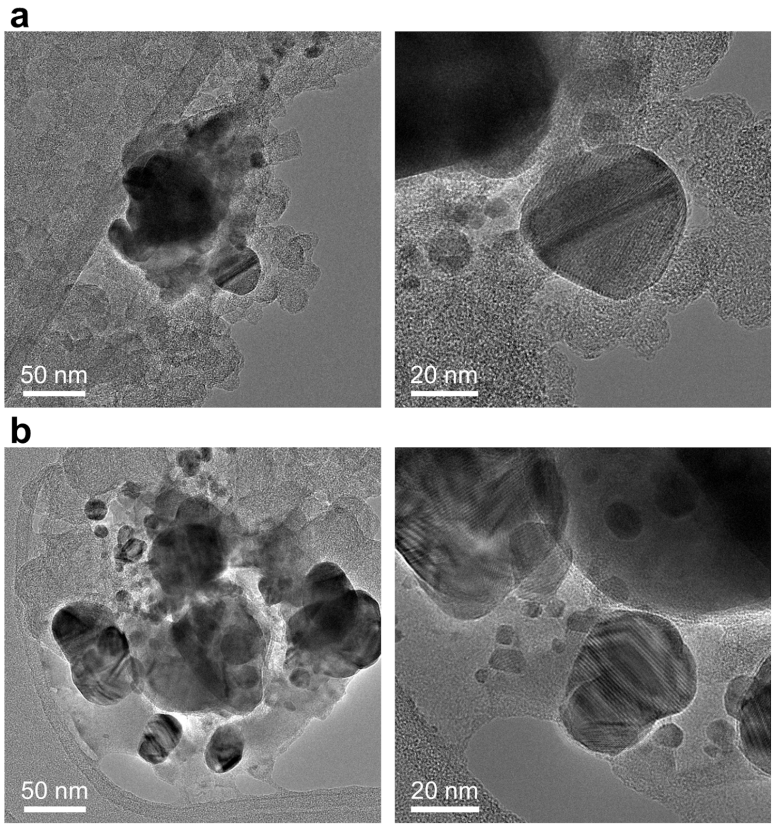

Figure 4.5. TEM images of I:Cat = 1 (a) and I:Cat = 3 (b) for a Ag/Sustainion ionomer system in a cathode catalyst ink. For the I:Cat = 3 images, the ionomer-coated region/band is visible and separate from the darker Ag nanoparticles and characteristically contrasting carbon species.

4.1.2 The impact of the Ag/ionomer interface on activity and selectivity

In using the Ag MPI (*i.e.,* fully-Sustainion) system as a baseline of comparison,[58] and maintaining the same optimal operating conditions from our previous study (1M $CsHCO_3$ Exchange-MEA, 50℃, 100 RH%, 0.1 mgAg cm^{-2}, I:Cat = 3)[58], noteworthy trends in total current density (TCD) performance for both CO_2R and water electrolysis were observed.

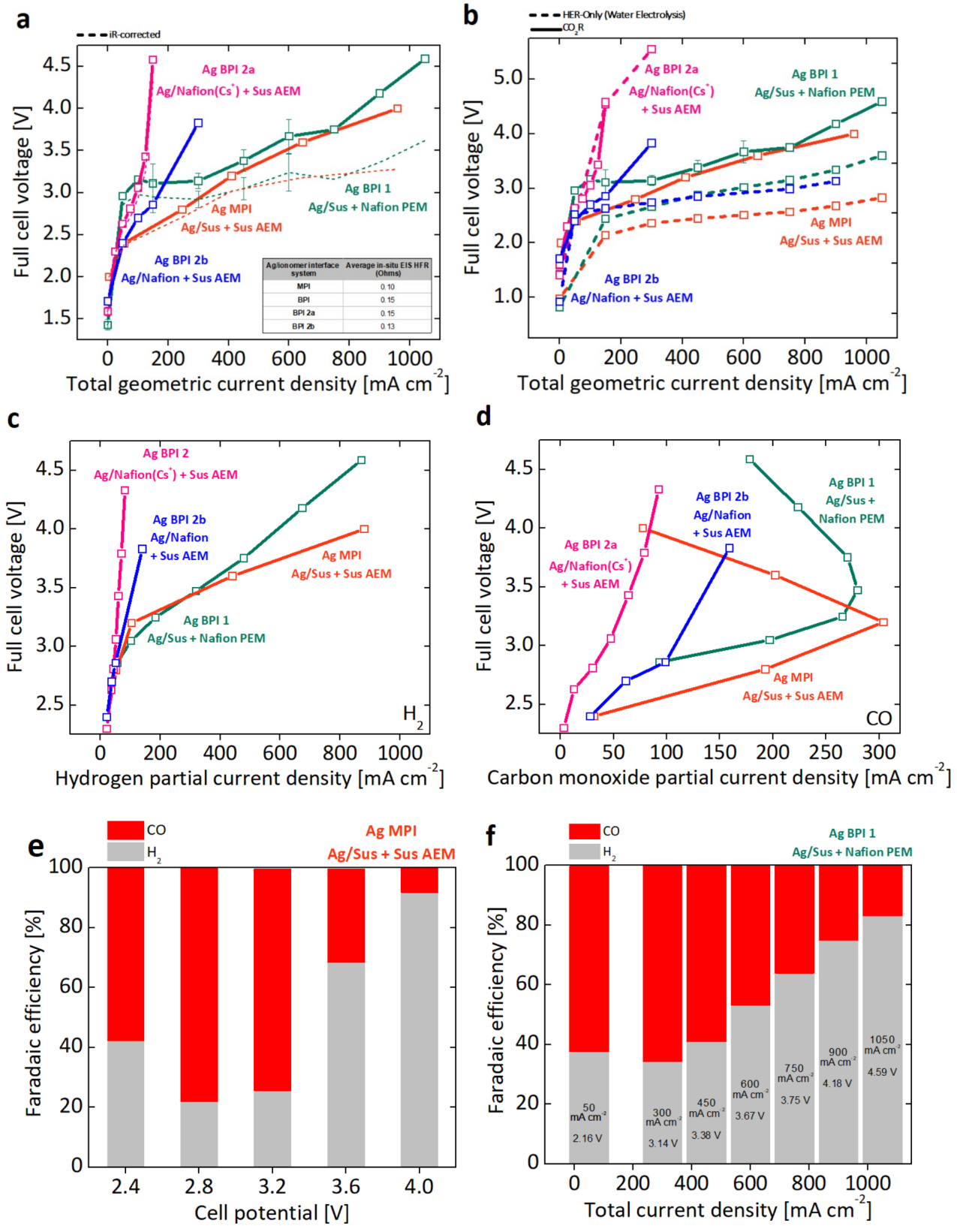
a
iR-corrected
Ag BPI 2a
Ag/Nafion(Cs+) + Sus AEM
Ag BPI 1
Ag/Sus + Nafion PEM
Ag MPI
Ag/Sus + Sus AEM
Ag BPI 2b
Ag/Nafion + Sus AEM
Ag/ionomer interface system | Average in-situ EIS HFR (Ohms)
MPI | 0.10
BPI | 0.15
BPI 2a | 0.15
BPI 2b | 0.13
Full cell voltage [V]
Total geometric current density [mA cm-2]
b
HER-Only (Water Electrolysis)
CO2R
Ag BPI 2a
Ag/Nafion(Cs+)
+ Sus AEM
Ag BPI 1
Ag/Sus + Nafion PEM
Ag MPI
Ag/Sus + Sus AEM
Ag BPI 2b
Ag/Nafion + Sus AEM
Full cell voltage [V]
Total geometric current density [mA cm-2]
c
Ag BPI 2
Ag/Nafion(Cs+) + Sus AEM
Ag BPI 2b
Ag/Nafion
+ Sus AEM
Ag MPI
Ag/Sus + Sus AEM
Ag BPI 1
Ag/Sus + Nafion PEM
H2
Full cell voltage [V]
Hydrogen partial current density [mA cm-2]
d
Ag BPI 1
Ag/Sus +
Nafion PEM
Ag BPI 2b
Ag/Nafion
+ Sus AEM
Ag BPI 2a
Ag/Nafion(Cs+)
+ Sus AEM
Ag MPI
Ag/Sus + Sus AEM
CO
Full cell voltage [V]
Carbon monoxide partial current density [mA cm-2]
e
CO
H2
Ag MPI
Ag/Sus + Sus AEM
Faradaic efficiency [%]
Cell potential [V]
f
CO
H2
Ag BPI 1
Ag/Sus + Nafion PEM
50 mA cm-2
2.16 V
300 mA cm-2
3.14 V
450 mA cm-2
3.38 V
600 mA cm-2
3.67 V
750 mA cm-2
3.75 V
900 mA cm-2
4.18 V
1050 mA cm-2
4.59 V
Faradaic efficiency [%]
Total current density [mA cm-2]

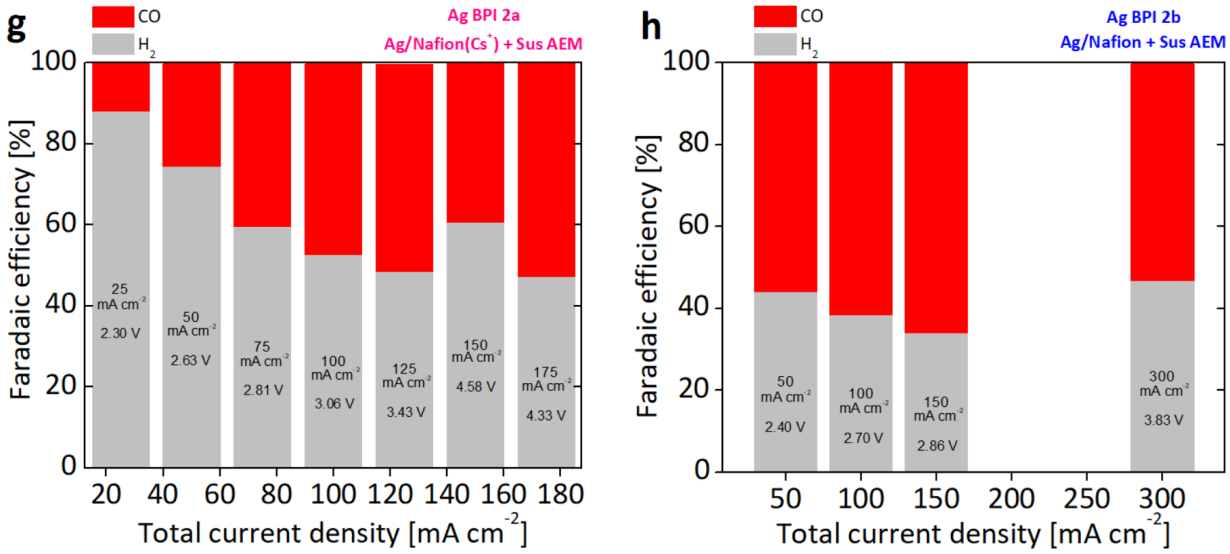

Figure 4.6. CO_2R polarization behavior with (solid lines) and without (dashed lines) *iR*-correction and an inset table depicting *in-situ* high-frequency resistance electrochemical impedance spectroscopy (EIS HFR) behavior (a) and water electrolysis behavior (b) as a function of potential for different multi-polar Ag/ionomer interfaces in a Ag cathode, Ir anode MEA. Hydrogen partial current density (c) and carbon monoxide partial current density (d) behavior as a function of potential for different multi-polar Ag/ionomer interfaces in a Ag cathode, Ir anode MEA. Faradaic efficiency as a function of potential for the different interfaces: Ag MPI (e), Ag BPI 1 (f), Ag BPI 2a (g), Ag BPI 2b (h) in a Ag cathode, Ir anode MEA. Ag MPI results and test conditions for all systems are the same as those presented in **Figure 3.2** in Chapter 3 *(used with permission from Ref.* [58]).

As shown in **Figure 4.6**, substantially different activities were observed: the Ag/Sustainion ionomer systems (*i.e.,* MPI and BPI 1) exhibited TCDs as high as 1000 mA cm^{-2}, while the Ag/Nafion ionomer systems (*i.e.,* BPI 2a and BPI 2b) exhibited markedly limited current densities at and below 300 mA cm^{-2}. Surprisingly, the TCDs of both Ag/Sustainion ionomer systems were comparable across the cell potential range despite the known order-of-magnitude differences in membrane conductivity between H^+-form Nafion CEMs[160] and HCO_3^--form Sustainion AEMs.[112,161] The BPI 1 system demonstrates essentially the same activity behavior as the MPI system for most of the potential range despite the presence of its bipolar interface, except for the sudden change in slope in the BPI 1 polarization behavior at higher cell potentials above 3.7 V. A severely limited performance of less than 200 mA cm^{-2} was observed from the Ag/Nafion ionomer system whose ionomer was directly exchanged with Cs^+ ions (*i.e.,* BPI 2a), while the Ag/Nafion ionomer system that was not directly exchanged with Cs^+ ions (*i.e.,* BPI 2b) yielded a ~100 mA cm^{-2} higher maximum current density (although due to the presence of the 1M $CsHCO_3$ exchange solution/electrolyte, some Cs^+ exchange is expected for BPI 2b). In general, the average *in-situ* EIS HFR resistances of the three BPI systems were higher than that of the MPI system, as depicted in the inset table in **Figure 4.6(a)**. The *iR*-corrected curves were also superimposed on **Figure 4.6(a),** demonstrating even more disparity between the Ag/ionomer systems: the non-ohmic and ohmic behaviors of both Ag/Nafion ionomer systems essentially overlap, while the non-ohmic and ohmic behaviors of both Ag/Sustainion ionomer systems exhibited applied cell voltage differences of approximately 0.5 V across the entire potential range. Moreover, as shown in **Figure 4.6(b)**, the overall activity trends in both CO_2R and water electrolysis persisted (*i.e.,* MPI >>> BPI 2a),

however, the water electrolysis performance only matched the CO_2R performance in the case of the BPI 2a system. This observation is especially true for the two Ag/Sustainion ionomer systems, which had comparable activity when conducting CO_2R but not when conducting water electrolysis.

A number of these observed activity trends could be attributed to certain physical phenomena occurring in the cathode CL microenvironment. The similar *iR*-corrected trends of the two Ag/Sustainion ionomer systems (*i.e.,* MPI and BPI 1) signifies comparable cathodic overpotentials, despite the presence of a prominent bipolar interface in BPI 1. This stands to reason since the same cathode ionomer (*i.e.,* Sustainion) is present in both configurations, thus any observed difference in activity (or selectivity) behavior between the two systems is directly a function of a difference in their local conditions, specifically local CO_2 concentrations. In particular, the fact that the overall activity trends (*i.e.,* MPI >>> BPI 2a) were observed for different cathode reactions, CO_2R and water electrolysis, also signifies that the cathode CL interfacial microenvironment is the primary driving force for MEA activity. However, some of the activity trends did not translate across the two reaction systems: (1) the activities of the MPI and BPI 1 systems were more disparate and (2) the activities of the BPI 1 and BPI 2b systems were more comparable to each other during water electrolysis unlike during CO_2R. These differences could also be attributed to local CO_2 concentrations being a key determining factor of activity behavior across the fabricated interfaces.

In examining the selectivity effects of the various Ag/ionomer interfaces, current notions about what chemical environment is required for optimal CO_2R selectivity (*i.e.,* a high pH and high $[CO_2]$:$[H_2O]$ ratio)[62] can be duly assessed. As shown in **Figure 4.6(c) and (d)**, the CO and H_2 partial current density trends between the Ag/Sustainion ionomer systems (*i.e.,* MPI and BPI 1) and the Ag/Nafion ionomer systems (*i.e.,* BPI 2a and BPI 2b) again show notable disparity. Very high CO partial current densities of ~300 mA cm^{-2} were observed in the MPI and BPI 1 systems, while about less than half of this value was obtained in the BPI 2a and BPI 2b systems. Moreover, the partial current densities of the MPI and BPI 1 systems were comparable and demonstrated an interesting dynamic at ~3.4 V, where a peculiar shift in the maximum COER production is observed between the two systems. This shift dynamic is also reflected in the faradaic efficiencies (FEs) of the two systems, as shown in **Figure 4.6(e) and (f)**; the MPI system attained a higher maximum CO FE of 78% compared to the lower 65% attained by the BPI 1 system across the potential range, albeit at a 10% higher overpotential. Interestingly, despite the large difference in CO partial current densities, the maximum CO FE of 65% of the non-exchanged BPI 2b system (shown in in **Figure 4.6(h)**) was comparable to that of the BPI 1 system despite having inverted membrane/ionomer chemistries (*i.e.,* Nafion ionomer with Sustainion AEM vs. Sustainion ionomer with Nafion CEM). On the other hand, the Cs^+-exchanged BPI 2a system that was expected to make gains in CO selectivity due to the more proximal presence of Cs^+ cations[96,97] in the cathode ionomer exhibited the poorest CO_2R selectivity (shown in in **Figure 4.6(g)**) of all four configurations, probably due to the way in which Cs^+ ions influence water uptake and inhibit other ion transport in the ionomer.

These selectivity behaviors could be explained by a confluence of local pH effects. For the Ag/Sustainion ionomer systems (*i.e.,* MPI and BPI 1), it is expected that, as the anion concentration in the Sustainion ionomer increases, Donnan exclusion at the Nafion membrane/Sustainion ionomer interface is overcome, and OH^-, Cs^+, and (bi)carbonate ions from the cathode reaction and anion exchange solution are transported across the membrane. These complex phenomena

could not be deconvoluted empirically and thus are treated more in-depth with the aid of a continuum model. In addition, the much higher COER production (*i.e.,* CO partial current densities) observed for the two Ag/Sustainion ionomer systems (*i.e.,* MPI and BPI 1) compared to the two Ag/Nafion ionomer systems (*i.e.,* BPI 2a and BPI 2b) could be partly explained by the differences in CO_2 solubility of the ionomers: Sustainion is known to have a 20-fold higher CO_2 solubility than water due to its imidazolium groups, which have a high CO_2 affinity,[162] while Nafion is known to have a CO_2 solubility comparable to that of water.[163] The poor TCD and selectivity performance of the Cs^+-exchanged Nafion system (BPI 2a) vs. the unexchanged Nafion system (BPI 2b) stems from both significant charge-blocking from the locally-fixed Cs^+ ions and also from the fact that the Cs^+-exchanged ionomer has lower water content, hindering its ability to transport protons: this detrimental impact of the localized Cs^+ ions in the cathode ionomer is corroborated by more in-depth interfacial capacitance and resistance studies covered in a following subsection. The selectivity switch in CO partial current density between the MPI to BPI 1 systems at around 3.4 V (with an overpotential difference of ~300 mV) is an interesting phenomenon. Considering the bipolar interfaces of Nafion and Sustainion being used in the BPI 1, the Sustainion ionomer and Nafion CEM configuration leads to higher CO selectivity (because of the trapping of the OH^- ions and the resulting high pH),[62,151] while the low ohmic resistance of the Nafion membrane allows for a comparable TCD despite the BPI interface created (the Nafion also mitigates bicarbonate crossover despite its generation). However, the fact that the TCDs (and CO partial current densities) of both configurations are nearly identical may mean that the pH environment near the Ag is effectively the same: wherein there is a high pH layer/band of generated OH^- ions that is comparable between both the MPI and BPI 1 systems. Also, despite the presence of the Nafion membrane, the TCD and EIS HFR properties of the BPI 1 system were still comparable to the full Sustainion MPI system, potentially indicating that the ohmic resistance stemming from the bipolar interface created outweighs the ohmic advantage caused of the presence of the Nafion membrane. The trends in CO partial current densities between the MPI and BPI 1 systems likely occur as a result of the balance between CO generation, high pH, and CO_2 parasitic conversion,[164] and this may be impacted by the volume/thickness of ionomer close to the Ag surface.

To aid in the interpretation of the complex CO_2R activity and selectivity experimental results described above, a multiphysics continuum model was developed. Using the model, an applied voltage-breakdown analysis[165] was performed on the BPI 1 system as shown in **Figure 4.7**. The modeled overpotentials exhibited behavior that is characteristic of other CO_2 electrolyzer polarization curves.[56] At lower current densities (i < 100 mA cm^{-2}), the kinetic overpotential associated with H^+ reduction or HER dominates (see **Equations 2.1. and 2.5**), while at higher current densities (300 mA cm^{-2} < i < 600 mA cm^{-2}), the kinetic and mass-transfer overpotentials for CO_2 reduction become significant and increase to > 50% of the total overpotential. These CO_2 reduction overpotentials decrease beyond the peak modeled CO current density (shown at ~450 mA cm^{-2} in **Figure 4.7**) as water reduction/HER activity increases. The overpotential associated with water reduction makes up almost all of the cathodic overpotential at i > 1000 mA cm^{-2}. These results highlight a dominance in HER selectivity at higher overpotentials, which was shown in the experimental results in **Figure 4.6(c)**; the higher presence of water in the BPI at higher current densities helps to explain its comparable performance with the MPI system, despite its bipolar interface. Thus, reducing water content in the cathode for the BPI 1 system at high current densities could be beneficial for reducing overpotentials.

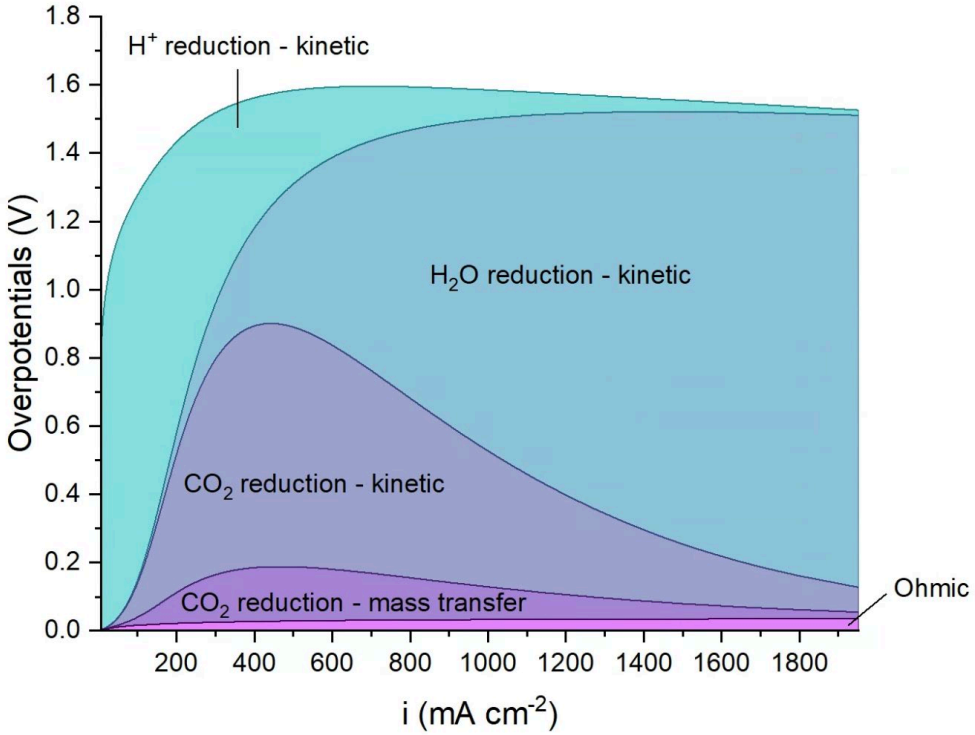

Figure 4.7. Cathodic applied-voltage breakdown for the Ag BPI 1 system as a function of current density.

In addition, the modeled concentration of CO_2 in the CL (shown in **Figure 4.8(a))** decreases as the current density is increased from 200 to 800 mA cm^{-2}. This decrease in CO_2 concentration is a result of electrochemical CO_2 reduction and acid-base reactions that form (bi)carbonates as shown in **Figure 4.8(b) and (c)**. The (bi)carbonates increase as the current density increases because of an increased rate of OH^- formation in the CL. Our experiments showed that the BPI 1 system effectively decreased the flux of these (bi)carbonates from the cathode to anode during electrolysis. Interestingly, the model shows that the transference number for CO_3^{2-} (*i.e.,* the fraction of the ionic current density associated with CO_3^{2-} transport) is close to 1 in the membrane and CL at steady-state, as shown in **Figure 4.8(d)**. As a result, future work will focus on developing a dynamic full cell model that is capable of investigating anode-specific phenomena and accurately predicting the carbon crossover during electrolysis.

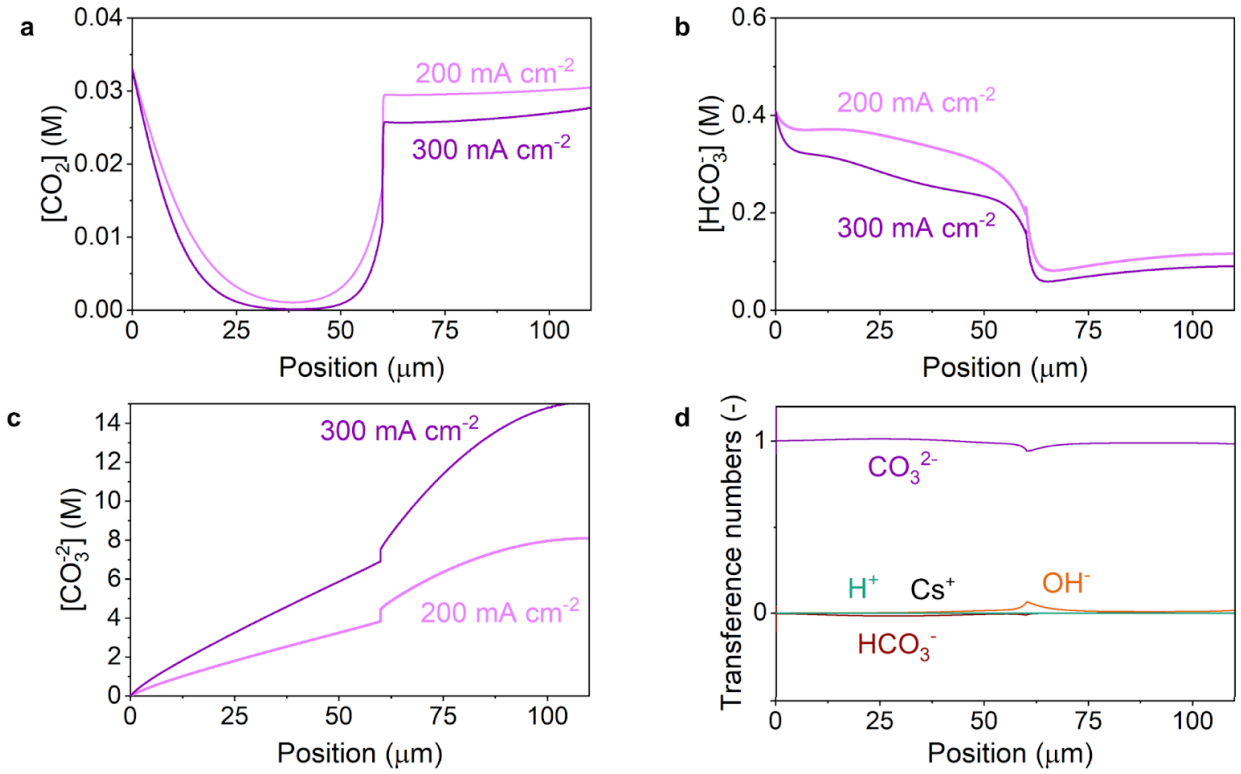

Figure 4.8. Modeled concentration profiles for the Ag BPI 1 system. Concentration profiles of (a) CO_2 (b) HCO_3^- and (c) CO_3^{2-} as a function of position in the membrane (position = 0-60 μm) and catalyst layer (position = 60-110 μm) for total current densities of 200 and 300 mA cm^{-2}. (d) Transference numbers for each ion at a total current density of 400 mA cm^{-2}.

As shown in **Figure 4.9**, the model was used to simulate the experimental CO partial current densities by implementing ion-exchange capacities corresponding to Nafion (-1 mmol g^{-1}) for the BPI 1 system and Sustainion (+1.2 mmol g^{-1}) for the MPI system. The model results show moderate agreement with the experimental data collected with the BPI 1 and MPI systems. In particular, the model corroborates the experimental observations showing that the peak CO partial current density for the MPI system occurs at a lower total current density than the BPI 1 system. We suspected that these differences in CO formation were linked to ion transport in the membrane, and therefore, we examined the modeled CO_2 and ion concentration profiles for the MPI and BPI 1 systems. The fixed negative charges in the Nafion membrane give rise to a Donnan exclusion effect that elevated the OH^- concentration in the BPI I CL relative to the MPI system. This elevated OH^- concentration resulted in a higher pH at a fixed potential as shown in **Figure 4.9(b)**, which suppressed HER and promoted CO_2 reduction. These model results corroborate the experimental results and explain how the membrane impacts the product selectivity of the CO_2R MEA.

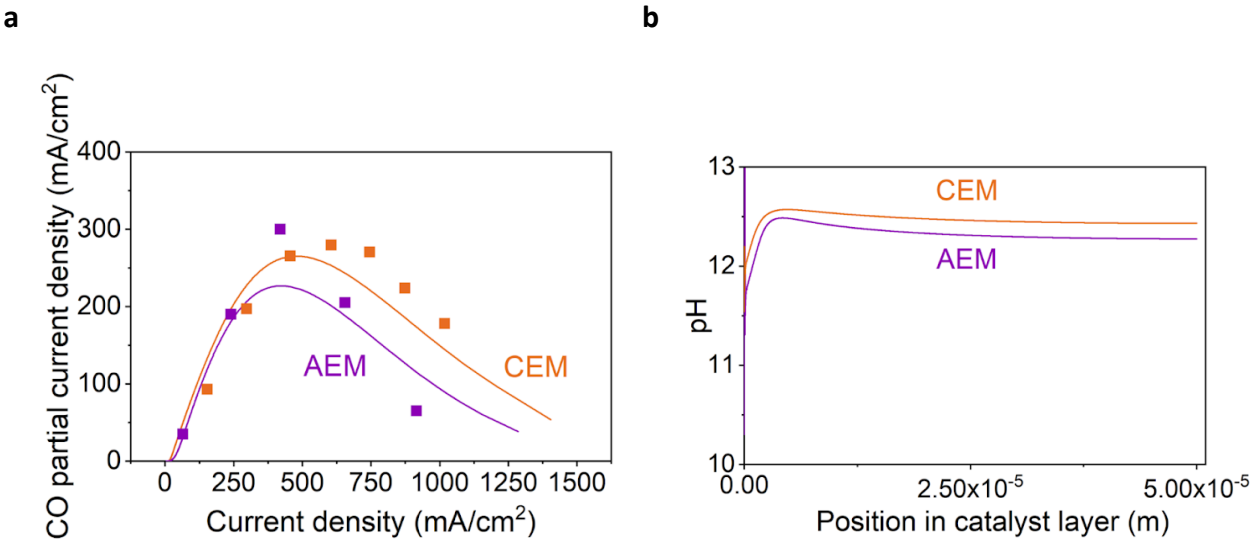

Figure 4.9. CO partial current densities for the Ag BPI 1 system (denoted CEM) and Ag MPI system (denoted AEM) as a function of the total current density. Modeling results are shown as lines and experimental data are shown as boxes (a) and modeled pH values in the catalyst layer for the AEM and CEM systems at a fixed cathode potential of 2.25 V (b).

4.1.3 The impact of the Ag/ionomer interface on CO_2 crossover and utilization

A major advantage of using multi-polar/bipolar interfaces in CO_2R device systems is their ability to mitigate CO_2 crossover that occurs via (bi)carbonate ion transport across the membrane from the cathode to the anode.[46,81,131,154]

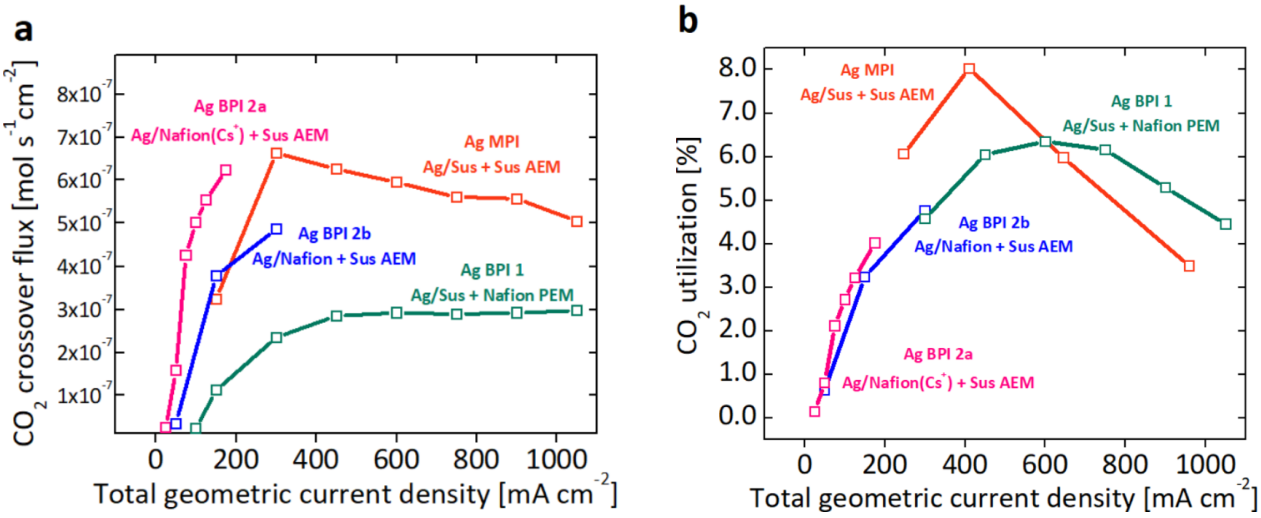

Figure 4.10. CO_2 crossover flux at the anode (a) and CO_2 utilization (b) behavior as a function of total geometric current density for different multi-polar Ag/ionomer interfaces in a Ag cathode, Ir anode MEA. Ag MPI results and test conditions for all systems are the same as those presented in **Figure 3.2** in Chapter 3 *(used with permission from Ref.* [58]).

The results of CO_2 crossover and utilization flux of monopolar vs. bipolar interfaces are shown in **Figure 4.10**. Very high CO_2 crossover fluxes were observed in the MPI system, while the lowest CO_2 crossover was exhibited by the BPI 1 system, which had a maximum flux of half that of the MPI, showing that the introduction of Nafion CEM reduces the CO_2 loss by about 50%. CO_2 utilization results were calculated based on recent modeling work.[46] The high CO_2 feed flow rates used in the systems leads to a lower fractional conversion, and hence lower CO_2 utilization. The same shifting behavior seen in the CO_2R selectivity is also observed in the CO_2 utilization trends between the MPI and BPI 1 systems. Moreover, at relevant high current densities nearing 1 A cm^{-2}, the BPI exhibited higher CO_2 utilization than the MPI system. This could be attributed to the balance between CO generation, high pH, and CO_2 parasitic conversion. It is important to note, that a half-cell/cathode steady-state continuum model that only models the cathode kinetics is sufficient to explain the observed activity and selectivity behavior, as evidenced by the good agreement between modeled and experimental behavior shown above. However, to capture fully the crossover dynamics and full applied-voltage breakdown, a full-cell (and potentially transient) model that accounts for the anode physics, specifically carbonate removal/neutralization and the unsteady-state transport of Cs^+ from the anode to the cathode, is essential and is the subject of future work.

4.1.4 The effect of Cs^+ presence on interfacial capacitance

Insights from EIS HFR sheet resistance and interfacial capacitance between the Cs^+-exchanged (BPI 2a) vs. non-exchanged (BPI 2b) Nafion ionomer systems were obtained by conducting separate tests before experimentation: the established MEA device system and operating conditions were converted into a vapor-fed Full-MEA ion pump, where HER was occurring at the cathode and HOR was occurring at the anode and no exchange solution was recirculated. An increase of ionic species at the Ag/ionomer interface in the CL due to the presence of Cs^+ ions was proposed to yield a larger interfacial capacitance than an interface without Cs^+ present. Thus, the influence of Cs^+ ions on the electrode/ionomer interface was investigated by measuring the interfacial capacitance using EIS via the method developed by where Liao et al.,[166] where the low-frequency total capacitances were extracted from spectra obtained from membranes with and without Cs^+. The method also was used to assess the consistency of the spectra with the Kramer-Kronig relations by nonlinear regression of a generic equivalent-circuit model consisting of a series of Voigt elements using a Levenberg-Marquardt algorithm implemented in Python by Watson and Orazem.[167] The regression also served to yield estimates of the values at high- and low-frequencies. Data found to be inconsistent with the Kramers-Kronig relations were discarded from the nonlinear regression.

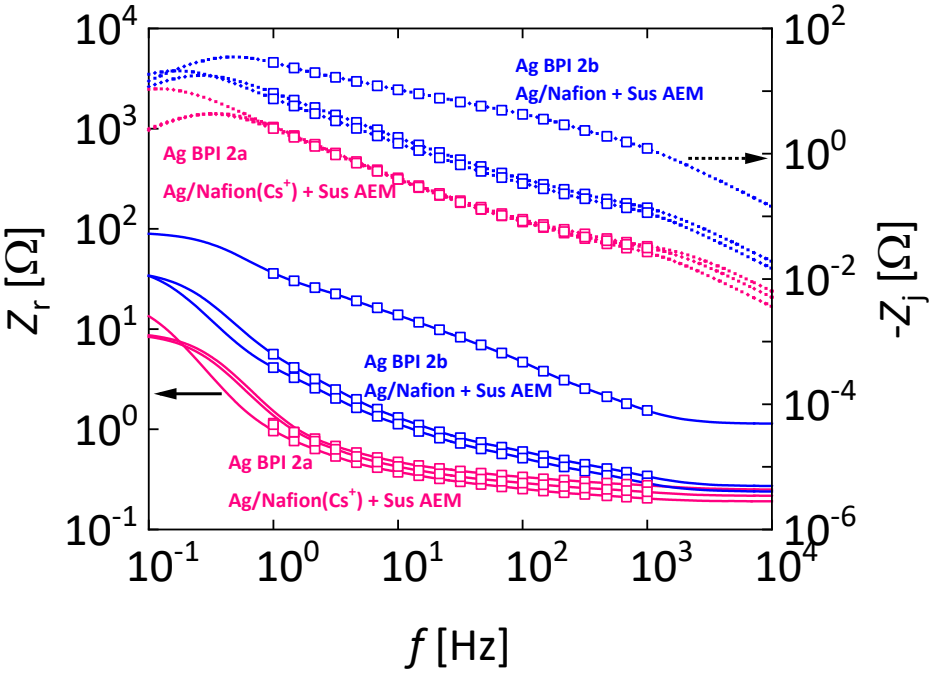

Figure 4.11. Real (solid) and imaginary (dotted) impedance from experimental measurements and generic equivalent-circuit models with the presence of Cs^+ in the membrane as a parameter. The extrapolated high-frequency resistances were mostly consistent amongst the measurements between membrane with (Ag BPI 2a) and without Cs^+ (Ag BPI 2b).

The impedance spectra and fitted model are shown in **Figure 4.11**, where the real and imaginary parts of the experimental and fitted impedances are shown as functions of frequency. The extrapolated high-frequency resistances were 2.7 ± 2.5 Ω-cm^2 (*i.e.,* 0.55 ± 0.5 Ω) and 1.1 ± 0.15 Ω-cm^2 (0.22 ± 0.03 Ω) for the membranes without Cs^+ (BPI 2b) and with Cs^+ (BPI 2a), respectively. The membrane without Cs^+ contained one measurement that had significantly larger resistance than the other values. If discarded, the high-frequency resistance of the membranes without Cs^+ (BPI 2b) was 0.254 ± 0.022 Ω, which is consistent with the EIS HFR measurements presented earlier and suggests that the discarded value is anomalous. Since low-frequency EIS measurements inform us of interfaces in the electrode/membrane region, the results indicate that the presence of Cs^+ in the exchange-Nafion ionomer cathode CL has a 2.77 greater charge number than that of just protons. These results were obtained from *in-situ* experiments, and they show that there is an interfacial charge and a specific, measurable adsorption of Cs^+ in the cathode region. However, the CO FE and partial current density of the Cs^+-exchanged Nafion was lower than that of the non-exchanged system at the same current densities, indicating that significant charge-blocking from the locally fixed cesium ions is occurring, which impacts the water uptake and hinders other H^+/OH^- ion transport.[168,169] The values of the total interfacial capacitances were assumed to be equivalent to the extrapolated low-frequency real part of the complex capacitance as calculated by **Equation 4.2**:

$$C_r(f \to 0) = \mathrm{Re}\left\{\frac{1}{j\omega Z(f \to 0)}\right\} \tag{4.2}$$

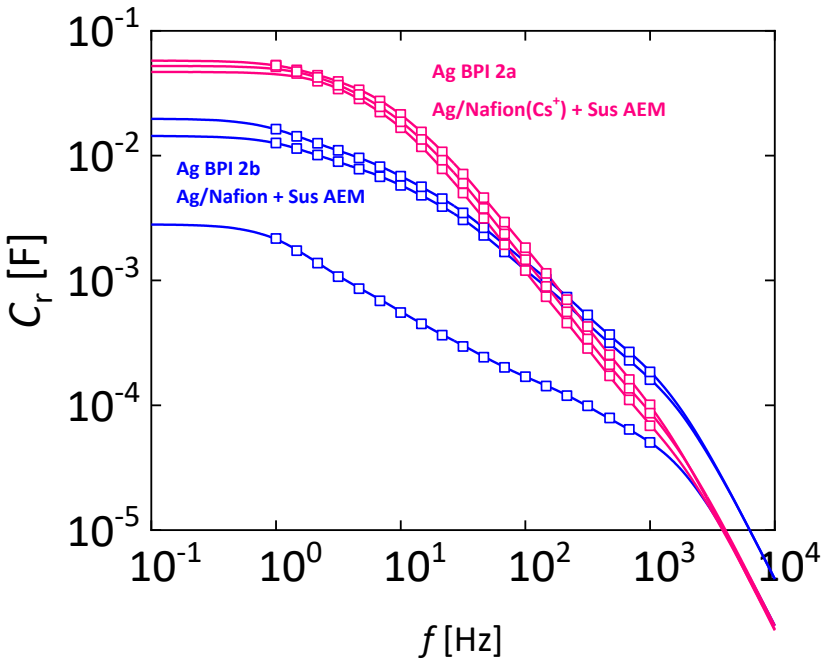

Figure 4.12. Real part of the complex capacitance of the experimental and fitted model as a function of frequency with the presence of Cs^+ in the membrane as a parameter. Membranes with Cs^+ (BPI 2a) exhibit a higher interfacial capacitance, which is consistent with higher local concentration of Cs^+ at the electrode/ionomer interface. Results were obtained from *in-situ* measurements.

The real part of the complex capacitance is shown as a function of frequency in **Figure 4.12**. The extracted interfacial capacitances were 12.3 ± 8.7 mF and 52.3 ± 5.4 mF for the membranes without Cs^+ (BPI 2b) and with Cs^+ (BPI 2a), respectively. The presence of Cs^+ resulted in larger interfacial capacitances, while not increasing the membrane bulk ohmic resistance, which suggests an enrichment of Cs^+ at the Ag/ionomer interface in comparison to the bulk Cs^+ concentration in the membrane.

4.2 Conclusions

The Ag/ionomer interface and catalyst-layer (CL) microenvironment has an outsized impact on both the microscale and macroscale performance of the CO_2R MEA. Morphological characterization of key elements of the cathode CL microenvironment (*i.e.,* ionomer, catalyst, and support carbon) was also conducted, where ionomer coverages could be visibly identified. An ionomer thickness of 13 nm for the I:Cat = 3 system matched well with the estimated ionomer thickness of 15 nm from our previous study and, extending similar estimated component volume fractions for that system, the parallel ionic pathways (one provided via ionomer and the other via electrolyte in the pore space) are estimated to be comparable in volume, as postulated in the previous work. However, depending on the ordering of the multipolar interfaces present in the cathode CL, interesting tradeoffs in activity, selectivity, and crossover can be observed. A Ag/Sustainion ionomer and Sustainion membrane monopolar interface system had very comparable activity and selectivity to a Ag/Sustainion ionomer and Nafion membrane bipolar interface system. Although the Ag monopolar interface system attains slightly higher (*i.e.,* 10%)

CO partial current densities and faradaic efficiencies and slightly lower (*i.e.,* 10%) applied overpotentials, the Ag bipolar interface system exhibited lower CO_2 crossover fluxes and higher CO_2 utilization at higher current densities. Multiphysics continuum modeling within this work corroborated these CO selectivity findings and verified that differing local conditions, specifically the local pH, ion and species concentrations, and potentials, contributed to the observed kinetic behavior of the two cathode CLs. The comparatively high performance and very low CO_2 crossover exhibited by the Ag/Sustainion ionomer and Nafion membrane bipolar interface system makes it a more efficient and the more recommended cell design for CO_2R commercialization. Current and future learnings from Nafion CEM-based systems could also potentially be applied to the improvement of such a cell. Ag/Nafion ionomer and Sustainion membrane multipolar interfaces, one with and one without a Cs^+-exchanged cathode ionomer, exhibited very poor activities, selectivities, and higher CO_2 crossovers. The HER promotion caused by the proximity of acidic Nafion to the Ag nanoparticle and the adverse impact of localized cesium ions on water uptake and ion transport in the Cs^+-exchanged Nafion ionomer cathode led to their poor performance. These findings were also confirmed via interfacial capacitance measurements and calculations.

5 A Pathway to Industrial Carbon Neutrality: Summary and Future Perspectives on CO_2 Reduction in MEA Devices

5.1 Dissertation Summary

Commercializable electrochemical CO_2 reduction devices are paramount in our concerted effort to transition our global chemical, energy, and materials industries towards carbon-neutral and decarbonized gigaton-scale operation. These devices present an inventive method for re-routing CO_2, a pervasive and damaging greenhouse gas, into carbon-neutral avenues and end uses in the medium- and long-term. Through comprehensive and systematic studies, ranging from cell experiments and characterization to mathematical and physical modeling, an understanding of the links between catalyst-layer component properties, CO_2R MEA macroscale performance, and fundamental multiphysics phenomena occurring in the cathode microenvironment was established. This effort led to the development of a membrane-electrode assembly that can convert CO_2 to value-added products (mainly CO) selectively and efficiently at industrially-relevant levels. This dissertation addressed certain knowledge gaps concerning the CO_2R MEA, whose relatively simple system design bellies a notoriously complex cathode catalyst-layer microenvironment. The overall effort included the crucial work of relating macroscale concepts, such as materials design parameters and operating conditions, to microscale, fundamental phenomena like interfacial surface area, electrochemical and homogeneous kinetics, and reactant and ion concentrations. Specifically, in this dissertation:

(1) Chapter 2 presents CO_2R MEA fabrication and experimental best practices, methodologies, and findings, such as the benchmarked performance for different AEM ionomers and membranes and the water-management effects of changing system-wide factors, including system temperature and relative humidity, that can potentially be applied to scalable CO_2R designs.

(2) Chapter 3 highlighted the use of the MEA systems engineered in Chapter 2 to build a Ag CO_2R MEA operating at moderately elevated system temperatures (50°C), high concentration exchange solutions (1.0 M $CsHCO_3$), low cathode catalyst-layer thicknesses and loadings (0.01 – 0.1 mg_{Ag} cm^{-2}), and intermediate ionomer-to-catalyst content or coverage (I:Cat = 3) that achieved tunable and high current densities (200 mA cm^{-2} to 1 A cm^{-2}) and CO/syngas selectivity (78 to 91% CO faradaic efficiencies).

(3) Building on the findings in Chapter 3, Chapter 4 explored the effects of multi-polar interfaces at the cathode catalyst layer, elucidating the inherent tradeoffs between CO_2R activity, selectivity, and CO_2 crossover and utilization, with further insights provided via multiphysics modeling, morphological characterization, and interfacial capacitance studies.

Applied research work that establishes both transferable scientific understanding and informative engineering optimization, such as the work done within this dissertation, can provide much-needed insight and guidance in the technologically-difficult path towards industrial carbon neutrality and decarbonization.

5.2 Future Perspectives

The field of CO_2 electrochemical synthesis leaves numerous areas for further exploration and in-depth investigation. Below is an outline of key topics encouraged for immediate research.

(1) ***Improving product selectivity****:* The Ag-based MEA insights and performance improvements outlined in this dissertation can be transferred to other CO_2R MEA device systems such as a Cu-based MEA, which has a much more varied product distribution and surface coverage behavior.[170–172] In particular, strategies to increase the formation of C_{2+} products (*e.g.,* ethylene, ethanol, and 1-propanol) relative to C_1 products like carbon monoxide and methane should be given special attention. Secondly, with Cu known to be the only electrocatalyst that can facilitate substantial multi-carbon selectivities[33] and with CO established as a key intermediate in the CO_2R mechanism,[34,128] the concept of tandem catalysis becomes more attractive. **Figure 5.1** depicts an example of this tandem concept, where two MEAs perform sequential reduction. A proof-of-concept has already been demonstrated in aqueous GDE systems[126,127] and a more recent tandem MEA study[85] exhibited significant improvements in C_{2+} selectivity, while also maintaining high reactivity. Lastly, in traditional aqueous CO_2R systems, it is known that maximum C_{2+} production generally occurs past a -1 V vs. RHE threshold.[164] However, it is currently unknown what the threshold cathodic overpotential (and corresponding full-cell voltage) for appreciable C_{2+} product formation is for the CO_2R MEA system. To help address this question, the development of (1) reliable, physical reference electrodes specifically for the cathode environment and (2) empirical or experimental applied-voltage-breakdown (AVB) methodologies (which could eventually be compared with theoretically-generated AVBs[165]) are insightful strategies that can be used to provide *in-situ* cathodic overpotential data for CO_2R MEAs.

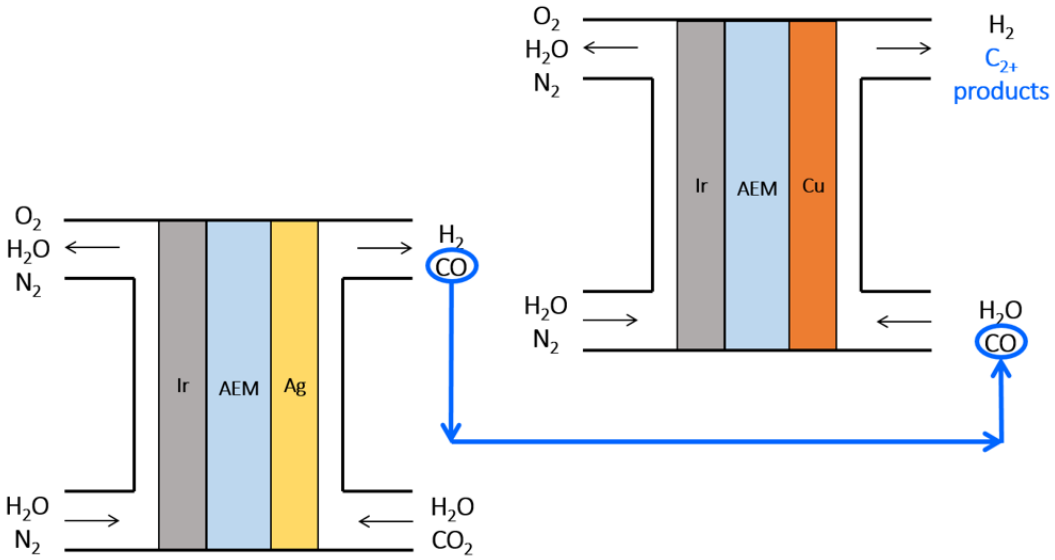

Figure 5.1. Schematic of an MEA-in-series design for tandem CO_2 reduction. The first MEA is optimized for CO_2-to-CO production, while the second MEA is optimized for CO-to-C_{2+} species production.

(2) ***Incorporating real-world feed conditions****:* Few comprehensive sensitivity studies have been conducted on the various aspects of the reactant feed inlet for CO_2R MEA systems, such as relative CO_2 and water reactant flow rates, pressures, or concentrations, CO_2 purity, inlet backpressure, feed recycle, as well as other metrics that would impact the single-pass conversion of the device. Although some learnings can be gleaned from studies done on the effect of CO_2 concentration in AEM water electrolyzers,[173] it is important to conduct targeted studies that would test the robustness and durability of CO_2R MEA systems under very low CO_2 concentrations or with high feed impurities[174] that closely mimic atmospheric or industrial effluent conditions. In addition, there is a need to explore the viability of direct air/CO_2 capture at the inlet via using membrane, ionomer, or ionic liquid CO_2 capture agents, metal-organic frameworks (MOFs) that can perform ambient reversible CO_2 adsorption, or bicarbonate electrolyzers;[156,175] such studies would inform advances towards the production of carbon-neutral or possibly carbon-negative CO_2 reduction products (provided those products never release CO_2). Furthermore, considering the continued and projected scarcity of pure freshwater sources,[176] research into using impure, non-potable water or seawater[177] as a replacement reactant, humidification, and solution agent in CO_2R MEA systems is of interest. The influence of these changes on required or optimal system temperatures, relative humidities, materials design parameters, as well as activities, surface coverages, selectivities, and fractional conversions in the MEA should also be quantified. Lastly, studies into various MEA gas-channel flow configurations, as shown in **Figure 5.2**, could help determine which mode of inlet water transport (*i.e.,* convective, diffusive) would be most beneficial for improving water management and CO_2R performance. The impact of various gas-channel designs, such as interdigitated, serpentine, and parallel patterns, has already been explored in PEM (proton exchange membrane) fuel cells[178] and it would be informative to see how such variations impact CO_2R MEA systems.

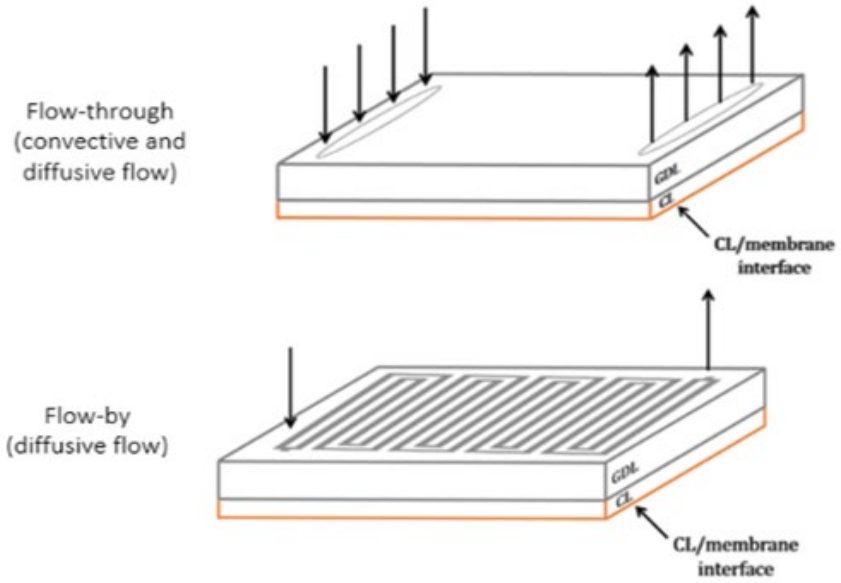

Figure 5.2. Schematic showing types of cathode feed flow configurations: flow-through and flow-by.

(3) ***Learning from model experimental systems:*** Model systems like the microelectrode could be used to probe intrinsic CO_2R activity for various catalyst/ionomer interfaces. Unlike the MEA, such systems offer solid-state measurements at better defined potentials and with lower resistances, allowing for empirical Butler-Volmer or Tafel fittings and kinetic activities to be obtained. It could also be possible to determine CO_2R-specific hydroxide/alkaline vs. proton/acidic transport parameters in these set-ups, which would give an insight into whether either kinetic or transport processes are limiting. Secondly, using a simpler model system to compare and assess proton vs. hydroxide ion mobility in membrane/ionomer systems is currently a key open question that warrants comprehensive investigation. Such a study would inform the overall design of acidic vs. alkaline GDE and MEA devices by determining whether supporting electrolyte or more precise, thoughtful catalyst-layer structures are required for alkaline systems but not for acidic systems. According to the seminal work done by McBreen et al,[179] the ECSA of a catalyst/ionomer interface was the same as that of a catalyst/electrolyte (*i.e.,* 1N H_2SO_4, 0.5 TFMSA) interface for acidic/Nafion systems, even without the ionomer being in contact with the full electrode area. They demonstrated that proton adsorption can occur on sites remote from the membrane/electrode interface, provided it is wetted with water. The concluding hypothesis was that mobile adsorbed species on metal surfaces were the main mechanism of current generation and thus source of ECSA. Assessing if this crucial ECSA finding is also true for hydroxide/alkaline systems and how the ECSAs of alkaline and acid systems compare under the same operating and materials design conditions would be highly informative in addressing the above open question pertaining to acidic vs. alkaline device designs. As shown in **Figure 5.3**, an ECSA measurement cell similar to the one used in the McBreen study[179] could be used for cyclic-voltammogram experiments conducted under different ionomer type, ion solution, relative humidity, or thermal conditions.

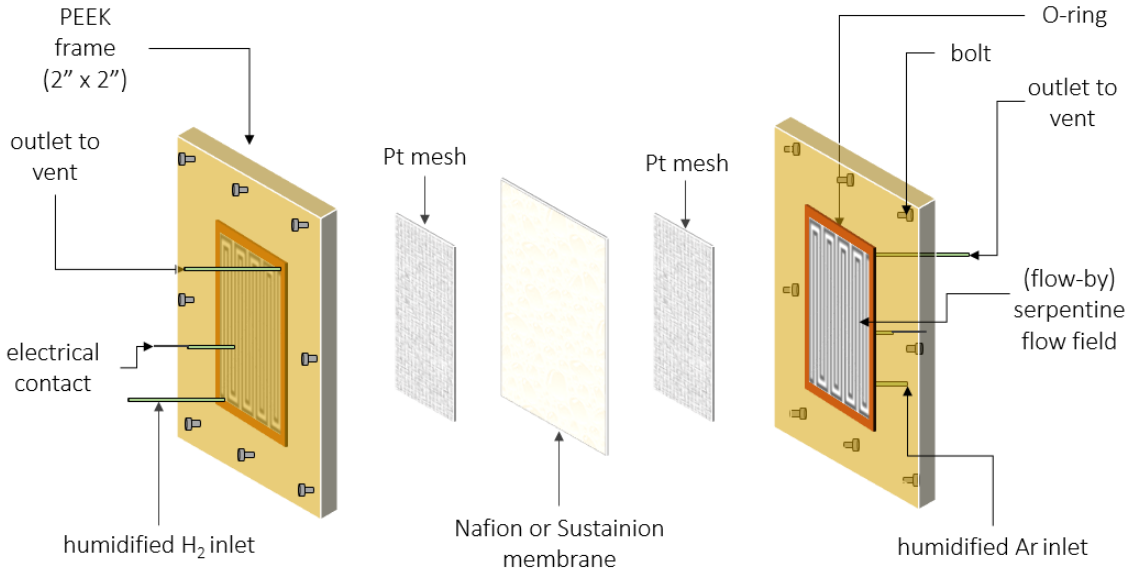

Figure 5.3. Schematic of a custom-made cell used for fundamental ECSA measurements, exploded view.

(4) ***Studying catalyst-layer inks****:* Chapters 3 and 4 of this dissertation demonstrated that the cathode catalyst layer and its components play a crucial role in CO_2R MEA performance. The genesis of this structure is the cathode catalyst ink, which can contain CO_2R catalysts ranging from Ag or Cu to Cu-free or custom-made catalysts.[180] Determining how the ink components themselves, the preparation process, and the deposition process dictate the physical nature and morphology of the cathode catalyst layer, as well as subsequent device performance, is of interest. These structure-property relationship studies have been conducted extensively for fuel-cell inks[105,107,108,125,158,181–183] but few have been done for CO_2R electrolyzer inks.[73] Some areas worth exploring on this front include determining: (1) the impact of the ionomer:solvent ratio on porosity and CO_2R MEA voltage response and selectivity, (2) the effect of support carbon content on CO_2R activity and selectivity, specifically if the presence of support carbon (a potential HER-promoting catalyst surface) could lead to more hydrogenated/less C-C coupled products that negatively impact C_{2+} selectivity or conversely allow for the degree of hydrogenation of CO_2R products to be intelligently modulated, and (3) how the ionomer coverage and its relative adsorption on catalyst particles vs. support carbon particles influence selectivity. Characterization techniques like dynamic or acoustic light scattering could be paired with ionomer thin film or cell studies to explore and elucidate these behaviors. Lastly, the impact of: (1) particle/particle, particle/ionomer, and particle/solvent interactions, particle-size distributions, and the degree of aggregation, (2) various MEA deposition or fabrication techniques separate from layer-by-layer spray coating (*e.g.,* electrospinning, doctor blading, slot die-coating *etc.*), and (3) different deposition substrates (*i.e.,* GDLs, PTLs, or CCMs) on the cathode catalyst-layer structure and subsequent device performance should be quantified.

(5) ***Expanding single-cell studies****:* Although hardly covered in the literature, anode catalysis can be important in its ability to affect the overpotential distribution throughout the entire CO_2R MEA device. Useful efforts in this area may involve taking away some focus from the use of scarce, precious metal catalysts like iridium for OER and channeling it to the study of more earth-abundant, non-precious catalysts like nickel.[184,185] Understanding how these other metal catalysts and their loading influence local kinetics and transport at the anode catalyst layer and the whole cell performance would be key in improving the overall device efficiency and cost via techno-economic analyses.[57,122,186–188] In addition, exploring other MEA anode reactions (aside from OER and HOR) that have more industrial relevance such as glycerol oxidation,[189–191] methane-to-methanol partial oxidation,[192] or organic oxidation reactions[57] could prove useful. In addition, other reductive reaction systems such as electrochemical ammonia synthesis via nitrogen reduction, which has garnered much attention in recent years,[193–197] could benefit from more practical, efficient MEA test-beds. Photo-electrochemical CO_2 conversion is another emerging subarea that warrants increased focus for further single-cell performance improvements.[198–206] Secondly, in the effort to scale-up the CO_2R MEA system for industrial implementation, it is important to explore the impact of increasing the MEA single-cell size, which has numerous implications surrounding heat management/cooling, higher throughput operation, increased cell component and material costs, as well as multiphysics complexity since larger cells would exhibit higher gradients and heterogeneities. Thirdly, there is a heightened need for long-term durability, stability, and failure mechanism

studies in these MEA devices, which would inform their life cycle assessments and lifetime cost analyses. Relatedly, the challenge of crossover and carbonate formation as well as detrimental salt formation in single-step electrolyzers is an ongoing issue, where the use of bipolar (or bipolar-like[151]) membrane systems,[131,207] tandem/CO reduction systems,[94,172,208–211] could serve to mitigate losses.[85,122] Quantifying recoverable and irrecoverable decay mechanisms and procedures during these instances of species loss is needed. Lastly, certain emerging, non-physics-based computational tools and techniques, such as Bayesian optimization,[212–214] machine learning,[215,216] or related data-centric/mathematical optimization strategies,[217] could be implemented to accelerate experimental and materials discovery,[218–220] tease out elusive kinetic or mass-transport parameters,[221] and subsequently optimize the CO_2R MEA single-cell system beyond what is currently possible.

6 References

(1) *Fifth Assessment Report — IPCC*. https://www.ipcc.ch/assessment-report/ar5/ (accessed 2022-06-28).

(2) *Climate change: a threat to human wellbeing and health of the planet. Taking action now can secure our future — IPCC*. https://www.ipcc.ch/2022/02/28/pr-wgii-ar6/ (accessed 2022-06-28).

(3) Broecker, W. S. Climatic Change: Are We on the Brink of a Pronounced Global Warming? *Science (1979)* **1975**, *189* (4201), 460–463. https://doi.org/10.1126/SCIENCE.189.4201.460.

(4) Mann, M. E.; Bradley, R. S.; Hughes, M. K. Northern Hemisphere Temperatures During the Past Millennium: Inferences, Uncertainties, and Limitations. **1999**.

(5) *Extreme Weather and Climate Change - Center for Climate and Energy SolutionsCenter for Climate and Energy Solutions*. https://www.c2es.org/content/extreme-weather-and-climate-change/ (accessed 2022-06-28).

(6) *Drought and Climate Change - Center for Climate and Energy SolutionsCenter for Climate and Energy Solutions*. https://www.c2es.org/content/drought-and-climate-change/ (accessed 2022-06-28).

(7) Dahl, K.; Licker, R.; Abatzoglou, J. T.; Declet-Barreto, J. Increased Frequency of and Population Exposure to Extreme Heat Index Days in the United States during the 21st Century. *Environmental Research Communications* **2019**, *1* (7). https://doi.org/10.1088/2515-7620/AB27CF.

(8) *Heat Waves and Climate Change - Center for Climate and Energy SolutionsCenter for Climate and Energy Solutions*. https://www.c2es.org/content/heat-waves-and-climate-change/ (accessed 2022-06-28).

(9) McElwee, P. Climate Change and Biodiversity Loss Two Sides of the Same Coin. *Current History* **2021**, *120* (829), 295–300. https://doi.org/10.1525/CURH.2021.120.829.295.

(10) *Climate Change and Biodiversity Loss | Current History | University of California Press*. https://online.ucpress.edu/currenthistory/article/120/829/295/118794/Climate-Change-and-Biodiversity-LossTwo-Sides-of (accessed 2022-06-28).

(11) Javeline, D.; Hellmann, J. J.; McLachlan, J. S.; Sax, D. F.; Schwartz, M. W.; Cornejo, R. C. Expert Opinion on Extinction Risk and Climate Change Adaptation for Biodiversity. *Elementa* **2015**, *3*. https://doi.org/10.12952/JOURNAL.ELEMENTA.000057/112719/EXPERT-OPINION-ON-EXTINCTION-RISK-AND-CLIMATE.

(12) Rounsevell, M. D. A.; Harfoot, M.; Harrison, P. A.; Newbold, T.; Gregory, R. D.; Mace, G. M. A Biodiversity Target Based on Species Extinctions. *Science (1979)* **2020**, *368* (6496), 1193–1195. https://doi.org/10.1126/SCIENCE.ABA6592.

(13) *Ocean acidification | National Oceanic and Atmospheric Administration*. https://www.noaa.gov/education/resource-collections/ocean-coasts/ocean-acidification (accessed 2022-06-28).

(14) *The Anatomy of Glacial Ice Loss – Climate Change: Vital Signs of the Planet*. https://climate.nasa.gov/news/3038/the-anatomy-of-glacial-ice-loss/ (accessed 2022-06-28).

(15) Domingues, R.; Goni, G.; Baringer, M.; Volkov, D. What Caused the Accelerated Sea Level Changes Along the U.S. East Coast During 2010–2015? *Geophysical Research Letters* **2018**, *45* (24), 13,367-13,376. https://doi.org/10.1029/2018GL081183.

(16) Church, J. A.; White, N. J. Sea-Level Rise from the Late 19th to the Early 21st Century. *Surveys in Geophysics* **2011**, *32* (4–5), 585–602. https://doi.org/10.1007/S10712-011-9119-1.

(17) *Understanding the Connections Between Climate Change and Human Health | US EPA*. https://www.epa.gov/climate-indicators/understanding-connections-between-climate-change-and-human-health (accessed 2022-06-28).

(18) Newsom, E. R.; Fassbender, A. J.; Maloney, A. E.; Bushinsky, S. M. Increasing the Usability of Climate Science in Political Decision-Making. *Elementa* **2016**, *4*. https://doi.org/10.12952/JOURNAL.ELEMENTA.000127/112876/INCREASING-THE-USABILITY-OF-CLIMATE-SCIENCE-IN.

(19) Myers, T. C. Understanding Climate Change as an Existential Threat: Confronting Climate Denial as a Challenge to Climate Ethics. *De Ethica* **2014**, *1* (1), 53–70. https://doi.org/10.3384/DE-ETHICA.2001-8819.141153.

(20) *Climate Change 2022: Impacts, Adaptation and Vulnerability | Climate Change 2022: Impacts, Adaptation and Vulnerability*. https://www.ipcc.ch/report/ar6/wg2/ (accessed 2022-06-28).

(21) *Geoengineering the Climate System - American Meteorological Society*. https://www.ametsoc.org/index.cfm/ams/about-ams/ams-statements/statements-of-the-ams-in-force/geoengineering-the-climate-system/ (accessed 2022-06-28).

(22) *Oxford Geoengineering Programme // What is Geoengineering?*. http://www.geoengineering.ox.ac.uk/www.geoengineering.ox.ac.uk/what-is-geoengineering/what-is-geoengineering/ (accessed 2022-06-28).

(23) *Storing CO2 underground can curb carbon emissions, but is it safe? | Research and Innovation*. https://ec.europa.eu/research-and-innovation/en/horizon-magazine/storing-co2-underground-can-curb-carbon-emissions-it-safe (accessed 2022-06-28).

(24) *CO2 Reduction | Center for Interface Science and Catalysis*. https://suncat.stanford.edu/research/co2-reduction (accessed 2022-06-18).

(25) Bushuyev, O. S.; de Luna, P.; Dinh, C. T.; Tao, L.; Saur, G.; van de Lagemaat, J.; Kelley, S. O.; Sargent, E. H. What Should We Make with CO2 and How Can We Make It? *Joule*. Cell Press May 16, 2018, pp 825–832. https://doi.org/10.1016/j.joule.2017.09.003.

(26) Loveless, B. T.; Buda, C.; Neurock, M.; Iglesia, E. CO Chemisorption and Dissociation at High Coverages during CO Hydrogenation on Ru Catalysts. *J Am Chem Soc* **2013**, *135* (16), 6107–6121. https://doi.org/10.1021/JA311848E/ASSET/IMAGES/MEDIUM/JA-2012-11848E_0018.GIF.

(27) Xu, M.; Iglesia, E. Carbon–Carbon Bond Formation Pathways in CO Hydrogenation to Higher Alcohols. *Journal of Catalysis* **1999**, *188* (1), 125–131. https://doi.org/10.1006/JCAT.1999.2650.

(28) Lee, M. Y.; Park, K. T.; Lee, W.; Lim, H.; Kwon, Y.; Kang, S. Current Achievements and the Future Direction of Electrochemical CO2 Reduction: A Short Review. *https://doi.org/10.1080/10643389.2019.1631991* **2019**, *50* (8), 769–815. https://doi.org/10.1080/10643389.2019.1631991.

(29) Hori Yoshio; Kikuchi Katsuhei; Murata Akira; Suzuki Shin. PRODUCTION OF METHANE AND ETHYLENE IN ELECTROCHEMICAL REDUCTION OF CARBON DIOXIDE AT COPPER ELECTRODE IN AQUEOUS HYDROGENCARBONATE SOLUTION. *http://dx.doi.org/10.1246/cl.1986.897* **2006**, *15* (6), 897–898. https://doi.org/10.1246/CL.1986.897.

(30) Hori, Y.; Murata, A.; Takahashi, R. Formation of Hydrocarbons in the Electrochemical Reduction of Carbon Dioxide at a Copper Electrode in Aqueous Solution. *Journal of the Chemical Society, Faraday Transactions 1: Physical Chemistry in Condensed Phases* **1989**, *85* (8), 2309–2326. https://doi.org/10.1039/F19898502309.

(31) Hori, Y.; Kikuchi, K.; Suzuki, S. PRODUCTION OF CO AND CH 4 IN ELECTROCHEMICAL REDUCTION OF CO 2 AT METAL ELECTRODES IN AQUEOUS HYDROGENCARBONATE SOLUTION . *Chemistry Letters* **1985**, *14* (11), 1695–1698. https://doi.org/10.1246/CL.1985.1695.

(32) Hori, Y.; Wakebe, H.; Tsukamoto, T.; Koga, O. Electrocatalytic Process of CO Selectivity in Electrochemical Reduction of CO2 at Metal Electrodes in Aqueous Media. *Electrochimica Acta* **1994**, *39* (11–12), 1833–1839. https://doi.org/10.1016/0013-4686(94)85172-7.

(33) Hori, Y. Electrochemical CO2 Reduction on Metal Electrodes. *Modern Aspects of Electrochemistry* **2008**, 89–189. https://doi.org/10.1007/978-0-387-49489-0_3.

(34) Nitopi, S. A.; Bertheussen, E.; Scott, S. B.; Liu, X.; Albert, K.; Horch, S.; Seger, B.; Stephens, I. E. L.; Chan, K.; Nørskov, J. K.; Jaramillo, T. F.; Chorkendorff, I. Progress and Perspectives of Electrochemical CO 2 Reduction on Copper in Aqueous Electrolyte. *Chemical Reviews* **2018**. https://doi.org/10.1021/ACS.CHEMREV.8B00705.

(35) Xu, Y.; Isom, L.; Hanna, M. A. Adding Value to Carbon Dioxide from Ethanol Fermentations. *Bioresour Technol* **2010**, *101* (10), 3311–3319. https://doi.org/10.1016/J.BIORTECH.2010.01.006.

(36) Monteiro, J.; Roussanaly, S. CCUS Scenarios for the Cement Industry: Is CO2 Utilization Feasible? *Journal of CO2 Utilization* **2022**, *61*, 102015. https://doi.org/10.1016/J.JCOU.2022.102015.

(37) Whipple, D. T.; Kenis, P. J. A. Prospects of CO2 Utilization via Direct Heterogeneous Electrochemical Reduction. *Journal of Physical Chemistry Letters* **2010**. https://doi.org/10.1021/jz1012627.

(38) Chorendorff, I.; Niemantsverdriet, J. W. Concepts in Modern Catalysis and Kinetics. *Adsorption Journal of The International Adsorption Society* **2003**. https://doi.org/10.1002/anie.200461440.

(39) Ooka, H.; Yamaguchi, A.; Takashima, T.; Hashimoto, K.; Nakamura, R. Efficiency of Oxygen Evolution on Iridium Oxide Determined from the PH Dependence of Charge Accumulation. *Journal of Physical Chemistry C* **2017**. https://doi.org/10.1021/acs.jpcc.7b03749.

(40) Hori, Y.; Takahashi, R.; Yoshinami, Y.; Murata, A. Electrochemical Reduction of CO at a Copper Electrode. *The Journal of Physical Chemistry B* **1997**. https://doi.org/10.1021/jp970284i.

(41) Schouten, K. J. P.; Qin, Z.; Gallent, E. P.; Koper, M. T. M. Two Pathways for the Formation of Ethylene in CO Reduction on Single-Crystal Copper Electrodes. *J Am Chem Soc* **2012**. https://doi.org/10.1021/ja302668n.

(42) Strmcnik, D.; Uchimura, M.; Wang, C.; Subbaraman, R.; Danilovic, N.; van der Vliet, D.; Paulikas, A. P.; Stamenkovic, V. R.; Markovic, N. M. Improving the Hydrogen Oxidation Reaction Rate by Promotion of Hydroxyl Adsorption. *Nature Chemistry* **2013**. https://doi.org/10.1038/nchem.1574.

(43) Roberts, F. S.; Kuhl, K. P.; Nilsson, A. Electroreduction of Carbon Monoxide over a Copper Nanocube Catalyst: Surface Structure and PH Dependence on Selectivity. *ChemCatChem* **2016**. https://doi.org/10.1002/cctc.201501189.

(44) Xiao, H.; Cheng, T.; Goddard, W. A.; Sundararaman, R. Mechanistic Explanation of the PH Dependence and Onset Potentials for Hydrocarbon Products from Electrochemical Reduction of CO on Cu (111). *J Am Chem Soc* **2016**. https://doi.org/10.1021/jacs.5b11390.

(45) Singh, M. R.; Clark, E. L.; Bell, A. T. Effects of Electrolyte, Catalyst, and Membrane Composition and Operating Conditions on the Performance of Solar-Driven Electrochemical Reduction of Carbon Dioxide. *Physical Chemistry Chemical Physics* **2015**. https://doi.org/10.1039/c5cp03283k.

(46) Weng, L.-C.; Bell, A. T.; Weber, A. Z. Towards Membrane-Electrode Assembly Systems for CO2 Reduction: A Modeling Study. *Energy & Environmental Science* **2019**, *12* (6), 1950–1968. https://doi.org/10.1039/C9EE00909D.

(47) Higgins, D.; Hahn, C.; Xiang, C.; Jaramillo, T. F.; Weber, A. Z. Gas-Diffusion Electrodes for Carbon Dioxide Reduction: A New Paradigm. *ACS Energy Letters* **2019**, *4* (1), 317–324. https://doi.org/10.1021/ACSENERGYLETT.8B02035/ASSET/IMAGES/LARGE/NZ-2018-02035T_0003.JPEG.

(48) Garg, S.; Li, M.; Weber, A. Z.; Ge, L.; Li, L.; Rudolph, V.; Wang, G.; Rufford, T. E. Advances and Challenges in Electrochemical CO2 Reduction Processes: An Engineering and Design Perspective Looking Beyond New Catalyst Materials. *Journal of Materials Chemistry A* **2020**, *8* (4), 1511–1544. https://doi.org/10.1039/C9TA13298H.

(49) NIST Chemistry Webbook. *Choice Reviews Online* **2013**. https://doi.org/10.5860/choice.35-2709.

(50) Verma, S.; Lu, X.; Ma, S.; Masel, R. I.; Kenis, P. J. A. The Effect of Electrolyte Composition on the Electroreduction of CO2 to CO on Ag Based Gas Diffusion Electrodes. *Physical Chemistry Chemical Physics* **2016**. https://doi.org/10.1039/c5cp05665a.

(51) Cook, R. L.; MacDuff, R. C.; Sammells, A. F. High Rate Gas Phase Carbon Dioxide Reduction to Ethylene and Methane Using Gas Diffusion Electrodes. *J. Electrochem. Soc.* **1990**. https://doi.org/10.1149/1.2086515.

(52) Hara, K.; Sakata, T. Large Current Density CO2 Reduction under High Pressure Using Gas Diffusion Electrodes. *Bull Chem Soc Jpn* **1997**. https://doi.org/10.1246/bcsj.70.571.

(53) Kopljar, D.; Inan, A.; Vindayer, P.; Wagner, N.; Klemm, E. Electrochemical Reduction of CO2 to Formate at High Current Density Using Gas Diffusion Electrodes. *Journal of Applied Electrochemistry* **2014**. https://doi.org/10.1007/s10800-014-0731-x.

(54) Kopljar, D.; Inan, A.; Vindayer, P.; Scholz, R.; Frangos, N.; Wagner, N.; Klemm, E. Development and Utilization of Gas Diffusion Electrodes for the Electrochemical Reduction of CO2; *Chemie-Ingenieur-Technik* **2015**. https://doi.org/10.1002/cite.201400135.

(55) Ogura, K. Electrochemical Reduction of CO[Sub 2] with a Functional Gas-Diffusion Electrode in Aqueous Solutions With and Without Propylene Carbonate. *Journal of The Electrochemical Society* **1999**. https://doi.org/10.1149/1.1392542.

(56) Weng, L. C.; Bell, A. T.; Weber, A. Z. Modeling Gas-Diffusion Electrodes for CO2 Reduction. *Physical Chemistry Chemical Physics* **2018**. https://doi.org/10.1039/c8cp01319e.

(57) Jouny, M.; Luc, W.; Jiao, F. General Techno-Economic Analysis of CO2 Electrolysis Systems. *Industrial and Engineering Chemistry Research* **2018**, *57* (6), 2165–2177. https://doi.org/10.1021/ACS.IECR.7B03514/SUPPL_FILE/IE7B03514_SI_002.XLSX.

(58) Romiluyi, O.; Danilovic, N.; Bell, A. T.; Weber, A. Z. Membrane-electrode Assembly Design Parameters for Optimal CO 2 Reduction . *Electrochemical Science Advances* **2022**. https://doi.org/10.1002/ELSA.202100186.

(59) Weng, L. C.; Bell, A. T.; Weber, A. Z. A Systematic Analysis of Cu-Based Membrane-Electrode Assemblies for CO2reduction through Multiphysics Simulation. *Energy and Environmental Science* **2020**. https://doi.org/10.1039/d0ee01604g.

(60) Fink, A. G.; Lees, E. W.; Zhang, Z.; Ren, S.; Delima, R. S.; Berlinguette, C. P. Impact of Alkali Cation Identity on the Conversion of HCO3− to CO in Bicarbonate Electrolyzers. *ChemElectroChem* **2021**, *8* (11), 2094–2100. https://doi.org/10.1002/CELC.202100408.

(61) Huang, J. E.; Li, F.; Ozden, A.; Rasouli, A. S.; de Arquer, F. P. G.; Liu, S.; Zhang, S.; Luo, M.; Wang, X.; Lum, Y.; Xu, Y.; Bertens, K.; Miao, R. K.; Dinh, C. T.; Sinton, D.; Sargent, E. H. CO2 Electrolysis to Multicarbon Products in Strong Acid. *Science (1979)* **2021**, *372* (6546), 1074–1078. https://doi.org/10.1126/SCIENCE.ABG6582/SUPPL_FILE/ABG6582_HUANG_SM.PDF.

(62) Bui, J. C.; Kim, C.; King, A. J.; Romiluyi, O.; Kusoglu, A.; Weber, A. Z.; Bell, A. T. Engineering Catalyst-Electrolyte Microenvironments to Optimize the Activity and

Selectivity for the Electrochemical Reduction of CO2on Cu and Ag. *Accounts of Chemical Research* **2022**, *55* (4), 484–494. https://doi.org/10.1021/ACS.ACCOUNTS.1C00650/ASSET/IMAGES/ACS.ACCOUNTS.1C00650.SOCIAL.JPEG_V03.

(63) Lees, E. W.; Mowbray, B. A. W.; Salvatore, D. A.; Simpson, G. L.; Dvorak, D. J.; Ren, S.; Chau, J.; Milton, K. L.; Berlinguette, C. P. Linking Gas Diffusion Electrode Composition to CO2 Reduction in a Flow Cell. *Journal of Materials Chemistry A* **2020**, *8* (37), 19493–19501. https://doi.org/10.1039/D0TA03570J.

(64) Endrődi, B.; Bencsik, G.; Darvas, F.; Jones, R.; Rajeshwar, K.; Janáky, C. Continuous-Flow Electroreduction of Carbon Dioxide. *Progress in Energy and Combustion Science* **2017**, *62*, 133–154. https://doi.org/10.1016/J.PECS.2017.05.005.

(65) Lee, J.; Lim, J.; Roh, C. W.; Whang, H. S.; Lee, H. Electrochemical CO2 Reduction Using Alkaline Membrane Electrode Assembly on Various Metal Electrodes. *Journal of CO2 Utilization* **2019**, *31*, 244–250. https://doi.org/10.1016/J.JCOU.2019.03.022.

(66) Shironita, S.; Karasuda, K.; Sato, K.; Umeda, M. Methanol Generation by CO2 Reduction at a Pt–Ru/C Electrocatalyst Using a Membrane Electrode Assembly. *Journal of Power Sources* **2013**, *240*, 404–410. https://doi.org/10.1016/J.JPOWSOUR.2013.04.034.

(67) Shironita, S.; Karasuda, K.; Sato, M.; Umeda, M. Feasibility Investigation of Methanol Generation by CO2 Reduction Using Pt/C-Based Membrane Electrode Assembly for a Reversible Fuel Cell. *Journal of Power Sources* **2013**, *228*, 68–74. https://doi.org/10.1016/J.JPOWSOUR.2012.11.097.

(68) Hua, W.; Sun, H.; Lin, L.; Mu, Q.; Yang, B.; Su, Y.; Wu, H.; Lyu, F.; Zhong, J.; Deng, Z.; Peng, Y. A Hierarchical Single-Atom Ni-N3-C Catalyst for Electrochemical CO2 Reduction to CO with Near-Unity Faradaic Efficiency in a Broad Potential Range. *Chemical Engineering Journal* **2022**, *446*, 137296. https://doi.org/10.1016/J.CEJ.2022.137296.

(69) Nguyen-Phan, T.-D.; Hu, L.; Howard, B. H.; Xu, W.; Stavitski, E.; Leshchev, D.; Rothenberger, A.; Neyerlin, K. C.; Kauffman, D. R. High Current Density Electroreduction of CO2 into Formate with Tin Oxide Nanospheres. *Scientific Reports 2022 12:1* **2022**, *12* (1), 1–10. https://doi.org/10.1038/s41598-022-11890-6.

(70) Yin, Z.; Peng, H.; Wei, X.; Zhou, H.; Gong, J.; Huai, M.; Xiao, L.; Wang, G.; Lu, J.; Zhuang, L. An Alkaline Polymer Electrolyte CO2 Electrolyzer Operated with Pure Water. *Energy & Environmental Science* **2019**, *12* (8), 2455–2462. https://doi.org/10.1039/C9EE01204D.

(71) Hoof, L.; Thissen, N.; Pellumbi, K.; junge Puring, K.; Siegmund, D.; Mechler, A. K.; Apfel, U.-P. Hidden Parameters for Electrochemical Carbon Dioxide Reduction in Zero-Gap Electrolyzers. *Cell Reports Physical Science* **2022**, *3*, 100825. https://doi.org/10.1016/j.xcrp.2022.100825.

(72) Shafaque, H. W.; Lee, C.; Fahy, K. F.; Lee, J. K.; Lamanna, J. M.; Baltic, E.; Hussey, D. S.; Jacobson, D. L.; Bazylak, A. Boosting Membrane Hydration for High Current Densities in Membrane Electrode Assembly CO 2 Electrolysis. *Cite This: ACS Appl. Mater. Interfaces* **2020**, *12*, 54595. https://doi.org/10.1021/acsami.0c14832.

(73) Mowbray, B. A. W.; Dvorak, D. J.; Taherimakhsousi, N.; Berlinguette, C. P. How Catalyst Dispersion Solvents Affect CO2Electrolyzer Gas Diffusion Electrodes. *Energy and Fuels* **2021**, *35* (23), 19178–19184. https://doi.org/10.1021/ACS.ENERGYFUELS.1C01731/SUPPL_FILE/EF1C01731_SI_001.PDF.

(74) Choi, W.; Park, S.; Jung, W.; Won, D. H.; Na, J.; Hwang, Y. J. Origin of Hydrogen Incorporated into Ethylene during Electrochemical CO2 Reduction in Membrane Electrode Assembly. *ACS Energy Letters* **2022**, *7* (3), 939–945. https://doi.org/10.1021/ACSENERGYLETT.1C02658/ASSET/IMAGES/LARGE/NZ1C02658_0004.JPEG.

(75) Gabardo, C. M.; O'Brien, C. P.; Edwards, J. P.; McCallum, C.; Xu, Y.; Dinh, C. T.; Li, J.; Sargent, E. H.; Sinton, D. Continuous Carbon Dioxide Electroreduction to Concentrated Multi-Carbon Products Using a Membrane Electrode Assembly. *Joule* **2019**, *3* (11), 2777–2791. https://doi.org/10.1016/J.JOULE.2019.07.021.

(76) Xu, Y.; Li, F.; Xu, A.; Edwards, J. P.; Hung, S. F.; Gabardo, C. M.; O'Brien, C. P.; Liu, S.; Wang, X.; Li, Y.; Wicks, J.; Miao, R. K.; Liu, Y.; Li, J.; Huang, J. E.; Abed, J.; Wang, Y.; Sargent, E. H.; Sinton, D. Low Coordination Number Copper Catalysts for Electrochemical CO2 Methanation in a Membrane Electrode Assembly. *Nature Communications 2021 12:1* **2021**, *12* (1), 1–7. https://doi.org/10.1038/s41467-021-23065-4.

(77) Dinh, C. T.; Burdyny, T.; Kibria, G.; Seifitokaldani, A.; Gabardo, C. M.; Pelayo García De Arquer, F.; Kiani, A.; Edwards, J. P.; de Luna, P.; Bushuyev, O. S.; Zou, C.; Quintero-Bermudez, R.; Pang, Y.; Sinton, D.; Sargent, E. H. CO2 Electroreduction to Ethylene via Hydroxide-Mediated Copper Catalysis at an Abrupt Interface. *Science (1979)* **2018**, *360* (6390), 783–787. https://doi.org/10.1126/SCIENCE.AAS9100/SUPPL_FILE/AAS9100-DINH-SM.PDF.

(78) Li, F.; Thevenon, A.; Rosas-Hernández, A.; Wang, Z.; Li, Y.; Gabardo, C. M.; Ozden, A.; Dinh, C. T.; Li, J.; Wang, Y.; Edwards, J. P.; Xu, Y.; McCallum, C.; Tao, L.; Liang, Z. Q.; Luo, M.; Wang, X.; Li, H.; O'Brien, C. P.; Tan, C. S.; Nam, D. H.; Quintero-Bermudez, R.; Zhuang, T. T.; Li, Y. C.; Han, Z.; Britt, R. D.; Sinton, D.; Agapie, T.; Peters, J. C.; Sargent, E. H. Molecular Tuning of CO2-to-Ethylene Conversion. *Nature 2019 577:7791* **2019**, *577* (7791), 509–513. https://doi.org/10.1038/s41586-019-1782-2.

(79) García de Arquer, F. P.; Dinh, C. T.; Ozden, A.; Wicks, J.; McCallum, C.; Kirmani, A. R.; Nam, D. H.; Gabardo, C.; Seifitokaldani, A.; Wang, X.; Li, Y. C.; Li, F.; Edwards, J.; Richter, L. J.; Thorpe, S. J.; Sinton, D.; Sargent, E. H. CO2 Electrolysis to Multicarbon Products at Activities Greater than 1 A Cm−2. *Science (1979)* **2020**, *367* (6478), 661–666. https://doi.org/10.1126/SCIENCE.AAY4217/SUPPL_FILE/AAY4217_GARCIADEARQUER_SM.PDF.

(80) Yang, K.; Li, M.; Subramanian, S.; Blommaert, M. A.; Smith, W. A.; Burdyny, T. Cation-Driven Increases of Co2utilization in a Bipolar Membrane Electrode Assembly for Co2electrolysis. *ACS Energy Letters* **2021**, *6* (12), 4291–4298. https://doi.org/10.1021/ACSENERGYLETT.1C02058/ASSET/IMAGES/LARGE/NZ1C02058_0005.JPEG.

(81) Pribyl-Kranewitter, B.; Beard, A.; Schuler, T.; Diklić, N.; Schmidt, T. J. Investigation and Optimization of Operating Conditions for Low-Temperature CO2 Reduction to CO in a Forward-Bias Bipolar-Membrane Electrolyzer. *Journal of The Electrochemical Society* **2021**, *168* (4), 043506. https://doi.org/10.1149/1945-7111/ABF063.

(82) Kim, D.; Choi, W.; Lee, H. W.; Lee, S. Y.; Choi, Y.; Lee, D. K.; Kim, W.; Na, J.; Lee, U.; Hwang, Y. J.; Won, D. H. Electrocatalytic Reduction of Low Concentrations of CO2Gas in a Membrane Electrode Assembly Electrolyzer. *ACS Energy Letters* **2021**, *6* (10), 3488–3495. https://doi.org/10.1021/ACSENERGYLETT.1C01797/ASSET/IMAGES/LARGE/NZ1C01797_0004.JPEG.

(83) Kas, R.; Yang, K.; Yewale, G. P.; Crow, A.; Burdyny, T.; Smith, W. A. Modeling the Local Environment within Porous Electrode during Electrochemical Reduction of Bicarbonate. *Industrial and Engineering Chemistry Research* **2022**. https://doi.org/10.1021/ACS.IECR.2C00352/ASSET/IMAGES/LARGE/IE2C00352_0007.JPEG.

(84) Lin, Y. R.; Lee, D. U.; Tan, S.; Koshy, D. M.; Lin, T. Y.; Wang, L.; Corral, D.; Avilés Acosta, J. E.; Zamora Zeledon, J. A.; Beck, V. A.; Baker, S. E.; Duoss, E. B.; Hahn, C.; Jaramillo, T. F. Vapor-Fed Electrolyzers for Carbon Dioxide Reduction Using Tandem Electrocatalysts: Cuprous Oxide Coupled with Nickel-Coordinated Nitrogen-Doped Carbon. *Advanced Functional Materials* **2022**, 2113252. https://doi.org/10.1002/ADFM.202113252.

(85) Zhang, T.; Bui, J. C.; Li, Z.; Bell, A. T.; Weber, A. Z.; Wu, J. Highly Selective and Productive Reduction of Carbon Dioxide to Multicarbon Products via in Situ CO Management Using Segmented Tandem Electrodes. *Nature Catalysis 2022 5:3* **2022**, *5* (3), 202–211. https://doi.org/10.1038/s41929-022-00751-0.

(86) Iqbal, M. Z.; Imteyaz, S.; Ghanty, C.; Sarkar, S. A Review on Electrochemical Conversion of CO2 to CO: Ag-Based Electrocatalyst and Cell Configuration for Industrial Application. *Journal of Industrial and Engineering Chemistry* **2022**. https://doi.org/10.1016/J.JIEC.2022.05.041.

(87) Anantharaj, S.; Noda, S. Dos and Don'ts in Screening Water Splitting Electrocatalysts. *Energy Advances* **2022**. https://doi.org/10.1039/D2YA00076H.

(88) Chatenet, M.; Pollet, B. G.; Dekel, D. R.; Dionigi, F.; Deseure, J.; Millet, P.; Braatz, R. D.; Bazant, M. Z.; Eikerling, M.; Staffell, I.; Balcombe, P.; Shao-Horn, Y.; Schäfer, H. Water Electrolysis: From Textbook Knowledge to the Latest Scientific Strategies and Industrial Developments. *Chemical Society Reviews* **2022**, *51* (11), 4583–4762. https://doi.org/10.1039/D0CS01079K.

(89) Kiessling, A.; Fornaciari, J. C.; Anderson, G.; Peng, X.; Gerstmayr, A.; Gerhardt, M. R.; McKinney, S.; Serov, A.; Kim, Y. S.; Zulevi, B.; Weber, A. Z.; Danilovic, N. Influence of Supporting Electrolyte on Hydroxide Exchange Membrane Water Electrolysis Performance: Anolyte. *Journal of The Electrochemical Society* **2021**, *168* (8), 084512. https://doi.org/10.1149/1945-7111/AC1DCD.

(90) Kiessling, A.; Fornaciari, J. C.; Anderson, G.; Peng, X.; Gerstmayr, A.; Gerhardt, M.; McKinney, S.; Serov, A.; Weber, A. Z.; Kim, Y. S.; Zulevi, B.; Danilovic, N. Influence of Supporting Electrolyte on Hydroxide Exchange Membrane Water Electrolysis Performance: Catholyte. *Journal of The Electrochemical Society* **2022**, *169* (2), 024510. https://doi.org/10.1149/1945-7111/AC4FED.

(91) Li, D.; Motz, A. R.; Bae, C.; Fujimoto, C.; Yang, G.; Zhang, F. Y.; Ayers, K. E.; Kim, Y. S. Durability of Anion Exchange Membrane Water Electrolyzers. *Energy & Environmental Science* **2021**, *14* (6), 3393–3419. https://doi.org/10.1039/D0EE04086J.

(92) Pivovar, B. 2011 Alkaline Membrane Fuel Cell Workshop Final Report (Proceedings). **2011**.

(93) Rashid, M.; al Mesfer, M. K.; Naseem, H.; Danish, M. Hydrogen Production by Water Electrolysis: A Review of Alkaline Water Electrolysis, PEM Water Electrolysis and High Temperature Water Electrolysis. *International Journal of Engineering and Advanced Technology (IJEAT)* **2015**, No. 3, 2249–8958.

(94) Wang, L.; Nitopi, S. A.; Bertheussen, E.; Orazov, M.; Morales-Guio, C. G.; Liu, X.; Higgins, D. C.; Chan, K.; Nørskov, J. K.; Hahn, C.; Jaramillo, T. F. Electrochemical Carbon Monoxide Reduction on Polycrystalline Copper: Effects of Potential, Pressure, and PH on Selectivity toward Multicarbon and Oxygenated Products. *ACS Catalysis* **2018**, *8* (8), 7445–7454. https://doi.org/10.1021/ACSCATAL.8B01200/SUPPL_FILE/CS8B01200_SI_001.PDF.

(95) Liu, X.; Schlexer, P.; Xiao, J.; Ji, Y.; Wang, L.; Sandberg, R. B.; Tang, M.; Brown, K. S.; Peng, H.; Ringe, S.; Hahn, C.; Jaramillo, T. F.; Nørskov, J. K.; Chan, K. PH Effects on the Electrochemical Reduction of CO(2) towards C2 Products on Stepped Copper. *Nature Communications 2019 10:1* **2019**, *10* (1), 1–10. https://doi.org/10.1038/s41467-018-07970-9.

(96) Resasco, J.; Chen, L. D.; Clark, E.; Tsai, C.; Hahn, C.; Jaramillo, T. F.; Chan, K.; Bell, A. T. Promoter Effects of Alkali Metal Cations on the Electrochemical Reduction of Carbon Dioxide. *J Am Chem Soc* **2017**. https://doi.org/10.1021/jacs.7b06765.

(97) Ringe, S.; Clark, E. L.; Resasco, J.; Walton, A.; Seger, B.; Bell, A. T.; Chan, K. Understanding Cation Effects in Electrochemical CO_2 Reduction. *Energy & Environmental Science* **2019**. https://doi.org/10.1039/C9EE01341E.

(98) Singh, M. R.; Kwon, Y.; Lum, Y.; Ager, J. W.; Bell, A. T. Hydrolysis of Electrolyte Cations Enhances the Electrochemical Reduction of CO2 over Ag and Cu. *J Am Chem Soc* **2016**, *138* (39), 13006–13012. https://doi.org/10.1021/JACS.6B07612/ASSET/IMAGES/JA-2016-07612A_M001.GIF.

(99) Singh, M. R.; Goodpaster, J. D.; Weber, A. Z.; Head-Gordon, M.; Bell, A. T. Mechanistic Insights into Electrochemical Reduction of CO2 over Ag Using Density Functional Theory and Transport Models. *Proc Natl Acad Sci U S A* **2017**, *114* (42), E8812–E8821. https://doi.org/10.1073/PNAS.1713164114/SUPPL_FILE/PNAS.1713164114.SAPP.PDF.

(100) Resasco, J.; Lum, Y.; Clark, E.; Zeledon, J. Z.; Bell, A. T. Effects of Anion Identity and Concentration on Electrochemical Reduction of CO2. *ChemElectroChem* **2018**. https://doi.org/10.1002/celc.201701316.

(101) Nesbitt, N. T.; Burdyny, T.; Simonson, H.; Salvatore, D.; Bohra, D.; Kas, R.; Smith, W. A. Liquid-Solid Boundaries Dominate Activity of CO2Reduction on Gas-Diffusion Electrodes. *ACS Catalysis* **2020**. https://doi.org/10.1021/acscatal.0c03319.

(102) Moore, T.; Xia, X.; Baker, S. E.; Duoss, E. B.; Beck, V. A. Elucidating Mass Transport Regimes in Gas Diffusion Electrodes for CO2Electroreduction. *ACS Energy Letters* **2021**, *6* (10), 3600–3606. https://doi.org/10.1021/ACSENERGYLETT.1C01513/ASSET/IMAGES/MEDIUM/NZ1C01513_M014.GIF.

(103) Guzmán, H.; Zammillo, F.; Roldán, D.; Galletti, C.; Russo, N.; Hernández, S. Investigation of Gas Diffusion Electrode Systems for the Electrochemical CO2 Conversion. *Catalysts 2021, Vol. 11, Page 482* **2021**, *11* (4), 482. https://doi.org/10.3390/CATAL11040482.

(104) Lum, Y.; Kwon, Y.; Lobaccaro, P.; Chen, L.; Clark, E. L.; Bell, A. T.; Ager, J. W. Trace Levels of Copper in Carbon Materials Show Significant Electrochemical CO2 Reduction Activity. *ACS Catalysis* **2016**. https://doi.org/10.1021/acscatal.5b02399.

(105) Berlinger, S. A.; Garg, S.; Weber, A. Z. Multicomponent, Multiphase Interactions in Fuel-Cell Inks. *Current Opinion in Electrochemistry* **2021**, *29*, 100744. https://doi.org/10.1016/J.COELEC.2021.100744.

(106) Khandavalli, S.; Park, J. H.; Kariuki, N. N.; Myers, D. J.; Stickel, J. J.; Hurst, K.; Neyerlin, K. C.; Ulsh, M.; Mauger, S. A. Rheological Investigation on the Microstructure of Fuel Cell Catalyst Inks. *ACS Applied Materials and Interfaces* **2018**, *10* (50), 43610–43622. https://doi.org/10.1021/ACSAMI.8B15039/SUPPL_FILE/AM8B15039_SI_001.PDF.

(107) Berlinger, S. A.; Dudenas, P. J.; Bird, A.; Chen, X.; Freychet, G.; McCloskey, B. D.; Kusoglu, A.; Weber, A. Z. Impact of Dispersion Solvent on Ionomer Thin Films and Membranes. **2022**, *18*, 4. https://doi.org/10.1021/acsapm.0c01076.

(108) Berlinger, S. A.; McCloskey, B. D.; Weber, A. Z. Inherent Acidity of Perfluorosulfonic Acid Ionomer Dispersions and Implications for Ink Aggregation. *Journal of Physical Chemistry B* **2018**, *122* (31), 7790–7796. https://doi.org/10.1021/ACS.JPCB.8B06493/ASSET/IMAGES/LARGE/JP-2018-06493S_0002.JPEG.

(109) Lee, J. H.; Doo, G.; Kwon, S. H.; Choi, S.; Kim, H. T.; Lee, S. G. Dispersion-Solvent Control of Ionomer Aggregation in a Polymer Electrolyte Membrane Fuel Cell. *Scientific Reports 2018 8:1* **2018**, *8* (1), 1–8. https://doi.org/10.1038/s41598-018-28779-y.

(110) Khandavalli, S.; Park, J. H.; Kariuki, N. N.; Zaccarine, S. F.; Pylypenko, S.; Myers, D. J.; Ulsh, M.; Mauger, S. A. Investigation of the Microstructure and Rheology of Iridium Oxide Catalyst Inks for Low-Temperature Polymer Electrolyte Membrane Water Electrolyzers. *ACS Appl. Mater. Interfaces* **2019**, *11*, 59. https://doi.org/10.1021/acsami.9b14415.

(111) Salam, M. A.; Habib, M. S.; Arefin, P.; Ahmed, K.; Uddin, M. S.; Hossain, T.; Papri, N. Effect of Temperature on the Performance Factors and Durability of Proton Exchange Membrane of Hydrogen Fuel Cell: A Narrative Review. *Material Science Research India* **2020**, *17* (2), 179–191. https://doi.org/10.13005/MSRI/170210.

(112) Kutz, R. B.; Chen, Q.; Yang, H.; Sajjad, S. D.; Liu, Z.; Masel, I. R. Sustainion Imidazolium-Functionalized Polymers for Carbon Dioxide Electrolysis. *Energy Technology* **2017**. https://doi.org/10.1002/ente.201600636.

(113) Mauritz, K. A.; Moore, R. B. State of Understanding of Nafion. *Chemical Reviews* **2004**, *104* (10), 4535–4585. https://doi.org/10.1021/CR0207123/ASSET/IMAGES/MEDIUM/CR0207123E00007.GIF.

(114) Mandal, M.; Huang, G.; Kohl, P. A. Highly Conductive Anion-Exchange Membranes Based on Cross-Linked Poly(Norbornene): Vinyl Addition Polymerization. *ACS Applied Energy Materials* **2019**, *2* (4), 2447–2457. https://doi.org/10.1021/ACSAEM.8B02051/ASSET/IMAGES/LARGE/AE-2018-02051A_0007.JPEG.

(115) Krivina, R. A.; Lindquist, G. A.; Yang, M. C.; Cook, A. K.; Hendon, C. H.; Motz, A. R.; Capuano, C.; Ayers, K. E.; Hutchison, J. E.; Boettcher, S. W. Three-Electrode Study of Electrochemical Ionomer Degradation Relevant to Anion-Exchange-Membrane Water Electrolyzers. *ACS Applied Materials and Interfaces* **2022**, *14* (16), 18261–18274. https://doi.org/10.1021/ACSAMI.1C22472/ASSET/IMAGES/LARGE/AM1C22472_0011.JPEG.

(116) Lindquist, G. A.; Oener, S. Z.; Krivina, R.; Motz, A. R.; Keane, A.; Capuano, C.; Ayers, K. E.; Boettcher, S. W. Performance and Durability of Pure-Water-Fed Anion Exchange Membrane Electrolyzers Using Baseline Materials and Operation. *ACS Applied Materials and Interfaces* **2021**, *13* (44), 51917–51924. https://doi.org/10.1021/ACSAMI.1C06053/SUPPL_FILE/AM1C06053_SI_003.PDF.

(117) Ehlinger, V. M.; Kusoglu, A.; Weber, A. Z. Modeling Coupled Durability and Performance in Polymer-Electrolyte Fuel Cells: Membrane Effects. *Journal of The Electrochemical Society* **2019**. https://doi.org/10.1149/2.0281907jes.

(118) Lu, X.; Leung, D. Y. C.; Wang, H.; Xuan, J. A High Performance Dual Electrolyte Microfluidic Reactor for the Utilization of CO2. *Applied Energy* **2017**, *194*, 549–559. https://doi.org/10.1016/J.APENERGY.2016.05.091.

(119) Sonoyama, N.; Kirii, M.; Sakata, T. Electrochemical Reduction of CO2 at Metal-Porphyrin Supported Gas Diffusion Electrodes under High Pressure CO2. *Electrochemistry Communications* **1999**, *1* (6), 213–216. https://doi.org/10.1016/S1388-2481(99)00041-7.

(120) Dufek, E. J.; Lister, T. E.; McIlwain, M. E. Bench-Scale Electrochemical System for Generation of CO and Syn-Gas. *Journal of Applied Electrochemistry 2011 41:6* **2011**, *41* (6), 623–631. https://doi.org/10.1007/S10800-011-0271-6.

(121) Park, J.; Palmre, V.; Hwang, T.; Kim, K.; Yim, W.; Bae, C. Electromechanical Performance and Other Characteristics of IPMCs Fabricated with Various Commercially Available Ion Exchange Membranes. *Smart Materials and Structures* **2014**, *23* (7), 074001. https://doi.org/10.1088/0964-1726/23/7/074001.

(122) Ethylene Electrosynthesis: A Comparative Techno-Economic Analysis of Alkaline vs Membrane Electrode Assembly vs CO 2 −CO− C 2 H 4 Tandems. **2021**. https://doi.org/10.1021/acsenergylett.0c02633.

(123) Gerhardt, M. R.; Pant, L. M.; Weber, A. Z. Along-the-Channel Impacts of Water Management and Carbon-Dioxide Contamination in Hydroxide-Exchange-Membrane Fuel Cells: A Modeling Study. *Journal of The Electrochemical Society* **2019**. https://doi.org/10.1149/2.0171907jes.

(124) Taie, Z.; Peng, X.; Kulkarni, D.; Zenyuk, I. v.; Weber, A. Z.; Hagen, C.; Danilovic, N. Pathway to Complete Energy Sector Decarbonization with Available Iridium Resources Using Ultralow Loaded Water Electrolyzers. *ACS Applied Materials and Interfaces* **2020**, *12* (47), 52701–52712. https://doi.org/10.1021/acsami.0c15687.

(125) Berlinger, S. A.; McCloskey, B. D.; Weber, A. Z. Probing Ionomer Interactions with Electrocatalyst Particles in Solution. *ACS Energy Letters* **2021**, 2275–2282. https://doi.org/10.1021/acsenergylett.1c00866.

(126) Lum, Y.; Ager, J. W. Sequential Catalysis Controls Selectivity in Electrochemical CO2 Reduction on Cu. *Energy and Environmental Science* **2018**. https://doi.org/10.1039/c8ee01501e.

(127) Gurudayal, G.; Perone, D.; Malani, S.; Lum, Y.; Haussener, S.; Ager, J. W. Sequential Cascade Electrocatalytic Conversion of Carbon Dioxide to C-C Coupled Products. *ACS Applied Energy Materials* **2019**, *2*, acsaem.9b00791. https://doi.org/10.1021/acsaem.9b00791.

(128) Chernyshova, I. v.; Somasundaran, P.; Ponnurangam, S. On the Origin of the Elusive First Intermediate of CO 2 Electroreduction . *Proceedings of the National Academy of Sciences* **2018**. https://doi.org/10.1073/pnas.1802256115.

(129) Bernt, M.; Gasteiger, H. A. Influence of Ionomer Content in IrO2/TiO2 Electrodes on PEM Water Electrolyzer Performance . *Journal of The Electrochemical Society* **2016**. https://doi.org/10.1149/2.0231611jes.

(130) Kim, K. H.; Lee, K. Y.; Kim, H. J.; Cho, E. A.; Lee, S. Y.; Lim, T. H.; Yoon, S. P.; Hwang, I. C.; Jang, J. H. The Effects of Nafion® Ionomer Content in PEMFC MEAs Prepared by a Catalyst-Coated Membrane (CCM) Spraying Method. *International Journal of Hydrogen Energy* **2010**. https://doi.org/10.1016/j.ijhydene.2009.11.058.

(131) Bui, J. C.; Digdaya, I.; Xiang, C.; Bell, A. T.; Weber, A. Z. Understanding Multi-Ion Transport Mechanisms in Bipolar Membranes. *ACS Applied Materials and Interfaces* **2020**. https://doi.org/10.1021/acsami.0c12686.

(132) *Modulation of the microstructure of the Ag/C-based alkaline cathode via the ionomer content for a bipolar membrane fuel cell | Elsevier Enhanced Reader*. https://reader.elsevier.com/reader/sd/pii/S0378775317304834?token=2122C6329F60B8F5BF731A224B9E29F52CBC2055F1FF3FF5D119FB57CCB1952603711EB01748A78C951203BB85DF259A&originRegion=us-east-1&originCreation=20210604153809 (accessed 2021-06-03).

(133) Schuler, T.; Chowdhury, A.; Freiberg, A. T.; Sneed, B.; Spingler, F. B.; Tucker, M. C.; More, K. L.; Radke, C. J.; Weber, A. Z. Fuel-Cell Catalyst-Layer Resistance via Hydrogen Limiting-Current Measurements. *Journal of The Electrochemical Society* **2019**. https://doi.org/10.1149/2.0031907jes.

(134) Lee, M. R.; Lee, H. Y.; Yim, S. D.; Kim, C. S.; Shul, Y. G.; Kucernak, A.; Shin, D. Effects of Ionomer Carbon Ratio and Ionomer Dispersity on the Performance and Durability of MEAs. *Fuel Cells* **2018**. https://doi.org/10.1002/fuce.201700178.

(135) Miller, H. A.; Bouzek, K.; Hnat, J.; Loos, S.; Bernäcker, C. I.; Weißgärber, T.; Röntzsch, L.; Meier-Haack, J. Green Hydrogen from Anion Exchange Membrane Water Electrolysis: A Review of Recent Developments in Critical Materials and Operating Conditions. *Sustainable Energy and Fuels*. 2020. https://doi.org/10.1039/c9se01240k.

(136) Vincent, I.; Lee, E. C.; Kim, H. M. Comprehensive Impedance Investigation of Low-Cost Anion Exchange Membrane Electrolysis for Large-Scale Hydrogen Production. *Scientific Reports* **2021**. https://doi.org/10.1038/s41598-020-80683-6.

(137) Seetharaman, S.; Balaji, R.; Ramya, K.; Dhathathreyan, K. S.; Velan, M. Graphene Oxide Modified Non-Noble Metal Electrode for Alkaline Anion Exchange Membrane Water Electrolyzers. *International Journal of Hydrogen Energy* **2013**. https://doi.org/10.1016/j.ijhydene.2013.09.033.

(138) Wu, X.; Scott, K. CuxCo3-XO4 ($0 \leq x < 1$) Nanoparticles for Oxygen Evolution in High Performance Alkaline Exchange Membrane Water Electrolysers. *Journal of Materials Chemistry* **2011**. https://doi.org/10.1039/c1jm11312g.

(139) Moura de Salles Pupo, M.; Kortlever, R. Electrolyte Effects on the Electrochemical Reduction of CO2. *ChemPhysChem*. 2019. https://doi.org/10.1002/cphc.201900680.

(140) König, M.; Vaes, J.; Klemm, E.; Pant, D. Solvents and Supporting Electrolytes in the Electrocatalytic Reduction of CO2. *iScience*. 2019. https://doi.org/10.1016/j.isci.2019.07.014.

(141) Liu, J.; Kang, Z.; Li, D.; Pak, M.; Alia, S. M.; Fujimoto, C.; Bender, G.; Kim, Y. S.; Weber, A. Z. Elucidating the Role of Hydroxide Electrolyte on Anion-Exchange-Membrane Water Electrolyzer Performance. *Journal of The Electrochemical Society* **2021**, *168* (5), 054522. https://doi.org/10.1149/1945-7111/ac0019.

(142) Hashiba, H.; Weng, L. C.; Chen, Y.; Sato, H. K.; Yotsuhashi, S.; Xiang, C.; Weber, A. Z. Effects of Electrolyte Buffer Capacity on Surface Reactant Species and the Reaction Rate of CO2 in Electrochemical CO2 Reduction. *Journal of Physical Chemistry C* **2018**. https://doi.org/10.1021/acs.jpcc.7b11316.

(143) Clark, E. L.; Resasco, J.; Landers, A.; Lin, J.; Chung, L. T.; Walton, A.; Hahn, C.; Jaramillo, T. F.; Bell, A. T. Standards and Protocols for Data Acquisition and Reporting for Studies of the Electrochemical Reduction of Carbon Dioxide. *ACS Catalysis* **2018**. https://doi.org/10.1021/acscatal.8b01340.

(144) Resasco, J.; Bell, A. T. Electrocatalytic CO2 Reduction to Fuels: Progress and Opportunities. *Trends in Chemistry*. 2020. https://doi.org/10.1016/j.trechm.2020.06.007.

(145) Tan, Y. C.; Lee, K. B.; Song, H.; Oh, J. Modulating Local CO2 Concentration as a General Strategy for Enhancing C−C Coupling in CO2 Electroreduction. *Joule* **2020**, *4* (5), 1104–1120. https://doi.org/10.1016/j.joule.2020.03.013.

(146) Schwertz, F. A.; Brow, J. E. Diffusivity of Water Vapor in Some Common Gases. *J. Chem. Phys* **1951**, *19*, 640. https://doi.org/10.1063/1.1748306.

(147) Weber, A. Z.; Newman, J. Transport in Polymer-Electrolyte Membranes : II. Mathematical Model. *Journal of The Electrochemical Society* **2004**, *151* (2), A311. https://doi.org/10.1149/1.1639157.

(148) Zheng, Y.; Omasta, T. J.; Peng, X.; Wang, L.; Varcoe, J. R.; Pivovar, B. S.; Mustain, W. E. Quantifying and Elucidating the Effect of CO2 on the Thermodynamics, Kinetics and Charge Transport of AEMFCs. *Energy and Environmental Science* **2019**. https://doi.org/10.1039/c9ee01334b.

(149) Li, M.; Idros, M. N.; Wu, Y.; Burdyny, T.; Garg, S.; Zhao, X. S.; Wang, G.; Rufford, T. E. The Role of Electrode Wettability in Electrochemical Reduction of Carbon Dioxide. *Journal of Materials Chemistry A* **2021**, *9* (35), 19369–19409. https://doi.org/10.1039/D1TA03636J.

(150) Gawel, A.; Jaster, T.; Siegmund, D.; Holzmann, J.; Lohmann, H.; Klemm, E.; Apfel, U. P. Electrochemical CO2 Reduction - The Macroscopic World of Electrode Design, Reactor Concepts & Economic Aspects. *iScience* **2022**, *25* (4), 104011. https://doi.org/10.1016/J.ISCI.2022.104011.

(151) Kim, C.; Bui, J. C.; Luo, X.; Cooper, J. K.; Kusoglu, A.; Weber, A. Z.; Bell, A. T. Tailored Catalyst Microenvironments for CO2 Electroreduction to Multicarbon Products on Copper Using Bilayer Ionomer Coatings. *Nature Energy 2021 6:11* **2021**, *6* (11), 1026–1034. https://doi.org/10.1038/s41560-021-00920-8.

(152) Koshy, D. M.; Akhade, S. A.; Shugar, A.; Abiose, K.; Shi, J.; Liang, S.; Oakdale, J. S.; Weitzner, S. E.; Varley, J. B.; Duoss, E. B.; Baker, S. E.; Hahn, C.; Bao, Z.; Jaramillo, T. F. Chemical Modifications of Ag Catalyst Surfaces with Imidazolium Ionomers Modulate H2Evolution Rates during Electrochemical CO2Reduction. *J Am Chem Soc* **2021**, *143* (36), 14712–14725. https://doi.org/10.1021/JACS.1C06212/SUPPL_FILE/JA1C06212_SI_002.ZIP.

(153) Xu, Y.; Edwards, J. P.; Zhong, J.; O'Brien, C. P.; Gabardo, C. M.; McCallum, C.; Li, J.; Dinh, C. T.; Sargent, E. H.; Sinton, D. Oxygen-Tolerant Electroproduction of C2 Products from Simulated Flue Gas. *Energy & Environmental Science* **2020**, *13* (2), 554–561. https://doi.org/10.1039/C9EE03077H.

(154) Pătru, A.; Binninger, T.; Pribyl, B.; Schmidt, T. J. Design Principles of Bipolar Electrochemical Co-Electrolysis Cells for Efficient Reduction of Carbon Dioxide from Gas Phase at Low Temperature. *Journal of The Electrochemical Society* **2019**, *166* (2), F34–F43. https://doi.org/10.1149/2.1221816JES/XML.

(155) Langford, J. I.; Wilson, A. J. C.; IUCr. Scherrer after Sixty Years: A Survey and Some New Results in the Determination of Crystallite Size. *urn:issn:0021-8898* **1978**, *11* (2), 102–113. https://doi.org/10.1107/S0021889878012844.

(156) Lees, E. W.; Bui, J. C.; Song, D.; Weber, A. Z.; Berlinguette, C. P. Continuum Model to Define the Chemistry and Mass Transfer in a Bicarbonate Electrolyzer. *ACS Energy Letters* **2022**, *7* (2), 834–842. https://doi.org/10.1021/ACSENERGYLETT.1C02522/SUPPL_FILE/NZ1C02522_SI_001.PDF.

(157) Berlinger, S. A.; McCloskey, B. D.; Weber, A. Z. Understanding Binary Interactions in Fuel-Cell Catalyst-Layer Inks. *ECS Transactions* **2017**. https://doi.org/10.1149/08008.0309ecst.

(158) Chowdhury, A.; Bird, A.; Liu, J.; Zenyuk, I. v.; Kusoglu, A.; Radke, C. J.; Weber, A. Z. Linking Perfluorosulfonic Acid Ionomer Chemistry and High-Current Density Performance in Fuel-Cell Electrodes. *ACS Applied Materials and Interfaces* **2021**, *13* (36), 42579–42589. https://doi.org/10.1021/ACSAMI.1C07611/SUPPL_FILE/AM1C07611_SI_001.PDF.

(159) Bergeret, G.; Gallezot, P. Particle Size and Dispersion Measurements. *Handbook of Heterogeneous Catalysis* **2008**, 738–765. https://doi.org/10.1002/9783527610044.HETCAT0038.

(160) Feng, S.; Kondo, S.; Kaseyama, T.; Nakazawa, T.; Kikuchi, T.; Selyanchyn, R.; Fujikawa, S.; Christiani, L.; Sasaki, K.; Nishihara, M. Characterization of Polymer-Polymer Type Charge-Transfer (CT) Blend Membranes for Fuel Cell Application. *Data in Brief* **2018**, *18*, 22–29. https://doi.org/10.1016/J.DIB.2018.02.031.

(161) Liu, Z.; Yang, H.; Kutz, R.; Masel, R. I. CO 2 Electrolysis to CO and O 2 at High Selectivity, Stability and Efficiency Using Sustainion Membranes . *Journal of The Electrochemical Society* **2018**, *165* (15), J3371–J3377. https://doi.org/10.1149/2.0501815JES/XML.

(162) Sadeghpour, M.; Yusoff, R.; Aroua, M. K. Polymeric Ionic Liquids (PILs) for CO2 Capture. *Reviews in Chemical Engineering* **2017**, *33* (2), 183–200. https://doi.org/10.1515/REVCE-2015-0070/MACHINEREADABLECITATION/RIS.

(163) Ren, X.; Myles, T. D.; Grew, K. N.; Chiu, W. K. S. Carbon Dioxide Transport in Nafion 1100 EW Membrane and in a Direct Methanol Fuel Cell. *Journal of The Electrochemical Society* **2015**, *162* (10), F1221–F1230. https://doi.org/10.1149/2.0711510JES/XML.

(164) Hatsukade, T.; Kuhl, K. P.; Cave, E. R.; Abram, D. N.; Jaramillo, T. F. Insights into the Electrocatalytic Reduction of CO2 on Metallic Silver Surfaces. *Physical Chemistry Chemical Physics* **2014**. https://doi.org/10.1039/c4cp00692e.

(165) Gerhardt, M. R.; Pant, L. M.; Bui, J. C.; Crothers, A. R.; Ehlinger, V. M.; Fornaciari, J. C.; Liu, J.; Weber, A. Z. Method—Practices and Pitfalls in Voltage Breakdown Analysis of Electrochemical Energy-Conversion Systems. *Journal of The Electrochemical Society* **2021**, *168* (7), 074503. https://doi.org/10.1149/1945-7111/ABF061.

(166) Liao, H.; Watson, W.; Dizon, A.; Tribollet, B.; Vivier, V.; Orazem, M. E. Physical Properties Obtained from Measurement Model Analysis of Impedance Measurements. *Electrochimica Acta* **2020**, *354*, 136747. https://doi.org/10.1016/J.ELECTACTA.2020.136747.

(167) Watson, W.; Orazem, M. E. Python-Based Program for Error Structure Analysis and Regression of Impedance Data. *ECS Meeting Abstracts* **2020**, *MA2020-02* (20), 1577. https://doi.org/10.1149/MA2020-02201577MTGABS.

(168) Kusoglu, A.; Kwong, A.; Clark, K. T.; Gunterman, H. P.; Weber, A. Z. Water Uptake of Fuel-Cell Catalyst Layers. *Journal of The Electrochemical Society* **2012**, *159* (9), F530–F535. https://doi.org/10.1149/2.031209JES/XML.

(169) Hwang, G. S.; Parkinson, D. Y.; Kusoglu, A.; MacDowell, A. A.; Weber, A. Z. Understanding Water Uptake and Transport in Nafion Using X-Ray Microtomography. *ACS Macro Letters* **2013**, *2* (4), 288–291. https://doi.org/10.1021/MZ300651A/SUPPL_FILE/MZ300651A_SI_001.PDF.

(170) Buckley, A. K.; Lee, M.; Cheng, T.; Kazantsev, R. v.; Larson, D. M.; Goddard, W. A.; Toste, F. D.; Toma, F. M. Electrocatalysis at Organic-Metal Interfaces: Identification of Structure-Reactivity Relationships for Co2 Reduction at Modified Cu Surfaces. *J Am Chem Soc* **2019**, *141* (18), 7355–7364. https://doi.org/10.1021/JACS.8B13655/SUPPL_FILE/JA8B13655_SI_002.PDF.

(171) Jiang, K.; Huang, Y.; Zeng, G.; Toma, F. M.; Goddard, W. A.; Bell, A. T. Effects of Surface Roughness on the Electrochemical Reduction of CO2 over Cu. *ACS Energy Letters* **2020**, *5* (4), 1206–1214. https://doi.org/10.1021/ACSENERGYLETT.0C00482/SUPPL_FILE/NZ0C00482_SI_002.MP4.

(172) Lee, S. H.; Sullivan, I.; Larson, D. M.; Liu, G.; Toma, F. M.; Xiang, C.; Drisdell, W. S. Correlating Oxidation State and Surface Area to Activity from Operando Studies of Copper CO Electroreduction Catalysts in a Gas-Fed Device. *ACS Catalysis* **2020**, *10* (14), 8000–8011. https://doi.org/10.1021/ACSCATAL.0C01670/SUPPL_FILE/CS0C01670_SI_001.PDF.

(173) INABA, M.; MATSUI, Y.; SAITO, M.; TASAKA, A.; FUKUTA, K.; WATANABE, S.; YANAGI, H. Effects of Carbon Dioxide on the Performance of Anion-Exchange Membrane Fuel Cells. *Electrochemistry* **2012**. https://doi.org/10.5796/electrochemistry.79.322.

(174) Williams, K.; Corbin, N.; Zeng, J.; Lazouski, N.; Yang, D. T.; Manthiram, K. Protecting Effect of Mass Transport during Electrochemical Reduction of Oxygenated Carbon Dioxide Feedstocks. *Sustainable Energy & Fuels* **2019**, *3* (5), 1225–1232. https://doi.org/10.1039/C9SE00024K.

(175) Lees, E. W.; Liu, A.; Bui, J. C.; Ren, S.; Weber, A. Z.; Berlinguette, C. P. Electrolytic Methane Production from Reactive Carbon Solutions. *ACS Energy Letters* **2022**, 1712–1718. https://doi.org/10.1021/ACSENERGYLETT.2C00283/SUPPL_FILE/NZ2C00283_SI_001.PDF.

(176) Kummu, M.; Guillaume, J. H. A.; de Moel, H.; Eisner, S.; Flörke, M.; Porkka, M.; Siebert, S.; Veldkamp, T. I. E.; Ward, P. J. The World's Road to Water Scarcity: Shortage and Stress in the 20th Century and Pathways towards Sustainability. *Scientific Reports 2016 6:1* **2016**, *6* (1), 1–16. https://doi.org/10.1038/srep38495.

(177) Sun, F.; Qin, J.; Wang, Z.; Yu, M.; Wu, X.; Sun, X.; Qiu, J. Energy-Saving Hydrogen Production by Chlorine-Free Hybrid Seawater Splitting Coupling Hydrazine Degradation. *Nature Communications 2021 12:1* **2021**, *12* (1), 1–11. https://doi.org/10.1038/s41467-021-24529-3.

(178) Sauermoser, M.; Kizilova, N.; Pollet, B. G.; Kjelstrup, S. Flow Field Patterns for Proton Exchange Membrane Fuel Cells. *Frontiers in Energy Research* **2020**, *8*, 13. https://doi.org/10.3389/FENRG.2020.00013/BIBTEX.

(179) McBreen, J. Voltammetric Studies of Electrodes in Contact with Ionomeric Membranes.

(180) Kim, C.; Cho, K. M.; Park, K.; Kim, J. Y.; Yun, G. T.; Toma, F. M.; Gereige, I.; Jung, H. T. Cu/Cu2O Interconnected Porous Aerogel Catalyst for Highly Productive Electrosynthesis of Ethanol from CO2. *Advanced Functional Materials* **2021**, *31* (32), 2102142. https://doi.org/10.1002/ADFM.202102142.

(181) Hatzell, K. B.; Dixit, M. B.; Berlinger, S. A.; Weber, A. Z. Understanding Inks for Porous-Electrode Formation. *Journal of Materials Chemistry A* **2017**, *5* (39), 20527–20533. https://doi.org/10.1039/C7TA07255D.

(182) Conde, J. J.; Folgado, M. A.; Ferreira-Aparicio, P.; Chaparro, A. M.; Chowdhury, A.; Kusoglu, A.; Cullen, D.; Weber, A. Z. Mass-Transport Properties of Electrosprayed Pt/C Catalyst Layers for Polymer-Electrolyte Fuel Cells. *Journal of Power Sources* **2019**, *427*, 250–259. https://doi.org/10.1016/J.JPOWSOUR.2019.04.079.

(183) Katzenberg, A.; Chowdhury, A.; Fang, M.; Weber, A. Z.; Okamoto, Y.; Kusoglu, A.; Modestino, M. A. Highly Permeable Perfluorinated Sulfonic Acid Ionomers for Improved Electrochemical Devices: Insights into Structure-Property Relationships. *J Am Chem Soc* **2020**, *142* (8), 3742–3752. https://doi.org/10.1021/JACS.9B09170/SUPPL_FILE/JA9B09170_SI_001.PDF.

(184) Trotochaud, L.; Young, S. L.; Ranney, J. K.; Boettcher, S. W. Nickel-Iron Oxyhydroxide Oxygen-Evolution Electrocatalysts: The Role of Intentional and Incidental Iron Incorporation. *J Am Chem Soc* **2014**, *136* (18), 6744–6753. https://doi.org/10.1021/JA502379C/SUPPL_FILE/JA502379C_SI_001.PDF.

(185) Ali Akbari, M. S.; Bagheri, R.; Song, Z.; Najafpour, M. M. Oxygen-Evolution Reaction by Nickel/Nickel Oxide Interface in the Presence of Ferrate(VI). *Scientific Reports 2020 10:1* **2020**, *10* (1), 1–11. https://doi.org/10.1038/s41598-020-65674-x.

(186) Barecka, M. H.; Ager, J. W.; Lapkin, A. A. Techno-Economic Assessment of Emerging CO2 Electrolysis Technologies. *STAR Protocols* **2021**, *2* (4), 100889. https://doi.org/10.1016/J.XPRO.2021.100889.

(187) Na, J.; Seo, B.; Kim, J.; Lee, C. W.; Lee, H.; Hwang, Y. J.; Min, B. K.; Lee, D. K.; Oh, H. S.; Lee, U. General Technoeconomic Analysis for Electrochemical Coproduction Coupling Carbon Dioxide Reduction with Organic Oxidation. *Nature Communications 2019 10:1* **2019**, *10* (1), 1–13. https://doi.org/10.1038/s41467-019-12744-y.

(188) Spurgeon, J. M.; Kumar, B. A Comparative Technoeconomic Analysis of Pathways for Commercial Electrochemical CO2 Reduction to Liquid Products. *Energy & Environmental Science* **2018**, *11* (6), 1536–1551. https://doi.org/10.1039/C8EE00097B.

(189) Li, T.; Harrington, D. A. An Overview of Glycerol Electrooxidation Mechanisms on Pt, Pd and Au. *ChemSusChem* **2021**, *14* (6), 1472–1495. https://doi.org/10.1002/CSSC.202002669.

(190) Zhong, S. H.; Pei, Y.; Pi, Z.; Zhong, H.; Cheng, J.; Jin, F. Rsc.Li/Materials-a As Featured in: Glycerol Oxidation-Assisted Electrochemical CO2 Reduction for the Dual Production of Formate Glycerol Oxidation-Assisted Electrochemical CO 2 Reduction for the Dual Production of Formate †. **2022**, 207890. https://doi.org/10.1039/d1ta07119j.

(191) Huang, X.; Zou, Y.; Jiang, J. Electrochemical Oxidation of Glycerol to Dihydroxyacetone in Borate Buffer: Enhancing Activity and Selectivity by Borate-Polyol Coordination Chemistry. *ACS Sustainable Chemistry and Engineering* **2021**, *9* (43), 14470–14479. https://doi.org/10.1021/ACSSUSCHEMENG.1C04795/SUPPL_FILE/SC1C04795_SI_001.PDF.

(192) Fornaciari, J. C.; Primc, D.; Kawashima, K.; Wygant, B. R.; Verma, S.; Spanu, L.; Mullins, C. B.; Bell, A. T.; Weber, A. Z. A Perspective on the Electrochemical Oxidation of Methane to Methanol in Membrane Electrode Assemblies. *ACS Energy Letters* **2020**, *5* (9), 2954–2963. https://doi.org/10.1021/ACSENERGYLETT.0C01508/ASSET/IMAGES/MEDIUM/NZ0C01508_0005.GIF.

(193) Lazouski, N.; Steinberg, K. J.; Gala, M. L.; Krishnamurthy, D.; Viswanathan, V.; Manthiram, K. Proton Donors Induce a Differential Transport Effect for Selectivity toward Ammonia in Lithium-Mediated Nitrogen Reduction. *ACS Catalysis* **2022**, *12* (9), 5197–5208. https://doi.org/10.1021/ACSCATAL.2C00389/SUPPL_FILE/CS2C00389_SI_001.PDF.

(194) Lazouski, N.; Chung, M.; Williams, K.; Gala, M. L.; Manthiram, K. Non-Aqueous Gas Diffusion Electrodes for Rapid Ammonia Synthesis from Nitrogen and Water-Splitting-Derived Hydrogen. *Nature Catalysis 2020 3:5* **2020**, *3* (5), 463–469. https://doi.org/10.1038/s41929-020-0455-8.

(195) Andersen, S. Z.; Čolić, V.; Yang, S.; Schwalbe, J. A.; Nielander, A. C.; McEnaney, J. M.; Enemark-Rasmussen, K.; Baker, J. G.; Singh, A. R.; Rohr, B. A.; Statt, M. J.; Blair, S. J.; Mezzavilla, S.; Kibsgaard, J.; Vesborg, P. C. K.; Cargnello, M.; Bent, S. F.; Jaramillo, T. F.; Stephens, I. E. L.; Nørskov, J. K.; Chorkendorff, I. A Rigorous Electrochemical Ammonia Synthesis Protocol with Quantitative Isotope Measurements. *Nature 2019 570:7762* **2019**, *570* (7762), 504–508. https://doi.org/10.1038/s41586-019-1260-x.

(196) Shen, H.; Choi, C.; Masa, J.; Li, X.; Qiu, J.; Jung, Y.; Sun, Z. Electrochemical Ammonia Synthesis: Mechanistic Understanding and Catalyst Design. *Chem* **2021**, *7* (7), 1708–1754. https://doi.org/10.1016/J.CHEMPR.2021.01.009.

(197) Wu, T.; Fan, W.; Zhang, Y.; Zhang, F. Electrochemical Synthesis of Ammonia: Progress and Challenges. *Materials Today Physics* **2021**, *16*, 100310. https://doi.org/10.1016/J.MTPHYS.2020.100310.

(198) Kistler, T. A.; Um, M. Y.; Cooper, J. K.; Sharp, I. D.; Agbo, P. Exploiting Heat Transfer to Achieve Efficient Photoelectrochemical CO2 Reduction under Light Concentration. *Energy & Environmental Science* **2022**, *15* (5), 2061–2070. https://doi.org/10.1039/D1EE03957A.

(199) Kistler, T. A.; Um, M. Y.; Cooper, J. K.; Sharp, I. D.; Agbo, P. Monolithic Photoelectrochemical CO2 Reduction Producing Syngas at 10% Efficiency. *Advanced Energy Materials* **2021**, *11* (21), 2100070. https://doi.org/10.1002/AENM.202100070.

(200) Kistler, T. A.; Danilovic, N.; Agbo, P. Editors' Choice—A Monolithic Photoelectrochemical Device Evolving Hydrogen in Pure Water. *Journal of The Electrochemical Society* **2019**, *166* (13), H656. https://doi.org/10.1149/2.1151913JES.

(201) Agbo, P. Transparent Dual-Conductivity Membrane Composites as Current Distributors for Diffuse Electrocatalysts. *ACS Applied Energy Materials* **2020**, *3* (12), 12284–12290. https://doi.org/10.1021/ACSAEM.0C02339/SUPPL_FILE/AE0C02339_SI_001.PDF.

(202) Kistler, T. A.; Agbo, P. Current Loss Analysis in Photoelectrochemical Devices. *APL Materials* **2020**, *8* (3), 031107. https://doi.org/10.1063/1.5142561.

(203) Kistler, T. A.; Um, M. Y.; Agbo, P. Stable Photoelectrochemical Hydrogen Evolution for 1000 h at 14% Efficiency in a Monolithic Vapor-Fed Device. *Journal of The Electrochemical Society* **2020**, *167* (6), 066502. https://doi.org/10.1149/1945-7111/AB7D93.

(204) Agbo, P. J- v Decoupling: Independent Control over Current and Potential in Electrocatalysis. *Journal of Physical Chemistry C* **2020**, *124* (52), 28387–28394. https://doi.org/10.1021/ACS.JPCC.0C08142/SUPPL_FILE/JP0C08142_SI_001.PDF.

(205) Liu, G.; Zheng, F.; Li, J.; Zeng, G.; Ye, Y.; Larson, D. M.; Yano, J.; Crumlin, E. J.; Ager, J. W.; Wang, L. Wang; Toma, F. M. Investigation and Mitigation of Degradation Mechanisms in Cu2O Photoelectrodes for CO2 Reduction to Ethylene. *Nature Energy 2021 6:12* **2021**, *6* (12), 1124–1132. https://doi.org/10.1038/s41560-021-00927-1.

(206) Gurudayal; Beeman, J. W.; Bullock, J.; Wang, H.; Eichhorn, J.; Towle, C.; Javey, A.; Toma, F. M.; Mathews, N.; Ager, J. W. Si Photocathode with Ag-Supported Dendritic Cu Catalyst for CO2 Reduction. *Energy & Environmental Science* **2019**, *12* (3), 1068–1077. https://doi.org/10.1039/C8EE03547D.

(207) Bui, J. C.; Corpus, K. R. M.; Bell, A. T.; Weber, A. Z. On the Nature of Field-Enhanced Water Dissociation in Bipolar Membranes. *Journal of Physical Chemistry C* **2021**, *125* (45), 24974–24987. https://doi.org/10.1021/ACS.JPCC.1C08276/SUPPL_FILE/JP1C08276_SI_001.PDF.

(208) Ripatti, D. S.; Veltman, T. R.; Kanan, M. W. Carbon Monoxide Gas Diffusion Electrolysis That Produces Concentrated C2 Products with High Single-Pass Conversion. *Joule* **2019**, *3* (1), 240–256. https://doi.org/10.1016/J.JOULE.2018.10.007/ATTACHMENT/6949FD43-6E31-4ABB-8C7F-47FBC800FC31/MMC1.PDF.

(209) Jouny, M.; Hutchings, G. S.; Jiao, F. Carbon Monoxide Electroreduction as an Emerging Platform for Carbon Utilization. *Nature Catalysis 2019 2:12* **2019**, *2* (12), 1062–1070. https://doi.org/10.1038/s41929-019-0388-2.

(210) Romero Cuellar, N. S.; Scherer, C.; Kaçkar, B.; Eisenreich, W.; Huber, C.; Wiesner-Fleischer, K.; Fleischer, M.; Hinrichsen, O. Two-Step Electrochemical Reduction of CO2 towards Multi-Carbon Products at High Current Densities. *Journal of CO2 Utilization* **2020**, *36*, 263–275. https://doi.org/10.1016/J.JCOU.2019.10.016.

(211) Theaker, N.; Strain, J. M.; Kumar, B.; Brian, J. P.; Kumari, S.; Spurgeon, J. M. Heterogeneously Catalyzed Two-Step Cascade Electrochemical Reduction of CO2 to Ethanol. *Electrochimica Acta* **2018**, *274*, 1–8. https://doi.org/10.1016/J.ELECTACTA.2018.04.072.

(212) Limaye, A. M.; Zeng, J. S.; Willard, A. P.; Manthiram, K. Bayesian Data Analysis Reveals No Preference for Cardinal Tafel Slopes in CO2 Reduction Electrocatalysis. *Nature*

Communications 2021 12:1 **2021**, *12* (1), 1–10. https://doi.org/10.1038/s41467-021-20924-y.

(213) Iwama, R.; Takizawa, K.; Shinmei, K.; Baba, E.; Yagihashi, N.; Kaneko, H. Design and Analysis of Metal Oxides for CO2Reduction Using Machine Learning, Transfer Learning, and Bayesian Optimization. *ACS Omega* **2022**, *7* (12), 10709–10717. https://doi.org/10.1021/ACSOMEGA.2C00461/ASSET/IMAGES/LARGE/AO2C00461_0009.JPEG.

(214) Frey, D.; Neyerlin, K. C.; Modestino, M. A. Bayesian Optimization of Electrochemical Devices for Electrons-to-Molecules Conversions: The Case of Pulsed CO 2 Electroreduction.

(215) Mistry, A.; Franco, A. A.; Cooper, S. J.; Roberts, S. A.; Viswanathan, V. How Machine Learning Will Revolutionize Electrochemical Sciences. *ACS Energy Letters* **2021**, *6* (4), 1422–1431. https://doi.org/10.1021/ACSENERGYLETT.1C00194/ASSET/IMAGES/LARGE/NZ1C00194_0005.JPEG.

(216) Chen, A.; Zhang, X.; Chen, L.; Yao, S.; Zhou, Z. A Machine Learning Model on Simple Features for CO2Reduction Electrocatalysts. *Journal of Physical Chemistry C* **2020**, *124* (41), 22471–22478. https://doi.org/10.1021/ACS.JPCC.0C05964/SUPPL_FILE/JP0C05964_SI_001.PDF.

(217) Pestourie, R.; Mroueh, Y.; Rackauckas, C.; Das, P.; Johnson, S. G. Physics-Enhanced Deep Surrogates for PDEs. **2021**. https://doi.org/10.48550/arxiv.2111.05841.

(218) Singh, A. K.; Montoya, J. H.; Gregoire, J. M.; Persson, K. A. Robust and Synthesizable Photocatalysts for CO2 Reduction: A Data-Driven Materials Discovery. *Nature Communications 2019 10:1* **2019**, *10* (1), 1–9. https://doi.org/10.1038/s41467-019-08356-1.

(219) Guo, Y.; He, X.; Su, Y.; Dai, Y.; Xie, M.; Yang, S.; Chen, J.; Wang, K.; Zhou, D.; Wang, C. Machine-Learning-Guided Discovery and Optimization of Additives in Preparing Cu Catalysts for CO2Reduction. *J Am Chem Soc* **2021**, *143* (15), 5755–5762. https://doi.org/10.1021/JACS.1C00339/SUPPL_FILE/JA1C00339_SI_001.PDF.

(220) Malek, A.; Wang, Q.; Baumann, S.; Guillon, O.; Eikerling, M.; Malek, K. A Data-Driven Framework for the Accelerated Discovery of CO2 Reduction Electrocatalysts. *Frontiers in Energy Research* **2021**, *9*, 52. https://doi.org/10.3389/FENRG.2021.609070/BIBTEX.

(221) Agbo, P.; Danilovic, N. An Algorithm for the Extraction of Tafel Slopes. *Journal of Physical Chemistry C* **2019**, *123* (50), 30252–30264. https://doi.org/10.1021/ACS.JPCC.9B06820/SUPPL_FILE/JP9B06820_SI_002.ZIP.